


5-2013

The Geometry and Sensitivity of Ion-Beam Sculpted Nanopores for Single Molecule DNA Analysis

Ryan Connor Rollings
University of Arkansas, Fayetteville

Follow this and additional works at: <http://scholarworks.uark.edu/etd>

 Part of the [Biomedical Commons](#), [Biophysics Commons](#), [Biotechnology Commons](#), [Nanoscience and Nanotechnology Commons](#), and the [Optics Commons](#)

Recommended Citation

Rollings, Ryan Connor, "The Geometry and Sensitivity of Ion-Beam Sculpted Nanopores for Single Molecule DNA Analysis" (2013). *Theses and Dissertations*. 727.
<http://scholarworks.uark.edu/etd/727>

This Dissertation is brought to you for free and open access by ScholarWorks@UARK. It has been accepted for inclusion in Theses and Dissertations by an authorized administrator of ScholarWorks@UARK. For more information, please contact scholar@uark.edu, ccmiddle@uark.edu.

The Geometry and Sensitivity of Ion-Beam Sculpted Nanopores
for Single Molecule DNA Analysis

The Geometry and Sensitivity of Ion-Beam Sculpted Nanopores
for Single Molecule DNA Analysis

A dissertation submitted in partial fulfillment
of the requirements for the degree of
Doctor of Philosophy in Physics

By

Ryan Connor Rollings
Hendrix College
Bachelor of Arts in Physics, 2004
Hendrix College
Bachelor of Arts in Mathematics, 2004
University of Arkansas
Master of Science in Physics, 2007

May 2013
University of Arkansas

Abstract

In this dissertation, the relationship between the geometry of ion-beam sculpted solid-state nanopores and their ability to analyze single DNA molecules using resistive pulse sensing is investigated. To accomplish this, the three dimensional shape of the nanopore is determined using energy filtered and tomographic transmission electron microscopy. It is shown that this information enables the prediction of the ionic current passing through a voltage biased nanopore and improves the prediction of the magnitude of current drop signals when the nanopore interacts with single DNA molecules. The dimensional stability of nanopores in solution is monitored using this information and is improved by modifying the pore's fabrication procedure. Furthermore, the correlation between noise sources present in the nanopore and the noble gas used to form the ion beam during fabrication is investigated. Finally, the polymerase chain reaction is used to verify that DNA translocates through ion-beam sculpted nanopores.

This dissertation is approved for
recommendation to the Graduate Council

Dissertation Director:

Dr. Jiali Li, Ph.D.

Dissertation Committee:

Dr. Michael Lieber, Ph.D.

Dr. David McNabb, Ph.D.

Dr. William 'Lin' Oliver, Ph.D.

Dr. Gregory Salamo, Ph.D.

Dr. Chao-Hung 'Steve' Tung, Ph.D.

©2013 by Ryan Connor Rollings
All Rights Reserved

Dissertation Duplication Release

I hereby authorize the University of Arkansas Libraries to duplicate this dissertation when needed for research and/or scholarship.

Agreed

Ryan Connor Rollings

Refused

Ryan Connor Rollings

Acknowledgements

First, thanks to Frank Bobek, my high school physics and chemistry teacher at Field Kindley Memorial High School for introducing me to science. Thanks to Professor Richard Rolleigh and Professor Ann Wright of Hendrix College for my introduction to theoretical and experimental physics, respectively. Thanks to Ken Vickers for his part in bringing me to the University of Arkansas and for providing welcome counsel throughout my tenure here. Thanks to Dr. Bradley Ledden to whom I owe almost the entirety of my introduction to practical experimentation as well as for being a friend when times were rough. Also important in my experimentalist upbringing were Dr. Daniel Fologea, Dr. James Uplinger, Dr. Eric Krueger, and Brian Thomas. Thanks to John Wong for teaching me nearly everything I know about programming. Thanks to Dr. David McNabb for opening his lab and personally teaching a naive physicist the wild world of molecular biology. Thanks to Dr. Mourad Benamara for his training and help with the beautiful microscopes that have transformed the way I see the world. Special thanks go to my adviser, Professor Jiali Li, for accepting me into her lab and offering me amazing opportunities at her earliest opportunity, guiding me to become an independent scientist, and bringing together the cast of characters that have influenced me so.

Thanks to my lab-mates and friends Santoshi 'Tosh-sister' Nandivada, Harpreet 'Preet' Kaur, Dr. Changbae Hyun, Nathan Walsh, and Ed 'Be-Aggressive' Graef. May you be lucky enough to find as much support both inside and outside the lab as I received from you.

I could never thank my parents enough for the care and encouragement I have received, but I'd like to at least thank them here for encouraging the little boy who endlessly studied tiny pebbles and smashed his toys to see what made them work. Finally, thanks to my wife, Erin, who has supported me and endured more throughout the duration of this work more than anyone knows; I hope to one day repay her.

Dedication

I dedicate this dissertation in memory of my sister.

May this work symbolize the knowledge she would have spread.

In memory of
Rachel Erin Rollings
1984-2006

Contents

1	Introduction	1
1.1	Nanopore detection principle	1
1.2	Important nanopore parameters	5
1.3	Recent developments in nanopore sequencing	7
1.3.1	Improving biological nanopores	7
1.3.2	Improving solid state nanopores	8
1.3.3	Commercialization of nanopore sequencing	9
1.4	Challenges addressed by this dissertation	10
1.5	Organization of this dissertation	11
1.6	A note on source material	12
2	Experimental setup and methods	13
2.1	Nanopore fabrication	13
2.1.1	Fabricating the freestanding membrane	13
2.1.2	Ion-beam sculpting (IBS)	13
2.1.3	TEM drilling	17
2.2	Fluidic system	17
2.3	Current measurement	18
2.3.1	Electrochemistry	18
2.3.2	Electronics	19
2.4	DNA translocation	21
2.5	Data analysis	24
2.6	Translocation protocols	25
2.6.1	Storage of pore before experiment	27
2.6.2	PDMS chamber fabrication	28
2.6.3	Electrode fabrication	29
2.6.4	Solution preparation	30
2.6.5	Wetting the nanopore and establishing a current	31
2.6.6	Adding DNA	33
2.7	Biochemical protocols	34
2.7.1	Purchasing DNA	35
2.7.2	Purifying DNA	35
2.7.3	ssDNA-dsDNA hybrid molecules	36
3	Nanopore conductance, conductance drop, and stability in salt solutions	39
3.1	Introduction	39
3.2	Methods	40
3.2.1	Nanopore fabrication	40
3.2.2	TEM geometry characterization	41
3.2.3	Conductance and conductance drop measurement	42
3.3	Results and Discussion	43
3.3.1	Conductance increased with simultaneous decrease in conductance drop	43

3.3.2	Nanopores etch laterally during experiment	45
3.3.3	Modeling to determine radius change from conductance and conductance drop	47
3.3.4	Radius change rate determined from conductance and conductance drop is similar	50
3.3.5	Radius change rate	51
3.3.6	Chemical etching mechanism and comparison of pore etching with the bulk etch rate	52
3.4	Conclusion	53
4	Noise in ionic current through IBS nanopores	55
4.1	When noise <i>is</i> signal	55
4.2	Introduction to noise measurement	56
4.2.1	Spectral density estimation	56
4.3	Noise in all systems	59
4.3.1	Thermal noise	59
4.3.2	Capacitance	60
4.3.3	Shot noise	62
4.3.4	1/ <i>f</i> noise	63
4.3.5	Surface chemistry noise	64
4.4	Combining noise sources	65
4.5	Amplifier Noise	67
4.6	Comparison of noise between Ne and Xe fabricated pores	69
4.6.1	Methods	70
4.6.2	Material characterization	71
4.6.3	Noise results and discussion	77
4.7	Conclusion	80
4.8	Future work	81
5	Proof of DNA translocation through ion-beam sculpted nanopores	83
5.1	Motivation	83
5.2	Methods	84
5.3	Results and Discussion	86
5.4	Conclusion	86
6	Conclusion	88
	References	89
A	On the resolution limits of the nanopore method	99
A.1	Introduction	99
A.2	Model and Results	99
A.2.1	Simplified model the nanopore	99
A.2.2	Simplified model of DNA	99
A.2.3	Single molecule measurements	100
A.2.4	Signal to noise ratio	100

A.2.5	Statistical resolution limit	101
A.3	Discussion	103
A.4	Conclusion	105

List of Figures

- 1.1 A) Figure 1 from Coulter’s patent, the first publication related to the Coulter counter that inspired the nanopore concept. The constriction (component 23) is the ‘pore’ through which a particle would pass, causing a temporary blockage of current. B) Notebook sketch of the first DNA sequencing concept of nanopores from 1989 depicting a DNA molecule passing left to right through a cross section schematic of a nanopore. Below is the idealized current vs time trace depicting quantized current drops for each nucleotide. 1
- 1.2 A) Schematic view of the fluidic setup of the nanopore measurement system. Width of entire system is several centimeters. Polydimethylsiloxane (PDMS) chambers above and below the chip form a tight seal with the pore and contain conduits for fluid flow and DNA insertion. B) Schematic nanoscale view of DNA unfolding and passing from the top chamber through the pore to the bottom chamber. Pore diameters in this work are typically ≈ 10 nm. C) Representative current trace during a DNA translocation event. The DNA molecule causes a temporary current blockage of magnitude ΔI with duration τ_d 3
- 1.3 Idealized concept of signal due to the passing single-stranded DNA molecule passing through the pore, similar to Deamer’s sketch in Figure 1.1B. 3
- 1.4 Sensing region of the nanopore. The convergence of the electric field outside the pore contributes to the voltage drop and hence sensing region of the pore. Image drawn roughly to scale. 7

2.1	<p>Schematic of the nanopore fabrication process. 1) 275 nm of LPCVD low tensile, silicon rich, amorphous silicon nitride is deposited on both sides of a 380 μm silicon wafer. Only the cross section of a single chip is shown (not to scale). 2) Polymer etch mask is photolithographically defined with complete coverage on the bottom side and 579 μm SiN_x regions exposed. 3) RIE etch of SiN_x to expose the underlying silicon. 4) KOH wet etch along the $\langle 111 \rangle$ plane of the silicon, exposing a 30 μm freestanding SiN_x membrane. At this point the chip is further processed to produce ion beam sculpted nanopores or TEM drilled nanopores. 5i) Expanded ≈ 500 nm wide view of the center of the freestanding membrane where highly focused 50 keV Ga^+ ions sputter a large 100 nm hole. 6i) The chip is flipped over and bombarded with a broad parallel beam of noble gas ions at 3 keV, causing an accretion of mass at the top region at the side facing the beam. Ions that pass through the pore are counted by a ‘Channeltron’ style single ion counter. 5t) If TEM drilled pores are desired, a pit is drilled in the membrane similar to the IBS method, but stopped before drilling all the way through, leaving a region 20-90 nm thick. 6t) A 200-300 keV field emission TEM beam is converged on the sample to drill a nanopore, while imaging with a CCD detector below the sample.</p>	14
2.2	<p>Functional diagram of the ion-beam sculpting apparatus (IBSA).</p>	15
2.3	<p>A) Plan view TEM image of FIB milled hole in 250 nm thick SiN_x. Lighter areas imply thinner regions. Here, the light region in the center is the hole with no thickness. B) TEM image of 8 nm diameter nanopore after sculpting. The membrane formed by the IBS process is thinner and scatters the electron beam less, producing a lighter region than the surrounding membrane. C) Count rate vs. time for constant bombardment of ions for the pore depicted above. Inset is a detail of the last few seconds before the beam was deflected showing that the sculpting process was terminated before the pore closed completely to leave the 8 nm pore depicted in B).</p>	16

2.4	Experimental setup of nanopore experiment. Grey chambers are made of PDMS and simultaneously form a seal with the chip while holding the fluid chambers, fluid exchange tubing, and electrochemical electrodes. The outlet tube has been removed to add DNA molecules. For a sense of scale note that PDMS chambers are roughly 3 cm across.	18
2.5	Instrumentation used in nanopore experiment.	20
2.6	A) Current through nanopore before adding DNA. Nanopore has a diameter of 10 nm, salt solution 1 M KCl, applied bias 120 mV. B) 7 kbp dsDNA translocation events plotted as a function of time. For clarity, the data between events is not shown. Due to slight changes in conductivity of the solution before and after the addition of DNA, the open pore current increased once DNA was added.	21
2.7	Folded capture of DNA. 1) Unfolded capture and translocation of DNA producing, long, shallow events 2) DNA folded part way through the molecule producing a larger mean current drop and shorter translocation time than unfolded translocation 3) DNA folded half way along its contour length producing a current drop twice the current drop of the unfolded molecule and half the translocation time.	22
2.8	Black dots are a scatterplot depicting each event for an experiment as a single dot. Noted regions (1-3) refer to example events in Figure 2.7. Red histograms are histograms of all events in the scatterplot. Data were taken under the same conditions as in Figure 2.6. Events far outside this main group are typically attributed to spike-like noise and are typically removed from evaluation of translocation events. The dashed line is the constant ECD hyperbola $\Delta I = ECD\tau^{-1}$ with $ECD = 1800$ ions.	23
2.9	Call diagram for DNA7. The four main parts of DNA7 are highlighted in grey. The user interacts with the GUI to call the core program and event classifiers to produce graphs from the raw ABF files and then calls the data display subroutines to visually analyze the data.	26

2.10	The event shown here is likely a folded translocation similar to example (2) in Figure 2.7, but noise fluctuations just before and after the event, as well as an upswing within the event complicate analysis. Three short events are selected as possible events, by the event candidate trigger, but are rejected because they do not pass below the event-verify trigger level. The event start and end are defined by the point in time when the current falls below and above the top trigger level, respectively.	27
3.1	Geometry of ion-beam sculpted (IBS) nanopores. (A) Plan view TEM image of IBS nanopore. (B) Thickness map along solid line shown in TEM image (C) 3D tomogram reconstruction of the same pore.	41
3.2	(Top) Concatenated conductance drops for (Initial) DNA events just after wetting pore after etching and after dewetting and rewetting. (Middle) Measured TEM cross section and model geometries for the initial, etching, and dewetting stages of the same pore as shown in (Top). (Bottom left) Scatterplot showing conductance drop and translocation time for all events for the same pore as above before etching. (Bottom right) Normalized conductance drop histograms for all events from the same pore for the three stages shown above. The applied voltage for all stages was 240 mV.	44
3.3	(A) Bright field TEM image of a nanopore as fabricated in vacuum and (B) after wetting and translocation. Dotted line shows outline of pore and vestibule before wetting. (C) EFTEM derived thickness profile before and after wetting. To aid in comparison, thickness profiles were radially averaged then mirrored about the center point. Noise at the center of the pore is an artifact of the averaging process. .	45

3.4	(A) Idealized cylinder-cone-cylinder geometry of nanopores showing idealized mass loss model. (B) (open circles) Pore radius fit using Equation 3.4 from the measured conductance and initial pore geometry. (closed circles) Pore radius measured by TEM after wetting. (C) (open circles) Pore radius fit using Equation 3.7 from the measured conductance drop and initial pore geometry. (closed circles) Pore radius measured by TEM after wetting. Conductances measured at 120 mV.	49
3.5	Graph showing difference in pore radius predicted by pore conductance and conductance drop. Perfect agreement between the two methods would produce a line at 45°. Dashed line is a linear fit to the data. Solid dots denote pores with post wetting TEM images in Figure 3.4B	50
3.6	Increase in pore radius vs time calculated using Equation (3.4) for all fabrication methods tested.	51
4.1	A) Current measured through a ‘quiet’ nanopore at zero applied voltage and at 120 mV. Nanopore 19 nm diameter, 1M KCl pH 7.5, Tris-EDTA buffer. Digital 10 kHz lowpass filter. B) Current measured through a ‘noisy’ nanopore at zero applied voltage and at 120 mV. Nanopore 10 nm diameter, 1M KCl pH 7.5, Tris-EDTA buffer. Digital 10 kHz lowpass filter. Both pores shown here were fabricated with neon.	56
4.2	Power spectral density of current fluctuations through ‘noisy’ nanopore shown in Figure 4.1B	57
4.3	RC circuit model for noise analysis of nanopore. C_m is the membrane capacitance ≈ 10 pF, $R_{a,\infty}$ is the access resistance far from the pore, not including the spreading resistance adjacent to the pore and is typically <100 k Ω , $R_{p,t}$ is the total resistance of the nanopore and surrounding area, on the order of 10 M Ω . Chapter 3 deals extensively with the calculation $R_{p,t}$	61

4.4	The same PSDs for no bias and 120 mV applied bias as shown in Figure 4.2, but with theoretical noise contributions depicted. Note the log-log scale and that for nearly every frequency regime, the largest noise contribution dominates the spectrum. The fit demonstrated here is qualitative and parameters used to fit the data were selected manually, nonphysically low membrane capacitance C_p and high access resistance R_a were required. Roll-off after 100 kHz is due from 8-pole analog Bessel filter used while taking the data.	65
4.5	Power spectral density of current fluctuations through ‘quiet’ nanopore shown in Figure 4.1	67
4.6	Maximum relative RMS noise contribution of amplifier noise to nanopore measurement.	69
4.7	An XPS survey scan before and after annealing a SiN_x sample in air. The expected Si and N peaks are clear, along with the oxygen from a surface oxide formed before baking. This sample was also dosed with Xenon before baking.	72
4.8	The area under the intensity peak is proportional to the concentration of the element studied. Here, xenon is shown decreasing with increase in bake temperature. .	73
4.9	Relative change in silicon, nitrogen, and oxygen for a typical SiN_x sample. The sample was first baked for 1 hr at 600° C and then for 1hr at 1000° C	73
4.10	Relative change in neon, argon, and xenon imbedded in SiN_x . Each sample baked for 1 hr at 600° C and then for 1hr at 1000° C.	74
4.11	RBS spectrum demonstrating diffusion of argon out of pure SiO_2 sample after 1 hr annealing at 600° C. The silicon peak is due to silicon substrate and copper peak is due to the copper sample holder.	74
4.12	Relative change in concentration for embedded argon and xenon out of two separate SiN_x samples annealed in an inert argon atmosphere. Without an oxidizing agent, both argon and xenon are less mobile.	75
4.13	Depth profile of xenon embedded in SiN_x at 3 keV.	76

4.14	Example AFM topographies of sample before dosing with argon, after dosing, and after annealing. Scale bar for height shown on the right.	77
4.15	RMS noise over the 30 Hz to 5 kHz bandwidth for each pore measured at zero applied bias and 120 mV bias. Error bars unless shown are approximately the width of the marker and omitted for clarity.	78
4.16	Difference in noise measured at 120 mV and zero bias, each pore is represented by a single marker. Dashed line is a fit to data points with RMS noise less than 5pA.	79
4.17	Mean current through nanopores used in the noise study vs diameter as measured by TEM.	81
5.1	A) Density plot of current blockage events measured from the 1 kb dsDNA molecules. The average open pore current was $I_0=11 \pm 1.5$ nA during the time of the recording. We estimate the nanopore diameter is about 10 nm based on this open pore current. The most probable Current drop values are at 112 pA and 60 μ s. (B) Agarose gel electrophoresis to demonstrate that the 1 kb dsDNA traversed the solid state nanopore. Lane 1. Promega Corp. 1 kbp DNA ladder, Lane 2, Positive control for the <i>cis</i> chamber sample (10^8 X dilution), Lane 3, negative control with no template DNA, Lane 4, <i>trans</i> chamber solution before the DNA was added, Lane 5, <i>trans</i> sample collected after $\approx 40,000$ events were recorded. Photograph of the ethidium bromide-stained gel was taken using UV transillumination in a FluoroChem 8900 imaging system.	87
A.1	Theoretical ‘phase diagram’ depiction showing the measurement bandwidth required to measure translocation events as a function of SNR and event duration. Detection of shorter event durations require higher bandwidth and higher signal to noise ratio.	104

List of Tables

2.1	Oligomers used in the fabrication of ssDNA-dsDNA hybrid molecules	37
2.2	PCR reagents concentration. Total sample volume is 100 μL with remaining balance of autoclaved deionized water. Promega 'Taqman' Taq polymerase is sold in supplier defined units and is available in concentrations of 5 'units'/ μL . The dsDNA 1 kbp template is the amplified product of the dsDNA PCR protocol. An experimenter using this recipe is encouraged to modify the concentrations represented here to optimize the protocol for their purposes.	37
2.3	PCR thermocycler protocol. An experimenter using this recipe is encouraged to optimize this protocol for her or his purposes.	38
3.1	Etch rate for all fabrication methods tested. Errors are standard deviations. Three samples were measured for each fabrication method.	51
4.1	Mean penetration depth for ions embedded in SiN_x at 3 keV. Data from SRIM calculation from work previously done in our lab. Reference in the main text. . . .	75
4.2	Relative change in RMS roughness for samples dosed with argon and xenon. R_{pre} and R_{post} are the RMS roughnesses before and after noble gas dosing, respectively. R_{bake} is the RMS roughness after first dosing then annealing for 1 hour at 850° C. Typical values for R_{pre} are 0.80 nm.	76
5.1	PCR thermocycler protocol for <i>trans</i> dsDNA sample.	85
5.2	PCR reagents concentration. See 2.7.3 of Chapter 2 for descriptions of the reagents used. Add enough water to fill each PCR tube to 50 μL . For controls and the <i>trans</i> sample extracted after translocation 1 μL of solution was added. The <i>trans</i> sample extracted after translocation was not pre-diluted before addition.	85

Chapter 1

Introduction

1.1 Nanopore detection principle

Nanopores probe single DNA molecules using the resistive pulse method discovered by Walter Coulter in the 1940s [1, 2]. Coulter desired to automate the medically important, but tedious and error prone process of manually counting blood cells. In his invention, reproduced from his patent in Figure 1.1, two ionic solution filled chambers are separated by a short, narrow tube with diameter on the order of the cells to be analyzed. Through this tube an electric field is applied, producing an ‘open pore’ current of ions through the channel. Small non-conducting particles such as cells that pass through the tube decrease the current measured as a function of the particle size. This invention was wildly successful and led to the creation of an industry that thrives today.

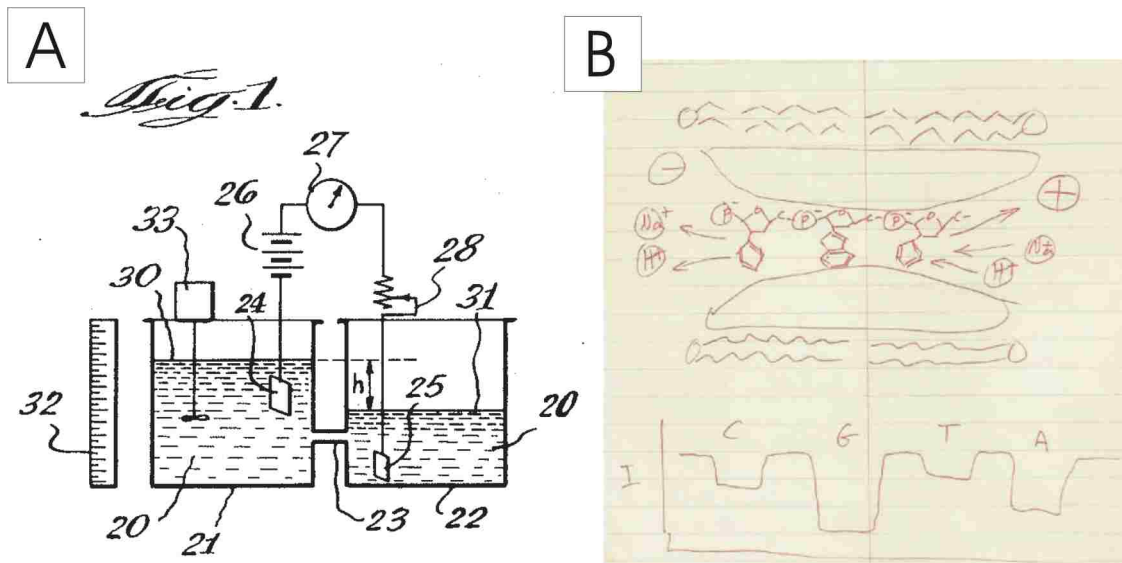


Figure 1.1: A) Figure 1 from Coulter’s patent, the first publication related to the Coulter counter that inspired the nanopore concept. The constriction (component 23) is the ‘pore’ through which a particle would pass, causing a temporary blockage of current. B) Notebook sketch of the first DNA sequencing concept of nanopores from 1989 depicting a DNA molecule passing left to right through a cross section schematic of a nanopore. Below is the idealized current vs time trace depicting quantized current drops for each nucleotide.

The idea to apply the Coulter counter to sequence DNA was independently proposed by David Deamer and George Church [3] as early as 1989 [4]. The sketch shown in Figure 1.1B from David Deamer's notebook shows a DNA molecule passing through a biological pore embedded in a lipid bilayer. Deamer's detailed depiction of DNA shows that each monomer consists of a ribose sugar and phosphate backbone attached to either an adenine, cytosine, thymine or guanine molecule. Each of these monomers have slightly different sizes that could possibly block the current in a sequence dependent manner as the molecule passed through the pore.

Because the diameter of DNA is 2.2 nm, nanopores, biological or synthetic, with diameters less than 10 nm and membrane thickness on the order of 10 nm have typically been investigated as the main sensing component for projects aimed at DNA sequencing. Figure 1.2A illustrates a typical nanopore sensing system as employed in this work. Similar to Coulter's original invention, a single pore is used as the sole electrical and fluidic connection between two electrolyte filled fluid chambers labeled in Figure 1.2A as *cis*, where the molecules start and *trans*, where the DNA pass or 'translocate' to. When a constant DC voltage is applied across Ag/AgCl electrodes connected to each chamber, a flow of ions through the nanopore creates a stable open pore ionic current on the order of pico to nano amperes.

When the electric field generated by the applied voltage drives a negatively charged DNA molecule through the nanopore, the molecule partially blocks the flow of the ions. Thus, the passing DNA molecule causes a transient resistance increase and resulting current decrease as shown in Figure 1.2C. The magnitude and duration of this transient current decrease contains information about the physical properties of the translocating DNA molecule such as its geometric dimensions and electrical charge density. In addition to the DNA molecule itself, the physical properties of the solution such as pH, conductivity, viscosity, and the dimensions of the nanopore also contribute to the characteristics of the current blockage signal. Figure 1.2C shows an example current blockage caused by a passing molecule. The ideal signal, suggested in Deamer's sketch and detailed more clearly in Figure 1.3, would produce a modulation of the current blockage as a function of the nucleotide within the nanopore, enabling a direct read-out of the sequence as the

molecule passed.

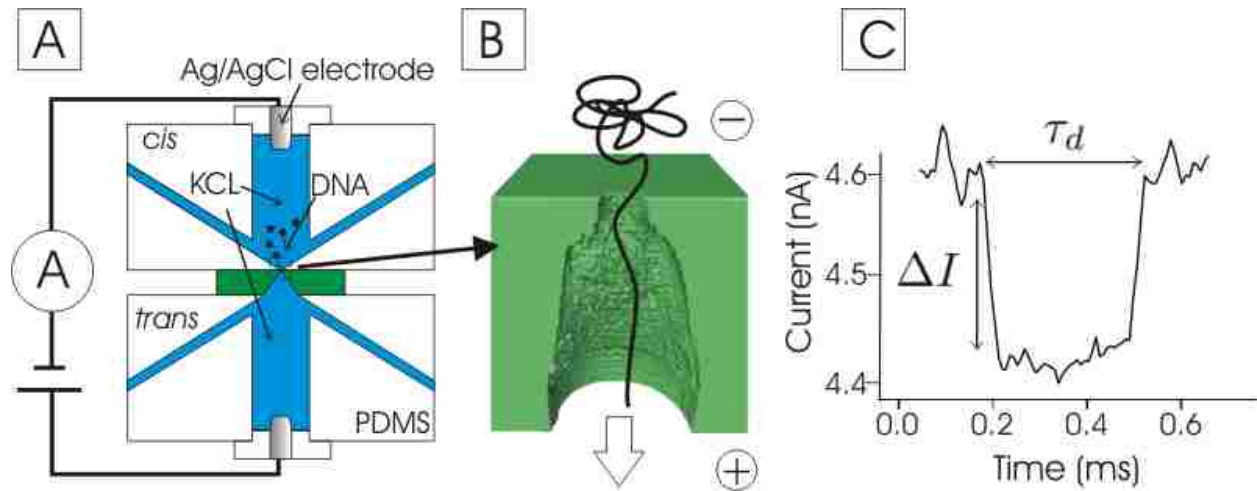


Figure 1.2: A) Schematic view of the fluidic setup of the nanopore measurement system. Width of entire system is several centimeters. Polydimethylsiloxane (PDMS) chambers above and below the chip form a tight seal with the pore and contain conduits for fluid flow and DNA insertion. B) Schematic nanoscale view of DNA unfolding and passing from the top chamber through the pore to the bottom chamber. Pore diameters in this work are typically ≈ 10 nm. C) Representative current trace during a DNA translocation event. The DNA molecule causes a temporary current blockage of magnitude ΔI with duration τ_d .

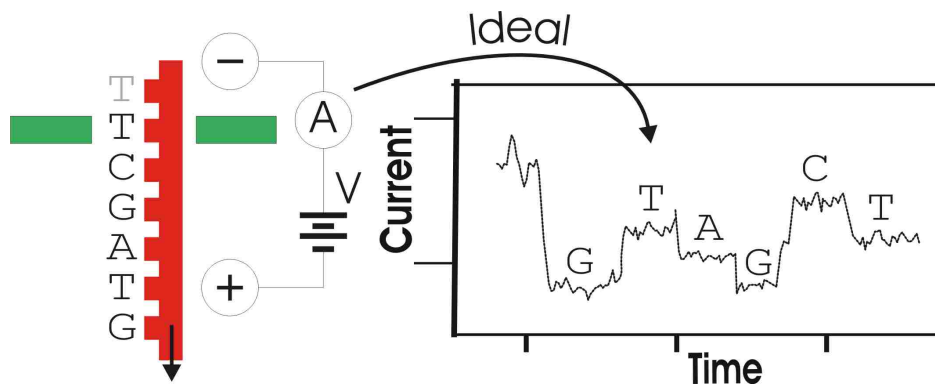


Figure 1.3: Idealized concept of signal due to the passing single-stranded DNA molecule passing through the pore, similar to Deamer's sketch in Figure 1.1B.

The earliest published work using any nanopore to probe polymers in solution used the alamethicin biological ion channel in 1994 [5]. In this study Bezrukov *et al.* detected a change in pore conductance with the addition of polyethylene glycol (PEG) molecules that were driven by diffusion through the pore; however, it was Kasianowicz *et al.* who in 1996 measured the time-resolved single-stranded DNA (ssDNA) and RNA homopolymer translocation through the alpha-hemolysin

channel, marking the beginning of single-molecule nanopore studies [6]. Several groups quickly began using alpha-hemolysin to detect the differences between different ssDNA and RNA homopolymers [6, 7]. The work of these groups showed that alpha-hemolysin could readily detect the difference between polyA and polyC RNA and even detect the difference between polyA and polyC regions on the same synthetically prepared molecules. However, the difference between polydA and polydC ssDNA was much smaller. It was concluded that the large variation in coiled secondary structure between polyA and polyC RNA, which the ssDNA homopolymers lacked, caused the large variations in current rather than the sequence itself. Their research and the research reviewed here and elsewhere [3, 8, 9] have proven the ability of biological pores to detect the secondary structure of biomolecules, but with only limited sequence information.

The development of solid state nanopores was driven by the desire to bring the promise shown by the alpha-hemolysin pore to a platform that could be fabricated with easy to manufacture, robust solid state materials. The first solid state nanopore that was able to detect single DNA molecule translocation was developed in the Harvard Nanopore Group using a unique process called ion-beam sculpting (IBS) [10, 11]. In this process a freestanding silicon rich (silicon in excess of stoichiometric) silicon nitride or silicon dioxide membrane is perforated by a high energy (50 keV) focused ion-beam mill or by electron beam lithography creating a single ≈ 100 nm hole through the membrane. Then the surrounding surface is bombarded by a low energy noble gas ion-beam, causing a very thin layer of matter to flow towards the hole [12, 13, 14]. Mechanisms to explain this counterintuitive shrinking include electrophoretic surface adatoms towards the hole by the electric field produced by ion deposited charge [11, 15, 16] as well as flow of a stressed viscous layer created by the embedded atoms [17]. During this process, ions that pass through the hole are detected after exiting the pore. The rate of ions passing through the pore decreases as the pore diameter shrinks, allowing the pore shrinking process to be monitored and the beam to be shut off when the pore reaches the desired area. By controlling the noble gas ion-beam species, flux, and energy, the pores dimensions can be sculpted to a radius of a few nanometers with a resolution of ≈ 1 nm, and a nanopore thickness of <10 nm. It is this method that is used to construct most of

the pores used in this work.

Shortly after the development of ion-beam sculpted pores, high energy electron beam sputtered silicon nitride and silicon oxide pores were developed [18]. In this method, a commercial TEM beam is focused on a freestanding membrane and beam conditions are set to controllably open or close the nanopore. This method has developed to the point that sub-nanometer radial resolution can be achieved [19, 20]. The TEM based fabrication methods have been the most often used, perhaps due to the availability of TEM equipment and the fine control of the pore radius.

1.2 Important nanopore parameters

The resistance of the pore is nearly ohmic and within an order of magnitude can be modeled as a cylinder of thickness t_p , radius r_p , with the bulk ionic solution conductivity σ [21]. At an applied voltage bias V across the pore, the open pore current can be summarized as

$$I_0 \approx V\sigma \frac{\pi r_p^2}{t_p}. \quad (1.1)$$

In solution at pH 7, the phosphate backbone of DNA is negatively charged to a linear charge density of -1 e/phosphate, producing a linear charge density along the DNA molecule of -2e/basepair (-5.9 e/nm). In an electrolyte solution the positively charged cations condense around the DNA to effectively screen the charge to ≈ -0.33 e/phosphate over a wide range of ionic strengths [22]. The net negative charge of a DNA molecule allows it to be driven by an electric field through the nanopore. The amplitude of the current blockage, $\Delta I = I_0 - I_b$, produced by a translocating DNA molecule increases with an increase in solution conductivity, voltage, and the cross sectional area excluded by the molecule [10], summarized as

$$\Delta I = I_0 - I_b \approx V\sigma \frac{\pi r_{DNA}^2}{t_p} \quad (1.2)$$

where r_{DNA} is the radius of a DNA molecule. This equation is simply the consequence of the DNA molecule reducing the cross sectional area available for ions to flow.

The duration of a current blockage event, on the other hand, is more complicated. It increases with increasing length of the DNA molecule and solution viscosity, and decreases at higher charge densities and applied voltage, represented approximately as [23, 24, 25]

$$\tau_d \approx \frac{\eta L^\alpha}{\lambda V} \quad (1.3)$$

where λ is the linear charge density, V is the applied voltage, and η is the solution viscosity. L is the contour length of the DNA molecule, defined as the end-to-end length of the DNA molecule if it were oriented in a straight line. The constant α has been measured to be between 1.2 and 1.4 for the larger diameter solid-state nanopores similar to those used in this study. The value $\alpha = 1.2$ can be derived using the Zimm model for polymer dynamics by assuming the DNA molecule interacts little with the membrane or the pore walls and that most of the length dependent drag on the molecule comes from the unwinding process as it is drawn through the pore [26]. Translocation time also decreases with an increase in pore radius, however, this dependence is not included in Equation (1.3) since this dependence is roughly constant for the pore sizes used here and are subsumed by the constant of proportionality [10, 25].

From these Equation (1.2) we can see that thinner pores are more desirable since they produce a greater current drop. Thinner pores also provide greater spatial resolution since fine details along the molecule that are shorter than the pore are effectively averaged out. The thinner the pore, the higher the fidelity of the current drop to the axial cross section variations caused by different bases. Decreasing pore thickness simultaneously increases signal and resolution, a rare occurrence indeed!

The pitch between basepairs on DNA are 0.34 nm, about the size a monolayer of atoms. The ideal pore therefore must be as close to a monolayer of atoms as possible. However, Equation (1.2) omits the influence of the access resistance region above and below the pore, as shown in Figure 1.4, caused by the convergence of electric field lines extended above and below the nanopore. These field lines produce a hemispherical sensing region with a radius roughly equal to that of the nanopore that defines the ultimate spatial resolution of the method [27, 28, 29, 30, 31]. Improved

models for ΔI that include these effects are covered in Chapter 3.

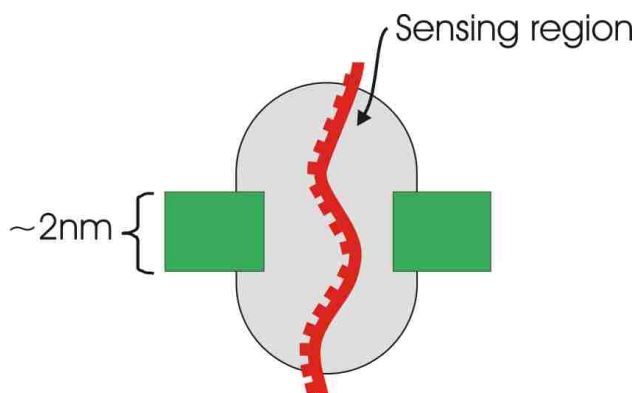


Figure 1.4: Sensing region of the nanopore. The convergence of the electric field outside the pore contributes to the voltage drop and hence sensing region of the pore. Image drawn roughly to scale.

To give a sense of the magnitude of the signals measured, consider that typical translocations have $\Delta I \approx 100$ pA and translocation times of $\tau_d \approx 300$ μ s for molecules roughly 10 kbp (10^3 basepairs) long. While measurement of changes in current for these durations is within the capabilities of modern electronics, this means that a single event will exclude on the order of 10^3 to 10^4 ions. Consequently, each ion excluded from translocation must provide for 1-10 nucleotides of sequence information, a daunting task! To surmount these challenges a variety of approaches have been taken by the nanopore community.

1.3 Recent developments in nanopore sequencing

1.3.1 Improving biological nanopores

Several engineered variants of the alpha-hemolysin protein pores have been developed to increase their sensitivity. By placing a single cysteine amino acid on the opening of an alpha-hemolysin pore, a short 5'-thiol modified DNA molecule, also called an oligomer, was attached by Howorka *et al.* [32]. This experimental setup allowed his group to sequence a three-basepair sequence of DNA at the end of the short covalently bound DNA molecule as it dangled into the narrowest constriction of the nanopore. By passing known sequences of DNA with varying end sequences, they found that exact matches had dwell times much longer than even single base mismatched

hybrids. Their method was limited to sequencing only three basepairs of the covalently bound oligomer, but their attachment chemistry helped open the door to the anchoring of enzymes to the pore to help slow the translocation rate of DNA.

Astier, Wu and others of the group of Prof. Bayley at the University of Oxford covalently attached an aminocyclodextrin molecule to the inner constriction of the alpha-hemolysin pore [33, 34]. They showed that the current of this mutant pore is modulated to four different levels as the four different deoxynucleoside monophosphates are driven through it one by one and in preliminary tests have been able to discriminate between bases at least 93% of the time. They envision attaching an exonuclease near the entrance of the pore that would cleave the DNA into a sequence of deoxynucleoside monophosphates that would be driven electrophoretically through the pore one at a time as they are removed.

In addition to alpha-hemolysin, in 2008, it was demonstrated that DNA translocations can be detected with the impressively robust *Mycobacterium smegmatis* porin A, MspA, biological transmembrane pore [35, 36]. In 2012 a significant achievement with this pore was achieved by slowing the translocation of DNA by a factor of $\approx 10^6$ while simultaneously measuring sequence specific current modulation [37]. This impressive feat was accomplished by pulling a single strand of DNA one basepair at a time through the MspA pore with the $\phi 29$ DNA polymerase.

1.3.2 Improving solid state nanopores

Solid state nanopores have lagged behind biological nanopores in their sequence sensitivity, but have now been fabricated atomically thin and have been used in the slowest translocations to date. In 2010 three groups nearly simultaneously demonstrated that nanopores fabricated from atomically thin graphene produce extremely large current drop signals, yet all groups reported extremely difficult fabrication requirements and high noise in their nanopores and only one report by Garaj *et al.* produced single layer graphene [38, 39, 40]. For SiN_x and SiO_2 pores, better characterization of the pore thickness has been reported [12, 19, 41, 42] and pore thicknesses of only a few nanometers can now be fabricated [42].

A variety of techniques have been employed to slow the translocation of DNA molecules including varying solution viscosity, temperature, and applied voltage for a ten fold increase in translocation time [21]. Still others have demonstrated the slowing and trapping of DNA in a nanopore by coupling DNA to a bead controlled by optical tweezers [43, 44]. In these experiments, researchers were able to repeatedly insert the tethered DNA molecule into the pore and pull it back out the same side it entered, demonstrating the possibility of resequencing a molecule with ultimate temporal control.

Dynamic control over the DNA translocation rate has been demonstrated by varying the voltage during the translocation [45, 46, 47]. In this technique, the driving voltage is reduced or shut off as a DNA hairpin is partially driven into a pore that is only large enough to allow ssDNA to translocate. The voltage is then increased at a constant rate and unzips the hairpin, pulling it through the pore. An interesting extension of this method is the ability to drive a molecule through the nanopore and after a complete translocation, reverse the polarity of the driving field and drive the same molecule back through the pore [48]. Although this method has not yet been used to slow the molecule, it presents a method for re-probing a molecule several times to increase the signal to noise ratio, with the possibility of re-probing sequences within a section of DNA without it leaving the pore.

1.3.3 Commercialization of nanopore sequencing

Progress has proceeded so far as for the creation of several companies seeking to commercialize the nanopore concept for sequencing. The company Oxford Nanopore Technologies Ltd. is working to commercialize biological and solid state nanopores for sequencing [49]. Nabsys Inc., seeks to combine the already proven ability of solid state nanopores to detect large tags at sequence specific regions separated by many hundreds or thousands of bases along the molecule that is complimentary to modern sequencing methods. International Business Machines (IBM) has also pursued research of a solid state nanopore with electrodes within the pore designed to ‘ratchet’ the DNA along the nanopore sensing region electronically one base at a time [49]. Despite the flurry of academic and industrial research, no device is commercially available to date.

1.4 Challenges addressed by this dissertation

The simple picture presented in Equations (1.1) and (1.2) produces current signals only within an order of magnitude of I_0 and ΔI . Computational solutions to the full 3D Poisson-Boltzman equation do no better since the error in prediction exists not in the physics of the current flow, but in the unknowns of the geometry. The result was a frustrating lack of predictability in measured current drop even when nanometer scale plan-view TEM images were available for the pore. It was felt that if there was any hope in modifying the nanopore geometry to increase current signals, a better understanding of the nanopore geometry fabricated by IBS was needed.

Chapter 3 addresses the challenge of predicting I_0 and ΔI from the full 3D size and geometry of the nanopore at nanoscale resolution using a method that can be performed routinely on modern TEM microscopes. Methods to produce 3D data had already been pioneered by labs working with TEM fabricated pores, but this method was performed for only a few pores and pore-to-pore variation provided predictions of current little better than those made originally. Another part of this challenge (that was often discussed at conferences but rarely discussed in the literature) was the stability of the nanopore once in solution. Frequently, pores would decrease in resistance over time in a manner unattributable to influences outside of the pore itself. A likely hypothesis was that the pore walls were dissolving while in solution, but verification in the literature was limited to a single report that focused on the final pore size rather than the rate of change [50]. By better understanding the relationship between current, current drop, and pore geometry, deviations over time could be related to changes in pore size in real time and etch rates could be determined. Because the ionic current depends quadratically on the pore radius, very small changes in radius cause clear changes in the current and allow very accurate dissolution rates to be measured.

Chapter 4 addresses the related issue of controlling noise sources in solid state nanopores. There are a variety of noise processes fundamental to current measurement, but there is also substantial pore-to-pore variability for low frequency noises that often obfuscate DNA translocation signals. In fact, it is the frequent occurrence of these noise sources that make nanopore research more of an ‘art’ than is desired. In the author’s experience, well over half of the nanopores fabri-

cated had noise levels far too high for measurement.

Preliminary work had shown differences in this low frequency noise depending on the fabrication method used to make IBS pores and it was hoped that by changing these parameters a possible mechanism for this enigmatic noise source could be found or at least controlled. Differences in surface chemistry and topography of the material surrounding the pore were explored. The final conclusion, however, was that changing fabrication parameters produced no systematic changes in noise and that a yet to be explained pore-to-pore variability was the cause of the differences in noise in the preliminary samples.

Chapter 5 addresses the long held assumption that the transient current blockages are evidence of DNA translocations through the pore. Unless independently verified, this assumption is far from certain and could be explained by a variety of means. The well characterized polymerase chain reaction is used as an independent verification to show that DNA does translocate through the pore.

1.5 Organization of this dissertation

This dissertation begins with an introduction to nanopore technology as applied to single-molecule studies, with a strong emphasis on solid state nanopores. In the introduction, I have made an attempt to combine a broad, brief historical view of this young field with an introduction to the most important physical parameters involved in the method. A more detailed introduction to the fabrication of nanopores and nanopore translocation experiments is presented in Chapter 2 which ends with highly technical and detailed protocols useful for experimenters wishing to reproduce or further the results presented here.

The remaining sections consist of three independently conducted but related projects. The core of this dissertation is Chapter 3 which presents novel information on the size, shape and stability of ion-beam sculpted nanopores and the relationship between these parameters and the measured current and DNA translocation current drop magnitudes. This information is used to determine the rate at which pore walls dissolve and to hypothesize a chemical dissolution mechanism consistent with the data.

Chapter 4 is more complicated as it presents a research project that failed to reproduce some preliminary work. For this project I studied the noise within the nanopore measurement with the hopes of finding ways to control that noise, however, I found in the end that there was no correlation with nanopore noise and the fabrication parameters I studied. During the project, I studied a wide array of fundamental noise sources within physical systems and I give a review of those noise sources in the nanopore. Data taken to characterize the pores and surrounding area using AFM and XPS is presented in the hope that it may be useful to future readers. However, since I was unable to control the noise, the characterization data could not be correlated to any effect.

Chapter 5 covers a very brief, successful project that shows DNA does in fact translocate through the nanopore. This was done to quell the concerns of a paper reviewer.

I conclude this dissertation with a brief summary of this work. The appendix to this dissertation builds upon the work of Chapter 3 and Chapter 4 to provide an interesting theoretical estimate of the limits of sensitivity of the nanopore method.

1.6 A note on source material

During my doctoral research I published two book chapters and several journal articles in the field of nanopore research and I have borrowed heavily from them for this dissertation. Reference [51], published in 2010 in *The Handbook of Plant Mutation Screening* is a review of the nanopore field up to that time and some sections are used in the introduction, reference [52], published in 2012 in *Nanopore-Based Technology* is a list of protocols, parts of which are used in Chapter 2. Parts of Chapter 3 are intended for publication in a peer reviewed scientific journal and sections may appear in such a journal in the future. Figures and text contributing to the supplemental information in reference [53] are used in Chapter 5. To the very best of my knowledge all other work is either unique to this dissertation or thoroughly referenced to the original source.

Chapter 2

Experimental setup and methods

2.1 Nanopore fabrication

2.1.1 Fabricating the freestanding membrane

In order to build a pore as the sole connection between two fluid reservoirs, a suitable membrane must be chosen. Ideally, this membrane should be mechanically robust, homogeneous, electrically insulating, and nearly chemically inert. In addition, materials that are well characterized and are easy to fabricate using the tools available in academic nanofabrication facilities would be ideal. One material that has been used in the semiconductor manufacturing industry for over four decades [54] and is readily available in academic nanofabrication facilities is low pressure chemical vapor deposited (LPCVD) silicon nitride. This material has the mechanical, electrical, and chemical properties that make it ideal for forming the thin freestanding membranes used in this work.

Working with a freestanding membrane thin enough for nanopore translocation requires a thicker substrate for support so that it can be handled by the experimenter. The procedure to accomplish this is discussed in detail elsewhere [55]. In brief, a 380 μm thick silicon wafer is covered on both sides with 275 nm LPCVD low tensile stress silicon rich silicon nitride. A polymer based mask is photolithographically defined on one side, features on one side of the SiN_x are reactive ion etched (RIEd) and then wet etched with 30% w/v KOH at 90°C to produce pyramid-shaped recesses that release a roughly 30 μm x 30 μm freestanding membrane of SiN_x 275 nm thick.

2.1.2 Ion-beam sculpting (IBS)

Once the freestanding membrane is prepared, a submicron hole is formed in the center by focused ion beam (FIB) milling producing the hole shown in Figure 2.3A. A single chip containing the membrane is loaded into the ion-beam sculpting apparatus (IBSA) where a broad 100 μm to 1

Freestanding membrane fabrication

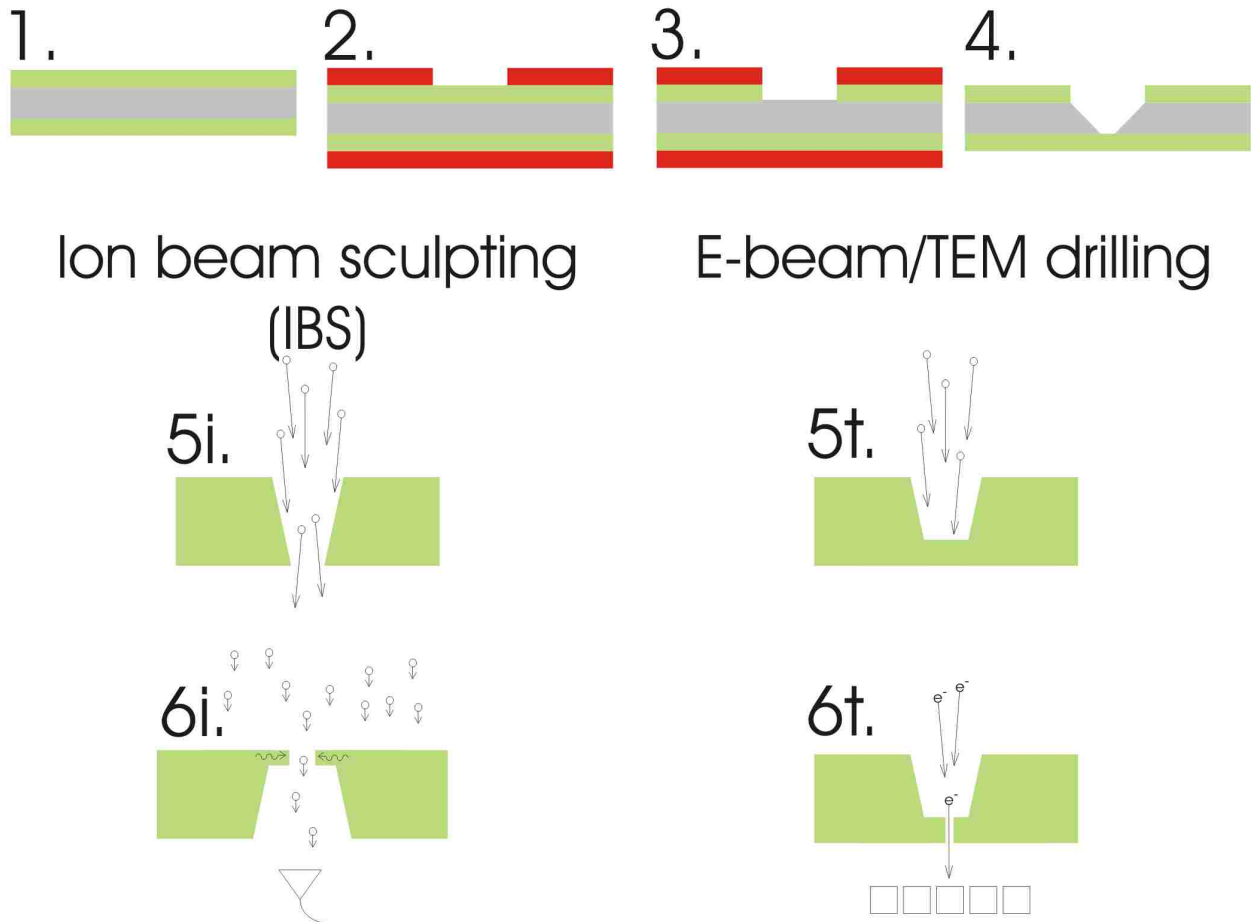


Figure 2.1: Schematic of the nanopore fabrication process. 1) 275 nm of LPCVD low tensile, silicon rich, amorphous silicon nitride is deposited on both sides of a 380 μm silicon wafer. Only the cross section of a single chip is shown (not to scale). 2) Polymer etch mask is photolithographically defined with complete coverage on the bottom side and 579 μm SiN_x regions exposed. 3) RIE etch of SiN_x to expose the underlying silicon. 4) KOH wet etch along the $\langle 111 \rangle$ plane of the silicon, exposing a 30 μm freestanding SiN_x membrane. At this point the chip is further processed to produce ion beam sculpted nanopores or TEM drilled nanopores. 5i) Expanded ≈ 500 nm wide view of the center of the freestanding membrane where highly focused 50 keV Ga⁺ ions sputter a large 100 nm hole. 6i) The chip is flipped over and bombarded with a broad parallel beam of noble gas ions at 3 keV, causing an accretion of mass at the top region at the side facing the beam. Ions that pass through the pore are counted by a 'Channeltron' style single ion counter. 5t) If TEM drilled pores are desired, a pit is drilled in the membrane similar to the IBS method, but stopped before drilling all the way through, leaving a region 20-90 nm thick. 6t) A 200-300 keV field emission TEM beam is converged on the sample to drill a nanopore, while imaging with a CCD detector below the sample.

mm diameter, 3 keV beam of noble gas ions are projected on the surface. The general layout of the IBSA is shown in Figure 2.2. A more complete description is given elsewhere by Dr. Derek Stein *et al.* [14]. Depending upon the gas used [12], membrane temperature [16], beam pulse rate, duty cycle, and flux [13], the accelerated ions cause a lateral flow of mass that shrinks the size of the nanopore as shown in Figure 2.3B. Recent work by Kuan [42] and novel work presented in Chapter 3 of this dissertation show that this flow of material happens only at the top of the nanopore, producing a much thinner membrane surrounding the pore. Ions that pass through the FIB hole are focused by an electrostatic Einzel lens through an electrostatic ion energy analyzer that selects zero loss ions onto a ‘channeltron’ style single ion detector. Small current pulses from this device are amplified and counted and are plotted in real time as shown in Figure 2.3C, allowing a computer controlled high voltage switch to deflect the beam once the nanopore has reached the desired size. A low energy flood of electrons is used to neutralize charge built up by the ion beam on the SiN_x surface.

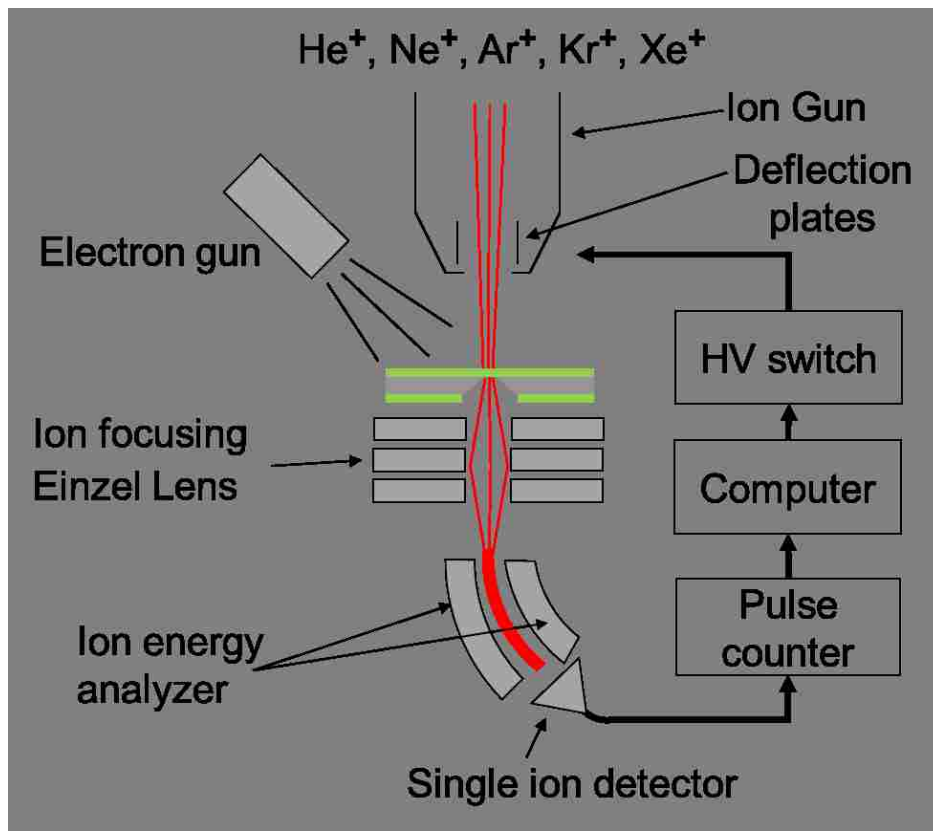


Figure 2.2: Functional diagram of the ion-beam sculpting apparatus (IBSA).

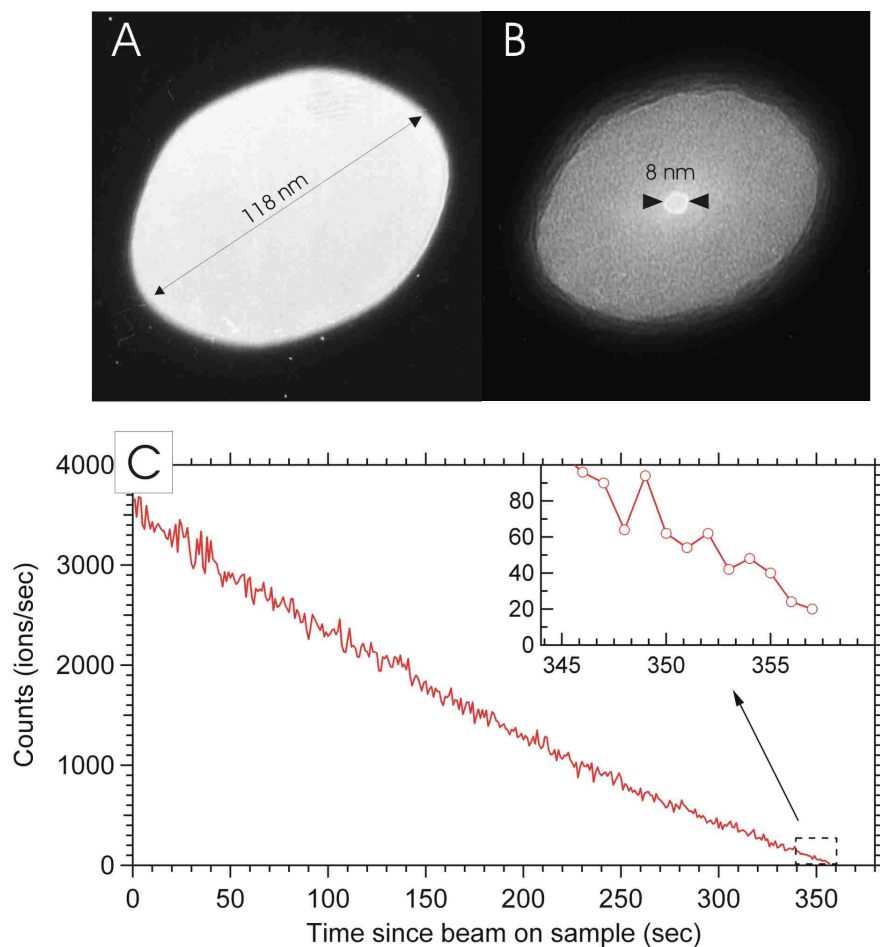


Figure 2.3: A) Plan view TEM image of FIB milled hole in 250 nm thick SiN_x . Lighter areas imply thinner regions. Here, the light region in the center is the hole with no thickness. B) TEM image of 8 nm diameter nanopore after sculpting. The membrane formed by the IBS process is thinner and scatters the electron beam less, producing a lighter region than the surrounding membrane. C) Count rate vs. time for constant bombardment of ions for the pore depicted above. Inset is a detail of the last few seconds before the beam was deflected showing that the sculpting process was terminated before the pore closed completely to leave the 8 nm pore depicted in B).

2.1.3 TEM drilling

Because details on TEM drilled nanopores are thoroughly documented in the literature, [56, 19, 18] and were not the primary method for nanopore fabrication in this dissertation, TEM fabrication of nanopores is discussed only briefly here.

TEM drilling of the nanopore is more straightforward than the IBS process. Once the free-standing membrane is complete, the FIB is used to mill a pit leaving less than 100 nm of SiN_x. The sample is placed inside a commercial high current density field emission TEM system, such as the modern FEI Tecnai or FEI Titan at the University of Arkansas where the condensing system is used to converge the beam with a full width at half maximum intensity of a few nanometers. The user observes the image of the membrane until a nanopore breaks through and reaches the desired size. Experimenters interested in TEM related methods are directed to a thorough introduction of the anatomy and function of the TEM presented in the excellent book by Williams and Carter [57].

2.2 Fluidic system

In order to interface the nanopore with fluid and enable current measurement, a fluidic gasket and chamber is made from polydimethylsiloxane (PDMS). PDMS is a silicon based elastomer that is very easy to pour into molds and is highly solvent resistant [58]. Two identical chambers are fabricated and placed on either side of the pore, termed the *cis* for the side the DNA is inserted on and *trans* as the side to which the DNA translocates. The chamber simultaneously provides a tight seal to contain the liquid and provide a pathway for fluid flow and electrode insertion. Custom fabricated Ag/AgCl electrodes and fluid inlets and outlets are press fit into the PDMS chamber to form a stable, portable nanopore holder that is robust to vibration and rotation. In this setup experiments can be conducted in any orientation with respect to gravity.

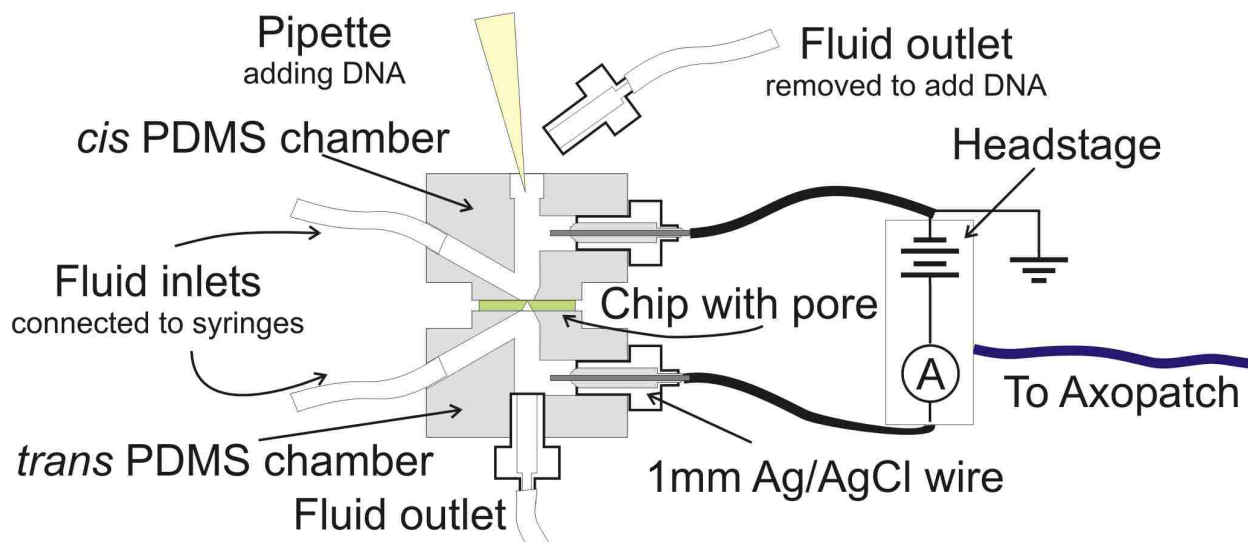
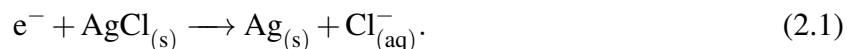


Figure 2.4: Experimental setup of nanopore experiment. Grey chambers are made of PDMS and simultaneously form a seal with the chip while holding the fluid chambers, fluid exchange tubing, and electrochemical electrodes. The outlet tube has been removed to add DNA molecules. For a sense of scale note that PDMS chambers are roughly 3 cm across.

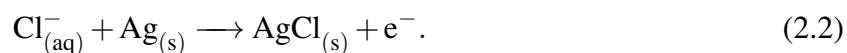
2.3 Current measurement

2.3.1 Electrochemistry

The current carrying element in the nanopore experiments in this work consists of the charged ions K^+ and Cl^- . Charge transfer between a solid anode and cathode through an ionic solution requires a chemical reaction that transfers the charge of the electron in the metal electronics to an ion in solution at the cathode and the reverse at the anode. A simple and widely used reaction in solutions containing chloride anions is the Ag/AgCl electrode. At the cathode, an electron supplied by the outside circuit causes the reaction



Chloride ions in solution at the anode complete the circuit through the reaction



Of particular concern in electrochemical experiments is the electrode potential between an electrode and the solution. Ag/AgCl electrodes have stable, Nernstian electrode potentials that depend on the local chloride ion concentration at the electrode. For nanopore experiments in this work, KCl and hence chloride ion concentrations were kept the same at both electrodes. Theoretically, the electrode potentials between each electrode and solution would cancel, resulting in no current flow without an applied bias, but small non-ideal differences in electrode chemistry can produce different electrode potentials at each electrode that turn the electrode-electrolyte system into a weak battery. For the electrodes used in these nanopore experiments, current was frequently observed at zero applied bias at the beginning of an experiment. This was attributed to differences in electrode potential due to the non-ideal chemical makeup of the electrodes. These potential offsets were measured to be on order of 5 mV and would drift by as much as a factor of 2 over several hours. To counter this effect, a voltage of equal magnitude but opposite sign was applied to zero the current before any currents were measured.

2.3.2 Electronics

The primary tool for all research involving ionic current through the nanopore was the Axopatch 200B capacitor/resistor feedback patch clamp amplifier manufactured by Molecular Devices. The device consists of two parts, an analog amplifier headstage (CV 203BU), and a rack mounted signal conditioning controller. This device is capable of controlling voltage (voltage clamping) or current (current clamping) and has a wide range of analog circuitry that is suitable for the high capacitance, picoampere range currents using capacitive feedback, but is user switchable to operate in low capacitance, nanoampere current range suitable for nanopore research. The noise over the entire 100 kHz measurement bandwidth was extremely low (see Chapter 4 for a detailed discussion).

Control of the experiment was done by a Windows 2000 PC running Clampfit 9 in conjunction with the Digidata 1233A, both by Molecular Devices. The voltage to be applied to the nanopore, termed the command voltage V_c was set either digitally by the PC as shown in Figure 2.5 or manually using the potentiometer interface on the Axopatch. When used, the digital output from the PC

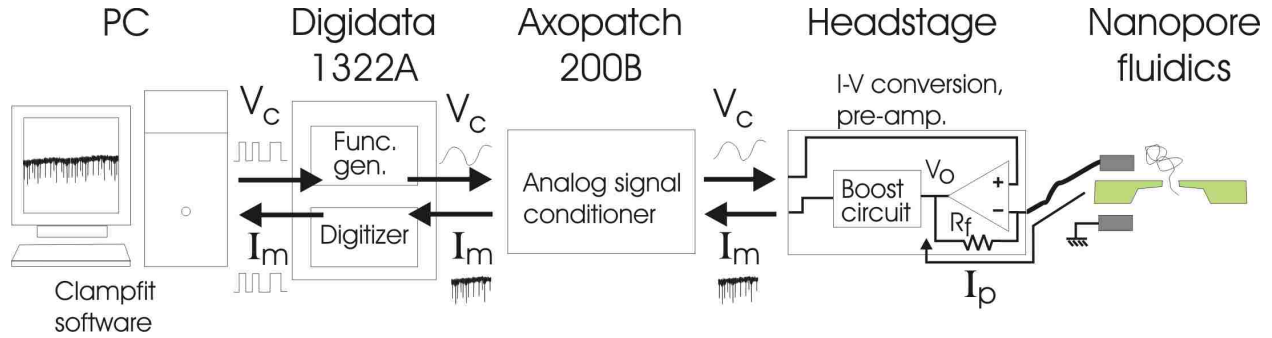


Figure 2.5: Instrumentation used in nanopore experiment.

computer was converted to an analog waveform – typically a DC voltage – by the digitizer build into the Digidata before passing through the voltage scaling and manually applied offset by the Axopatch. The analog signal was then sent to the non-inverting input of the operational amplifier located within the headstage which applied V_c and measured the current I_p passing through the pore. Output from the first amplification stage was the voltage V_0 . In the configuration shown, the output voltage follows the current with a gain factor defined by the feedback resistor R_f and offset by the command voltage as shown by

$$V_0 = V_c + I_p R_f. \quad (2.3)$$

The headstage has two electronically selectable feedback resistors of $50 \text{ M}\Omega$ and $500 \text{ M}\Omega$ for initial amplification of the signal. A fundamental limitation of a transimpedance amplifier in this configuration is the limited bandwidth associated from stray capacitances and capacitances required to keep the circuit operating without overshoot. To compensate for this effect, the voltage signal was further conditioned using the boost circuit which implemented frequency dependent gain and signal offset circuitry to produce a voltage signal I_m that was directly proportional to the nanopore current I_p with uniform gain over an approximately 250 kHz bandwidth. From there, the Digidata digitized the signal and sent it to the PC for storage and oscilloscope-like output to visually monitor the experiment.

2.4 DNA translocation

Once the pore is wet, an applied voltage bias produces a steady state current as shown in Figure 2.6A. DNA is then added, producing the transient current blockages depicted in Figure 2.6B.

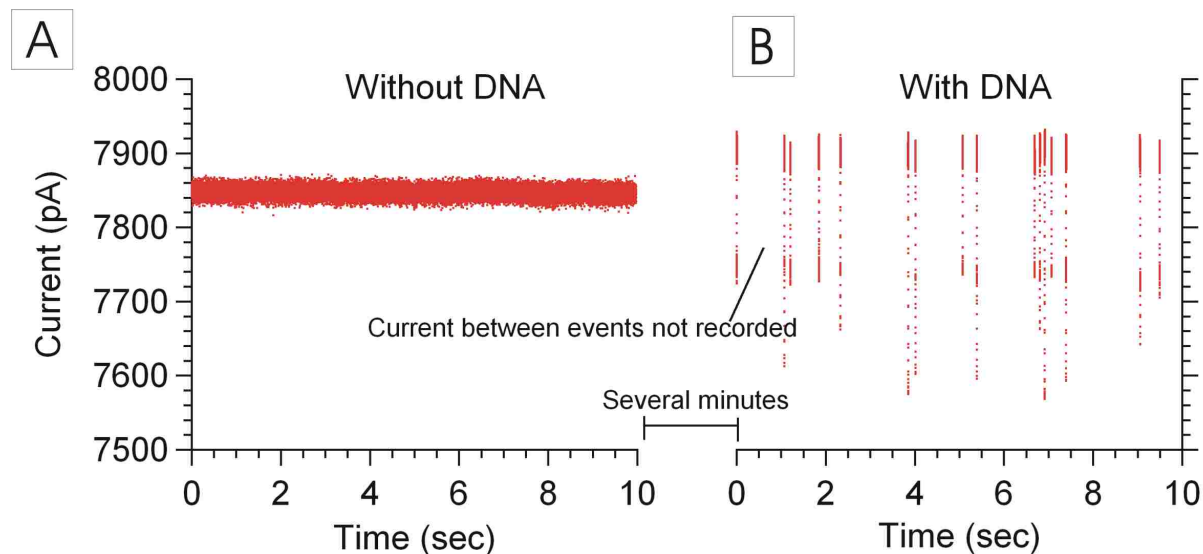


Figure 2.6: A) Current through nanopore before adding DNA. Nanopore has a diameter of 10 nm, salt solution 1 M KCl, applied bias 120 mV. B) 7 kbp dsDNA translocation events plotted as a function of time. For clarity, the data between events is not shown. Due to slight changes in conductivity of the solution before and after the addition of DNA, the open pore current increased once DNA was added.

The covalent bonding and high charge along the backbone prevent the molecule from bending and twisting over short length scales, producing a polymer that is rigid and resistant to thermal fluctuations on the nanoscale. This stiffness of a polymer can be characterized by its persistence length, which is the length over which the direction of the tangent vector along the contour of the polymer is highly correlated. In other words, the orientation of two small sections of the molecule separated by one persistence length are uncorrelated. For DNA, the persistence length is 50 nm, much larger than most of the nanopores used in this work. The DNA used for most of this work is 7×10^3 base pairs long (abbreviated as 7 kbp). Each base pair is separated by 0.34 nm along the axis of the molecule, producing a contour length of $\approx 2.4 \mu\text{m}$, far longer than the persistence length, producing multiple bends and folds as it diffuses to the nanopore. This folded molecule diffuses through solution until a random point along the molecule comes close enough to the pore

to be pulled through. Recent work has shown that the number of conformations available to the molecule counter-intuitively favor the molecule being captured in an unfolded state [59].

Close inspection of the translocation events reveals two current drop levels due to the folding of the DNA molecule as it is captured by the pore. Examples of three different folded capture configurations are shown in Figure 2.7. Example (1) shows end-to-end translocation, producing the smallest current drop and the longest translocation time. Examples (2) and (3) are folded events with the fold in (2) occurring in the first half of the molecule and the fold in (3) occurring at halfway through the molecule. Folding as shown in (2) clearly has two current drop levels, complicating the definition of the current drop. For this work we define ΔI as the mean current drop for the entire event since this definition best preserves the approximation in equation 2.4 discussed next.

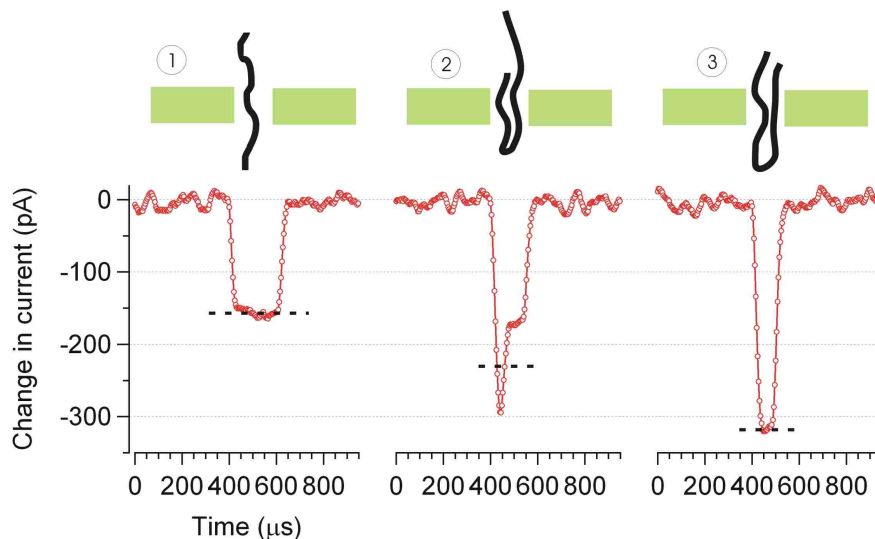


Figure 2.7: Folded capture of DNA. 1) Unfolded capture and translocation of DNA producing, long, shallow events 2) DNA folded part way through the molecule producing a larger mean current drop and shorter translocation time than unfolded translocation 3) DNA folded half way along its contour length producing a current drop twice the current drop of the unfolded molecule and half the translocation time.

Much of what has been discussed so far can be observed at a glance in the scatter plots and histograms shown in Figure 2.8. Each event is plotted as a single point defined by its translocation time and mean current drop. Most events, regardless of folding position fall along a hyperbola defined by $\Delta I \tau_d \approx const..$ This constant is called the Event Charge Deficit (ECD) and is the number of ions stopped from passing through the nanopore due to the presence of the DNA molecule. As

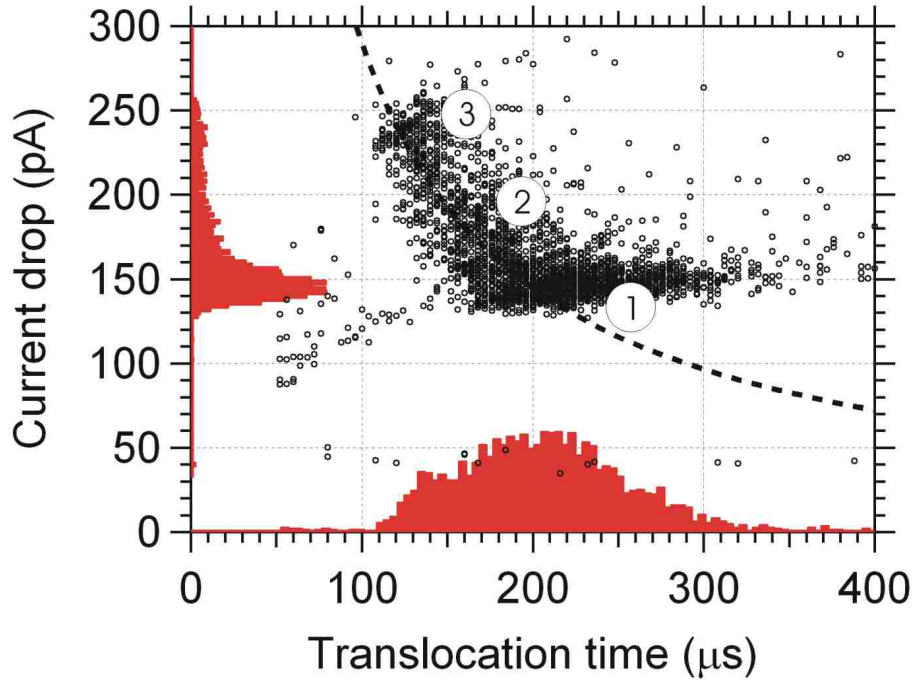


Figure 2.8: Black dots are a scatterplot depicting each event for an experiment as a single dot. Noted regions (1-3) refer to example events in Figure 2.7. Red histograms are histograms of all events in the scatterplot. Data were taken under the same conditions as in Figure 2.6. Events far outside this main group are typically attributed to spike-like noise and are typically removed from evaluation of translocation events. The dashed line is the constant ECD hyperbola $\Delta I = ECD\tau^{-1}$ with $ECD = 1800$ ions.

events fold, they effectively become shorter and, assuming that all DNA translocates at the same velocity, the ECD is the same for all events [10, 24]. Precise calculation of the ECD is done by integrating the difference between the baseline current and the current during the event, namely

$$ECD = \int (I_0 - I(t)) dt \approx \Delta I \tau_d. \quad (2.4)$$

where the integration limits are from the beginning to the end of the event. Taking the integral of each event, we find an average ECD of 1800 ions. The hyperbola $\Delta I = ECD\tau^{-1}$ is the dashed line passing through the scatterplot in Figure 2.8.

Several deviations from this ideal behavior are clear. Thermal forces intuitively produce variations in measured velocity, but the measured deviations are much larger than those expected from the constant velocity electrophoretic translocation time of a rigid rod [60]. Since the radius of

gyration of the DNA molecule is much larger than the nanopore, it must first unwind, producing a larger spread in translocation time. This spread decreases as the position of the fold approaches the center of the molecule, possibly due to the fact that there are fewer initial conformations available to the shorter parts of the molecule outside the pore as translocation begins.

2.5 Data analysis

In order to avoid handling very large files, only the current during the event and several milliseconds surrounding the event are saved; data between events are discarded. To achieve this, current is measured continuously, but only the few most recent milliseconds of data are buffered at any moment in time. When the current drops below a user defined current trigger level, the buffered data is committed to nonvolatile memory and the incoming data is recorded until the current returns back above the trigger level. After this point, several more milliseconds of data are saved before the trigger resets and waits for another event. The resulting data file consists of the current measured for the event and a timestamp for each event recording the time at which the event began. This data is stored using pClamp 9 as a binary file in the proprietary Axon Binary File (ABF) format.

This method of capturing events only works well when the current drops are large compared to the noise of the measurement and often contains undulations in current that are better classified as noise, requiring further processing. Parsing the proprietary ABF format for the extraction and investigation of events is done with a suite of programs written in MATLAB. Two program suites are used to process the data, called Adjust4 and DNA7. Nearly all parts of these programs have been modified and updated, building upon previous contributions from former lab members Dr. James Uplinger and John Wong and the lab of Prof. Golovchenko at Harvard University.

Originally written by Dr. James Uplinger, Adjust4 removes the majority of low-frequency noise and current drift by assuming that the baseline current does not change over the few millisecond time period immediately before and after the triggered event. The baseline immediately before or after each event is determined and the event is shifted to a user defined baseline. This produces events that are largely free of slow drifts and noise in the few Hz range and less. This program

has been expanded in its baseline detection algorithms and batch processing, making the program more versatile.

Originally developed at Harvard University, DNA7 is a more complicated suite of programs centered around a graphical user interface (GUI) that allows users to analyze their data without any programming knowledge. Because of its complexity and the shifting needs of research, modules have been added and the core routines changed to keep up with the needs of the lab. As depicted in Figure 2.9, DNA7 consists of nearly 40 subroutines, consisting mainly of four important groups: the GUI, the core program, the event classifiers, and the data display and output.

The user accesses her or his raw ABF file using the GUI and chooses a series of analysis parameters to submit to the core program. The core program contains subroutines that re-classify the events saved in the ABF file using a more discerning double trigger level method shown in Figure 2.10. The top trigger level performs two actions. First, any current that falls below this level is considered a candidate event. Second, the two times at which the current crosses this trigger level define the start and end of the event. Data that falls below the lower trigger level is considered a valid event and can be used for further processing. An important point is that if only one trigger level were used, for example at the level of the event verify trigger, the duration of the event would be artificially shortened. This is of negligible importance for events with very fast rise and fall times, however, as shown in this example, many events would have translocation times that would be artificially shortened by a non-negligible fraction. Finally, the user has the flexibility to use either trigger levels to define which data points are appropriate to find the mean current drop.

2.6 Translocation protocols

The following section is a collection of technically detailed protocols and some informal discussion meant for experimentalists in the field. It is arranged in the order one would perform a DNA translocation experiment assuming that a nanopore has already been fabricated. Experimenters interested in reviewing the IBS nanopore fabrication process are directed to the masters thesis of Dr. Bradley Ledden [55] and the protocol book chapter I coauthored found in reference [52].

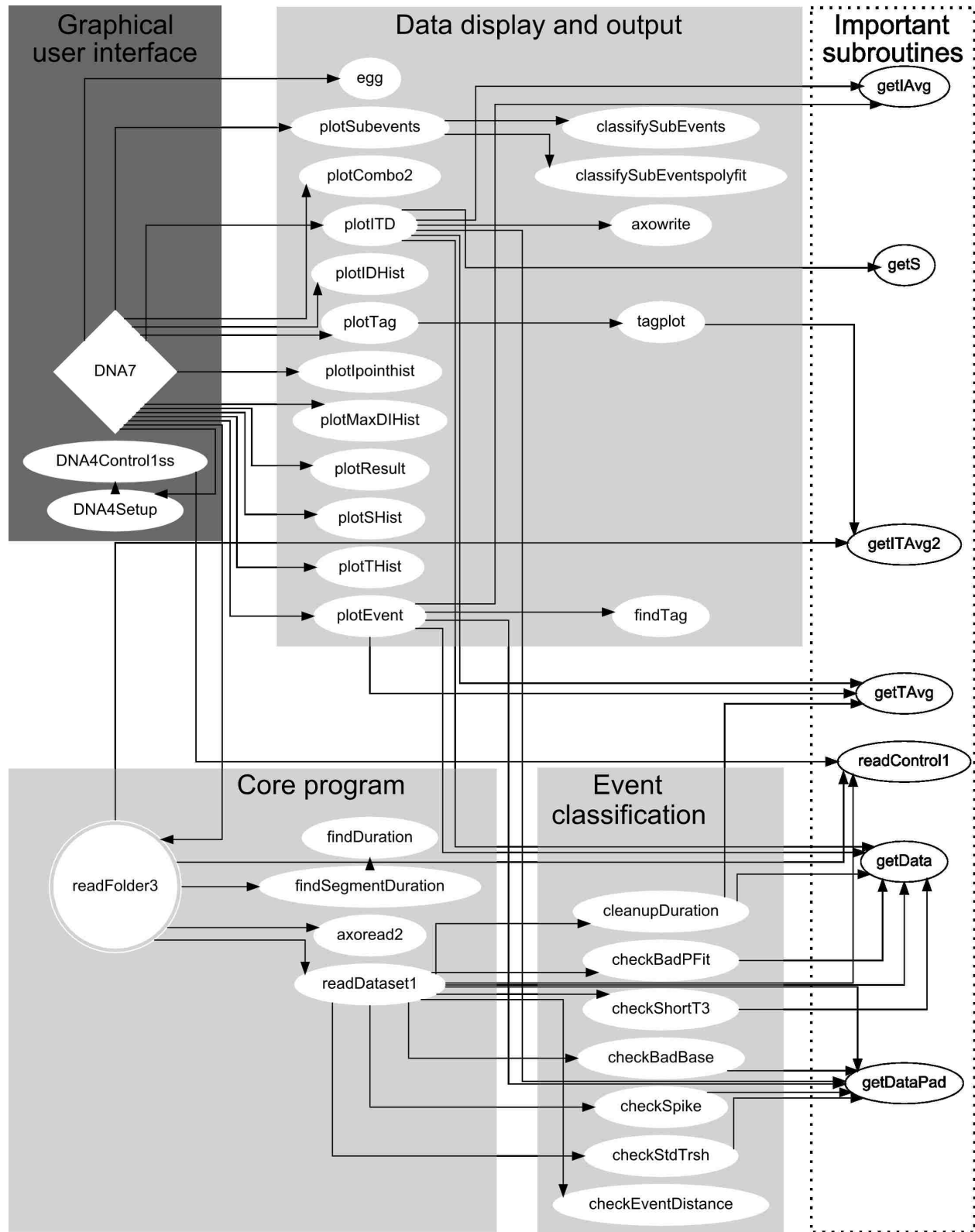


Figure 2.9: Call diagram for DNA7. The four main parts of DNA7 are highlighted in grey. The user interacts with the GUI to call the core program and event classifiers to produce graphs from the raw ABF files and then calls the data display subroutines to visually analyze the data.

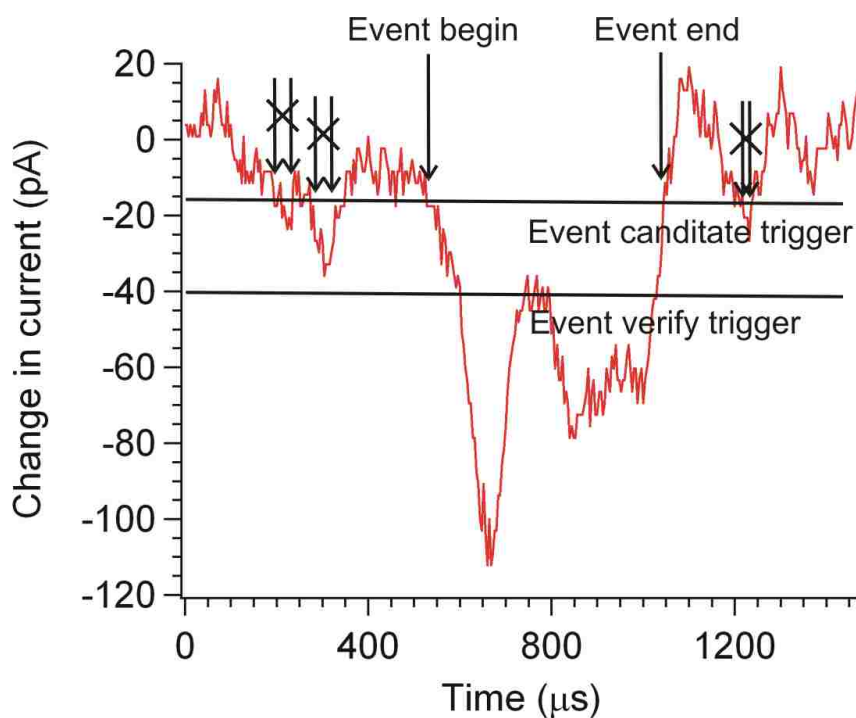


Figure 2.10: The event shown here is likely a folded translocation similar to example (2) in Figure 2.7, but noise fluctuations just before and after the event, as well as an upswing within the event complicate analysis. Three short events are selected as possible events, by the event candidate trigger, but are rejected because they do not pass below the event-verify trigger level. The event start and end are defined by the point in time when the current falls below and above the top trigger level, respectively.

2.6.1 Storage of pore before experiment

In order to perform conductance measurements and single molecule translocation experiments, the pore must transition from the high vacuum environment where it was fabricated and be wet by solution. Typically, the chip containing the pore is stored for anywhere from days to months in a dry box at atmospheric pressure with humidities kept below 20%. Pores were typically stored in lab fabricated versions of the popular Gel-Pak boxes used for TEM sample storage.

There has been some debate in our lab and among collaborators at the Harvard nanopore lab about an aging process during pore storage. Because of the frequent failure and high noise of nanopores and a general feeling in the lab that newer pores performed better, we investigated possible aging mechanisms. SiN_x is considered chemically stable and is used as an oxidation mask in semiconductor fabrication, but it has been known since at least 1976 that chemical vapor deposited

SiN_x similar to ours form an oxide layer upon exposure to air at room temperature for as little as 3 days with layers on the order of 1 nm forming after a month [61]. Using X-ray photoelectron spectroscopy of virgin SiN_x exposed by ion beam sputtering in high vacuum, we discovered qualitative evidence for the presence of oxygen throughout the LPCVD deposited SiN_x with concentrations of a few percent. A conversation with the deposition team at Cornell verified that oxygen concentrations of this level are typical of nitrides they deposit. Thus, understanding any changes in the material surface reacting with air would need to be divorced from the native oxides and no conclusions were made. Other possible aging processes are coatings due to carbonaceous material in the air, a strong source of which would be the outgassed plasticizers. XPS scans frequently showed trace carbon contamination typical of most samples studied by XPS. Future work investigating this material and correlating pore failure with age will probably need more thorough XPS measurements to discover any chemical changes materials coating the chip surface and TEM-EELS measurements at the pore surface to see if these materials and coatings are present at the pore. This engineering research would be of great import to the eventual use of solid state nanopores as practical devices.

2.6.2 PDMS chamber fabrication

To fabricate the chambers, our mold design uses stainless steel machine pins of the diameter desired for the interior chambers that can slide through holes in a mold machined from aluminum or plastic. In order for the PDMS chambers to press against the SiN surface and form a seal, holders with clamps are needed to press the PDMS components together.

1. Prepare PDMS: hardener mixture in a 10:1 ratio by mass and stir until well mixed in disposable plastic cup.
2. Place PDMS in bell jar for approximately 20 min under vacuum or until all bubbles are gone.
3. While degassing, clean mold. An aluminum mold can be sonicated in acetone for 15 min. followed by isopropyl alcohol for 15 min.

4. Assemble mold with pins in place and pour degassed PDMS over mold. Bubbles that form while pouring can be removed with a pipette tip.
5. Heat mold at 70° C for 3 hours.
6. Disassemble mold by first removing the pins, and then forcing out the molded part.
7. Using a dissecting microscope, narrow tip tweezers, and sharp hypodermic needle as a cutting tool, clean up any unwanted films or other artifacts.
8. Clean fluid chamber by sonicating in 10% ethanol for 15 minutes. Ethanol is added for weak cleaning and to wet the interior of the PDMS. Replace solution with 18 MΩ water and sonicate for 15 minutes.
9. Blow dry chambers with clean N₂ and store in clean place until ready to use.

2.6.3 Electrode fabrication

Electrodes suitable for single molecule experiments can easily be fabricated in the laboratory. In the fabrication procedure described below, care must be taken to ensure proper sealing between PDMS potting material and silver wire since electrochemical reactions between Ag and the solution can produce electrochemical potentials.

1. Insert enough Ag wire into the Luer-Lock fitting such that it fits several millimeters past the end of the Luer-Lock head.
2. Use laboratory tape to affix the end to be soldered to the Luer-Lock in a water tight fashion.
3. Mix and degas several grams of PDMS similar to chamber fabrication procedure and fill the empty space between the Luer-Lock interior and the electrode with unhardened PDMS. Arrange the Luer-Lock fitting so that it holds the PDMS in a cup-like fashion.
4. Heat electrode head in an oven at 70°C for 3 hours, or leave at least a week at room temperature.

5. Solder and heat shrink about 10 cm of thin, flexible wire to the small end of the electrode head.
6. On the opposing side of the wire, solder a 1 mm diameter male pin to mate the electrode with the headstage.
7. Sand the Ag electrode tip with fine sandpaper, 600 grit works well.
8. Sonicate the Ag electrode head in 18 M Ω water for 15 minutes.
9. Bleach the Ag tip in household Clorox bleach to form an Ag/AgCl coating.
10. The Ag electrode tip can be stored in bleach or washed with water and dried with clean N₂ and store in clean place until ready to use.

2.6.4 Solution preparation

Roughly 50% to 90% of the time noise and uninterpretable signals confound single molecule experiments so caution was taken to ensure the purity of solutions used in the experiments. All aqueous solutions introduced directly to the nanopore were purified to approximately 18 M Ω cm resistivity and whenever possible passed through a syringe filter passing particles no larger than 20 nm to remove particulates. Syringe filters were chosen because of their ease of setup, but required continuous manual pressure. To automate this process, syringe pumps were arranged such that filtered material drained directly into the desired storage vessel. Storage was typically done in unwashed 125 mL polypropylene reagent bottles or in 45 mL polypropylene centrifuge tubes purchased from VWR International. To prevent microscale bubbles that could cover the pore or interfere with fluid transport and to avoid possible nanoscale bubbles inside the pore, all solutions were degassed with a rough vacuum pump for 15 minutes while sonicated and then back filled with dry Ar or lab air. No repeatable difference in experimental results was noticed between degassed and non-degassed solutions or the nature of the back filled air. Although microscale bubbles can shrink in size as the gas inside dissolves into the unsaturated liquid, studies concerning

noise attributed to nanobubbles [62] within nanopores and controlled wetting and dewetting of nanopores [63] show no dependence of current noise or wetting behavior on solution degassing.

2.6.5 Wetting the nanopore and establishing a current

Wetting of the nanopore was a key step in performing translocation experiments. Unless properly treated, nanopores would exhibit no current when biased, even in the absence of macroscopically observable obstructions. Since the nanopore is stored in air, the air present in the nanopore must first be removed in order to allow fluid to enter. To facilitate this process a multi-step procedure was developed.

1. Beginning with a clean glass sample vial with ≈ 20 mL volume, pour ACS grade acetone straight from the reagent bottle. Avoid acetone that has been stored in plastic bottles or been exposed to air. It is the author's experience that older acetone absorbs and dissolves organic compounds from the air and plastic bottles over the course of months and that this leads to downstream contamination issues.
2. Place the nanopore chip directly into the acetone and gently rotate the bottle several times for 5 min.
3. While the chip is still in the bottle, taking care to keep the chip submerged, pour out most of the acetone and replace it with 5 exchanges of 100% ACS grade isopropyl alcohol. Gently rotate bottle for 5 min.
4. Pour out most isopropyl alcohol and replace with 5 exchanges of 50% ethanol. Use ACS grade ethanol filtered through a 200 nm filter.
5. Store vial for several hours to several days before use.
6. Bring the chip into the air using tweezers and mount it on the *trans* PDMS chamber, using the microscope to align the *cis* chamber. This process should be done in only a few minutes. It is thought that the nanopore will retain some liquid in or near the pore while in air for a

short time and this is what facilitates wetting later even though the pore has been exposed to air.

7. Insert fluid inlets and outlets and flush with deionized water filtered through a 20 nm pore size filter. Take care to ensure no bubbles are trapped in any portion of the apparatus, in particular near the electrodes.
8. Connect apparatus to an the Axopatch 200B and affix securely to the vibration isolated floor of a Faraday cage.
9. Apply a voltage of 100 mV to 120 mV and observe any current response. If electric current flows, measure the IV curve from -200 mV to 200 mV and measure the root-mean-square (RMS) noise at 120 mV to determine if pore resistance and noise are as expected. Refer to Chapter 3 to estimate the expected current through the pore and Chapter 4 for the expected RMS noise. The pClamp software can perform an automated IV curve, but a single current measurement at roughly 120 mV yields a good estimate of the pore resistance. The Axon 200B can measure the RMS noise over a 5 kHz bandwidth on the front panel. If these noise measurement methods are unavailable, the RMS noise can be determined by roughly $1/6^{\text{th}}$ the peak-to-peak distance of the noise at 120 mV.

If no current is measured, wetting the pore can usually be facilitated by the following measures:

- Check electrode contact with the solution: Macroscopic bubbles often gather around the electrodes. To ensure electrodes are in contact with solution, short the fluid inlet lines to each other and apply a small voltage. A measurable current will be produced depending upon the solution conductivity and system geometry. If this is not the case, it is likely that there are bubbles in the tubing that can be removed by flowing solution re-mounting the nanopore.
- Manually apply positive pressure. By pinching off the fluid outlets and applying a positive pressure up to 1 atm, conduction can occasionally be enhanced. This may be due to the change in size of unobserved bubbles on electrodes or near the nanopore.

- Wait: Sometimes pores in this apparatus spontaneously conduct after 30 minutes.
- Flush 1 M KCl: Flushing 5 mL of solution at a rate of approximately 5 mL per minute can encourage pore wetting.
- Use negative pressure: By reducing the pressure (by pulling on the syringes), bubbles inside the system become larger and can be removed much more easily by slowly flowing solution. This method can inadvertently pass macroscopic bubbles across the pore causing it to dewet and rewet, which can cause severe damage to the nanopore. Nanopores that are intentionally dewet and rewet by passing bubbles across them often immediately exhibit much higher current than is reasonable from their TEM measured geometry. This is discussed in more detail in Chapter 3.
- Add KOH: Adding KOH has been used to wet pores as a method of last resort because of its chemical etching and can open the pore much wider than measured by its TEM images. This method is also discussed in more detail in Chapter 3.

2.6.6 Adding DNA

Adding DNA is a straightforward, but extremely crucial process. The electric field of the pore is negligible more than a micrometer from the pore so if DNA containing solution is not brought within this distance, the very slow process of unbiased diffusion is the only mechanism bringing DNA to the pore. In fact, step 3 was learned after nearly six months of translocation experiments that failed, likely because DNA was not brought close enough to the pore.

1. Before opening the pore, prepare a pre-diluted experimental sample of DNA at the desired pH and salt concentration. DNA concentrations between 5 to 10 nM work well. If the DNA concentration used is too high, events come very frequently and are hard to separate. Moreover, clogging of the pore can occur soon after the experiment begins. Event rates of 3-10/sec at ≈ 100 mV work well.

2. Once a stable, low noise open pore current is established, carefully remove the waste outlet and pipette out most of the fluid from the *cis* chamber, making sure a layer of fluid remains over the nanopore at all times. Then, backfill the entire chamber with the pre-diluted sample. There is no need to mix the solution.
3. Reverse the flow of solution for a few μL such that the solution without DNA is removed and the DNA mixed solution is now directly covering the pore. This is an extremely crucial step. DNA tends to float when added to buffer solutions and mixing is difficult for very small sample volumes. By extracting the DNA-free solution and pulling the pre-mixed DNA solution directly over the pore, translocation events are *far* more likely.
4. Apply a voltage of roughly 120 mV and wait for up to a few minutes for translocations. Events should occur within 1 minute. If not, try step 3 again or add more DNA. Pores that do not translocate even after a second aliquot of DNA is added are not worth the time. Give up and try again. I mean, don't give up on science, just give up on the pore and try another. Depending on the number of years you've been working on this project, you may want to rethink working with nanopores, but if you've gotten here already, you should probably stay in science.

2.7 Biochemical protocols

Biochemistry is not a typical part of a physicist's training and any experimenter is strongly urged to seek guidance from researchers in the biochemistry field. At the University of Arkansas, collaboration with the labs of Dr. David McNabb and Dr. Ines Pinto was invaluable to learning the basics of biochemical sample preparation. Also of interest is the compendium of protocols available in the frequently updated journal *Current Protocols in Molecular Biology* [64]. The author made particular use of Chapter 2 Preparation and Analysis of DNA, Chapter 3: Enzymatic Manipulation of DNA and RNA, and Chapter 15: The Polymerase Chain Reaction.

The main thrust of five years of work was spent on a project that produced almost no results and was ultimately abandoned for more promising work. No results will be presented in this

dissertation. In brief, this project sought to hybridize three short 60 mer single stranded DNA tags along a longer 1079 nt long ssDNA molecule and use the nanopore to detect the difference between single and double stranded sections of the molecule. Significant steps were made in sample preparation for this project that will likely be of interest to future researchers and makes the bulk of the following DNA sample prep discussion.

2.7.1 Purchasing DNA

All DNA longer than 100 bases used in this work was derived from single stranded virion Φ X174 (New England Biolabs) or 7 kbp double stranded No-Limits (Thermo Scientific, formerly Fermentas). Shorter molecules were custom designed in our lab and synthesized by Eurofins MWG Operon. All DNA was purchased lyophilized and resuspended in 10 mM Tris-HCl buffer at a pH of approximately 7.5 and stored at -80° C. Ethylenediaminetetraacetic (EDTA) was also added to a total concentration of 1 mM to chelate multivalent anions that could catalyze enzymatic degradation of the DNA by trace concentrations of enzyme contamination in solution.

2.7.2 Purifying DNA

Slab-gel electrophoresis was performed on all samples received to investigate the purity and concentration of the sample and ensure the electrophoretic mobility was as reported by the supplier. All gel electrophoresis experiments were run with a 1 kbp dsDNA ladder from either New England Biolabs or Promega. All work done with the 7 kbp dsDNA required little preparation before use in nanopore experiments. The single stranded form of Φ X174 contained $\approx 80\%$ circular DNA fragments and hence had several bands representing the different conformations of DNA. Since the Φ X174 DNA was to be modified and simultaneously purified by polymerase chain reaction (PCR), the smeared bands were considered sufficient.

2.7.3 ssDNA-dsDNA hybrid molecules

The single strand form of Φ X174 DNA was purchased with several possible experiments in mind that needed that form, but the final experiment could use nearly any stretch of double stranded DNA of known sequence and length of at least 1079 kbp. Φ X174, the first DNA genome sequenced [65], contains 5386 nucleotides [66], with two restriction sites for the *DraI* enzyme separated by 1079 nt. The original intent was to produce ssDNA by annealing complimentary DNA oligomers to the *DraI* restriction sites and restrict the mostly circular Φ X174 stock to produce single stranded fragments of 4307 nt and 1079 nt followed by slab gel electrophoresis and extraction of the 1079 nt sequence. This method was costly, produced low yields, and abandoned.

A more straightforward method to produce ssDNA with any length up to about 3 knt is to use asymmetric PCR rather than restriction. This method works equally well using ssDNA and dsDNA as the starting stock and only requires that the sequence be known for two locations at least 10 nt long that are separated by the length of final molecule desired. Using the sequence of Φ X174 provided by the distributor, two 60 mer primers were designed complimentary to the Φ X174 molecule such that the 1079 nt sequence would be copied. Note that in PCR, the two primers must be complimentary to the opposing DNA strands and that the extension step by the DNA polymerase moves in the 3' direction. Hence the primers must be designed such that their 5' ends anneal to the limits of the region that is to be amplified. Sequences of oligomers used to PCR amplify the dsDNA (oligo1c, oligo3) and ssDNA (oligo1c, oligo3) as well as used to form hybrid ssDNA-dsDNA complexes (oligo1, oligo2, oligo3) are shown in Table 2.1.

Using conventional PCR reagents from Promega and their 'Taqman' Taq polymerase, conventional double stranded PCR was used to produce 1079 nt dsDNA stock that was used for translocation and to produce 1079 nt ssDNA for hybridization detection. Reagents were mixed using the concentrations shown in Table 2.2, with the Taq polymerase added just before thermocycling using the protocol shown in Table 2.3.

After PCR, sample quality was qualitatively checked using slab gel electrophoresis. Because of the exponential amplification of the desired sequence, the desired product was orders of magnitude

Name	Sequence
oligo1	5'-GATTTCTTAC CTATTAGTGG TTGAACAGCA TCGGACTCAG ATAGTAATCC ACGCTCTTTT-3'
oligo2	5'-CTTGCCTTTA GTACCTCGCA ACGGCTGCGG ACGACCAGGG CGAGCGCCAG AACGTTTTTTT-3'
oligo3	5'-TTTAAAATAG TTGTTATAGA TATTCAAATA ACCCTGAAAC AAATGCTTAG GGATTTTATT-3'
oligo1c	5'-AAAAGAGCGT GGATTACTAT CTGAGTCCGA TGCTGTTCAA CCACTAATAG GTAAGAAATC-3'

Table 2.1: Oligomers used in the fabrication of ssDNA-dsDNA hybrid molecules

Reagents	dsDNA	Asymmetric (ssDNA)
oligo1c	2 pM	4 pM
oligo3	2 pM	–
dNTPs	200 μ M	300 μ M
MgCl ₂	2.5 mM	–
Φ X174	1pM	–
dsDNA 1 kbp template	–	1 pM
Taqman Polymerase	0.05 units/ μ L	0.10 units/ μ L

Table 2.2: PCR reagents concentration. Total sample volume is 100 μ L with remaining balance of autoclaved deionized water. Promega 'Taqman' Taq polymerase is sold in supplier defined units and is available in concentrations of 5 'units'/ μ L. The dsDNA 1 kbp template is the amplified product of the dsDNA PCR protocol. An experimenter using this recipe is encouraged to modify the concentrations represented here to optimize the protocol for their purposes.

more concentrated than the original Φ X174 genome, and was clearly visible on a gel at dilutions that made the virion Φ X174 undetectable. The PCR reagents were further purified by manually excising the 1079 bp band and removed using a silica membrane based spin column gel extraction kit purchased from Qiagen (QIAquick Gel Extraction Kit). The DNA was eluted using 10 mM Tris 1 mM EDTA. This purification step acted to remove undesired DNA from the Φ X174 and to remove the short primers and reagents that would complicate the production of ssDNA later. After this step, approximately 1 μ L (\approx 50 ng) was run on slab-gel electrophoresis to verify the purity and presence of the sample and a UV-Vis absorbance at 260 nm wavelength was measured to quantify the concentration of the DNA. Final concentrations were between 50 nM and 150 nM. The eluted DNA was stored at -80°C or used immediately as the stock for ssDNA amplification.

Step	Duration		Temperature	Notes
	dsDNA	ssDNA		
1.	2 min	30 sec	95° C	Initial denaturation
2.	1 min	1 min	95° C	Denaturation
3.	1 min	1 min	55° C	Annealing
4.	1.5 min	1 min	72° C	Extension
5.				GOTO STEP 2. 29 TIMES for dsDNA 39 TIMES for ssDNA
6.	5 min	5 min	72°C	Final extension
7.	Inf.	Inf.	5°C	Hold until retrieved

Table 2.3: PCR thermocycler protocol. An experimenter using this recipe is encouraged to optimize this protocol for her or his purposes.

Finally, ssDNA was produced using asymmetric PCR using the purified dsDNA stock and adding only one primer, oligo1c as shown in table 2.2. The thermocycler protocol was nearly identical to that used for dsDNA, as shown in Table 2.3. After PCR, this DNA was qualitatively checked for purity and concentration by running a gel electrophoresis the same as was done after the dsDNA PCR. Oligos oligo1, oligo2, and oligo3 were then added to the ssDNA in equimolar ratios for a total volume of 30 μ L in a 1.5 mL max volume polypropylene Eppendorf style tube and then suspended in a 1 L bath of boiling water for 5 min and allowed to cool for 2 hr. This extreme temperature treatment was warranted since the oligomers had melting temperatures approaching 90° C as predicted by sequence dependent salt adjusted calculation using the OligoCalc software [67]. The final samples were stored until use for later nanopore experiments at -80° C.

Chapter 3

Nanopore conductance, conductance drop, and stability in salt solutions

3.1 Introduction

As introduced in Chapter 1, research over the last decade has shown the single molecule sensitivity of solid state nanopores to the study of DNA [11], ssDNA[68], RNA [69], and proteins [70]. The sub-molecular sensitivity of solid state as well as their biological counterparts have inspired investigation into their use in single molecule high throughput DNA sequencing with recent success in detecting sequence dependent information within DNA molecules [37, 71, 72]. Genetically engineered variants of natural transmembrane pores have the highest sensitivity to date [37, 71], but the tunable size and shape of solid state nanopores and their easily scalable integration with wafer scale electronics fabrication make solid state nanopores more appealing. Typical solid state nanopores are fabricated through either direct drilling by a TEM-based electron beam [18, 19], or use a combination of drilling and closing a larger hole as in ion-beam sculpting (IBS) [11], atomic layer deposition [73, 74], and thermal annealing [50, 75]. Materials used to fabricate nanopores include SiO_2 [18], SiN_x [11], Al_2O_3 [73, 74], and suspended graphene [40, 38, 39]. Hybrid biological solid state nanopores include combining transmembrane pores [76], DNA origami pores [77] or lipid bilayers with solid state substrates [78].

Although advances in fabrication have improved the dimensions of solid state nanopores for their use in single molecule experiments, less work has been done to ensure pores remain at those dimensions in ionic solutions. Increase in conductance during experiment has been attributed to changes in pore radius [50, 79], but the 3D structure of pores once wet or mechanism of radius change has not been investigated to the author's knowledge. In this chapter we show, through a combination of TEM methods, translocation experiments, and numerical modeling, that pore radius increases while keeping the pore thickness profile nearly unchanged. Furthermore, we show that chemical dissolution is the likely mechanism of this geometry change and that changes in

fabrication procedure can significantly reduce the rate of change.

3.2 Methods

3.2.1 Nanopore fabrication

To determine the applicability of our method over a wide range of pore dimensions, nanopores were fabricated using either IBS or TEM drilling with diameters between 4 nm to 45 nm with a median diameter of 12 nm. Details of the IBS method [80] and TEM method [19] are documented in Chapter 1. Briefly, in the IBS method we first use a 50 keV Ga⁺ focused ion beam (FIB) to mill a single ≈ 100 nm diameter hole in a ≈ 250 nm thick freestanding low tensile stress, silicon rich LPCVD deposited SiN_x membrane suspended on a 3 mm x 3 mm silicon chip deposited with dichlorosilane and NH₃ at 800° C. This chip is mounted in a custom made vacuum system [14] where a 3 keV Ne⁺ ion beam was directed normal to the SiN_x surface with a typical flux of 1 ion/nm² sec. Ions that passed through the hole were focused by an electrostatic lens system on a ‘channeltron’ style single ion detector connected to a LabView controlled single ion counting system. The ion beam impinging upon the pore elicits lateral mass flow that shrinks the top of the hole. As the hole shrinks, the ion beam current through the hole decreases. By measuring the beginning hole area with TEM and assuming that the pore area is proportional to the ion beam current, the beam was deflected using a LabView controlled feedback system when the desired area was reached. To determine if a decrease in dangling bonds left over from the IBS process can improve the stability of IBS pores, we annealed half of the IBS samples at 800° C for 1 hr in dry N₂ in a tube furnace with a flow rate that ensured hundreds of volume exchanges over that time.

In TEM drilling, we begin with the same freestanding SiN_x membrane and FIB milled a ≈ 200 nm deep 100 nm diameter pit in the same 250nm thick SiN_x freestanding membrane and drill a nanopore with a 300 keV electron beam of an FEI-Titan TEM in imaging mode focused to spot with full width at half maximum of ≈ 3 nm. This beam size was used to reduce beam induced damage that is known to decrease pore stability [50]. The beam was manually directed to the edge of the pore to widen the pore to the desired size.

3.2.2 TEM geometry characterization

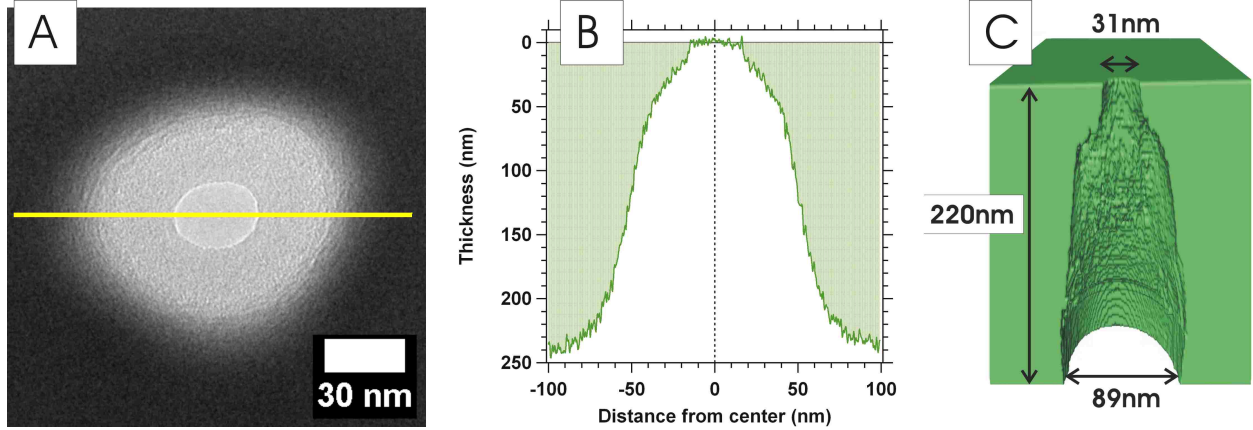


Figure 3.1: Geometry of ion-beam sculpted (IBS) nanopores. (A) Plan view TEM image of IBS nanopore. (B) Thickness map along solid line shown in TEM image (C) 3D tomogram reconstruction of the same pore.

Analysis of all nanopores was done using either an FEI-Titan TEM at 300 keV or an FEI-Tecni TEM at 200 keV equipped with Gatan post column electron energy loss filters. Since the contrast of bright field TEM images are difficult to interpret quantitatively, they were used only to determine the radius of the nanopore and vestibule. Energy filtered TEM (EFTEM) at either 300 keV or 200 keV was used to produce thickness maps of nanopores by taking two images, the first with a 10 eV energy slit centered at the zero loss peak, $I_{zlp}(x,y)$ and another, unfiltered image $I_0(x,y)$ and thickness calculated using the log-ratio method,

$$t(x,y) = \lambda \ln \left(\frac{I_0(x,y)}{I_{zlp}(x,y)} \right). \quad (3.1)$$

These images were aligned using cross correlation to compensate for sample drift using Digital Micrograph (Gatan) [81]. The inelastic mean free path λ was found for both energies for our material by measuring the thickness of several membranes by thin film reflectometry. Mean free paths of $\lambda = 185$ nm at 300 keV and $\lambda = 152$ nm 200 keV were found using this method. These values were repeatable from sample to sample within a few nm, well within the 10% error commonly used in measuring very thin structures [81]. A non-zero log ratio baseline at the center of the nanopore also seen by other researchers [50] was removed by deconvolution using a point spread function

estimated from the EFTEM thickness measurement of FIB milled sharp step edges in membranes of identical thickness and composition as those used to make nanopores.

To construct our tomograms, bright field images were zero loss filtered with a filter width of 10 eV at an acceleration of 200 keV on an FEI-Tecnai TEM. Images were taken in 1° increments over $\pm 35^\circ$. Image alignment was done using low pass filtering and cross correlation and tomograms were reconstructed using weighted back projection in Inspect3D Xpress (FEI Company). Segmentation was done with Amira 5 (Visualization Sciences Group) using semi-automated thresholding with manual guidance.

The thickness of the pore was measured using the radial profile plugin in ImageJ [82] by first integrating along the azimuthal angles about the pore center and extracting the thickness of the point farthest from the center of the pore as determined from bright field images. The cone angle was calculated in IGOR Pro (Wavemetrics) from a least squares linear fit to the cone region from the radial thickness map.

3.2.3 Conductance and conductance drop measurement

Nanopores were mounted as the sole fluidic and electronic connection between two $\approx 80 \mu\text{L}$ chambers containing a solution of 1 M KCl, 10 mM Tris, and 1 mM EDTA at pH 7.5. The chambers were constructed of custom fabricated disposable polydimethylsiloxane (PDMS) as detailed elsewhere [80, 52]. The entire system was mounted on a vibration isolated Faraday cage (TMC). Voltage was applied using Ag/AgCl electrodes and currents measured using an Axopatch 200B and Digi-data 1322A (Molecular Devices). The dsDNA added for all translocations was 7 kbp (Thermo Scientific, NoLimits). Current was measured using pClamp 9 (Molecular Devices), and files were post-processed using custom software written in MATLAB (Mathworks). Pores were wet by first immersing for several hours to overnight in 50% ethanol, followed by mounting in the PDMS cell and flushing with DI water and then 1 M KCl. Typically, current was not present through pores immediately and positive and negative pressure had to be applied manually by syringe with current typically appearing in less than 30 min. Once conducting, IV curves were taken several times

during an experiment to ensure linearity. Open pore conductance was determined from baseline current without DNA events divided by the applied voltage, usually 120 mV. Electrochemical drift due to the electrodes was compensated for several times an hour by first measuring current at zero applied bias and then applying a small offset voltage of a few millivolts to zero the current. This offset bias was considered zero applied bias for subsequent conductance measurements. Currents without offset bias were never more than several hundred pA. To find conductance drops, tens of thousands of events were recorded at multiple voltages ranging between 60 mV and 360 mV, resulting in thousands to many tens of thousands of translocation events per pore. Mean current drops of unfolded translocations were plotted vs voltage and fitted using least squares regression in IGOR with the slope of fit used to find the conductance drop. Almost all current drop vs voltage curves were clearly linear. Pores in which current drop vs voltage was not linear were not considered in current drop analysis and consisted of less than about 10% of the pores studied. Conductance drop errors are from the error to the least squares fit with the assumption that residuals were normally distributed.

3.3 Results and Discussion

3.3.1 Conductance increased with simultaneous decrease in conductance drop

We observed gradual conductance increases in most pores before the addition of DNA. In pores that had already increased in conductance significantly before the addition of DNA, we observed conductance drops that were smaller than those from similarly fabricated pores that had not increased in conductance. Because DNA can permanently clog the nanopore, observing a decrease in conductance drop as open pore conductance increased within the same pore was difficult. To observe this phenomena in the same pore we used a combination of KOH etching and dewetting to intentionally increase conductance and perform translocations in several stages as shown in Figure 3.2. The observed increase in conductance and decrease in conductance drop is consistent with a change in geometry that widens the pore.

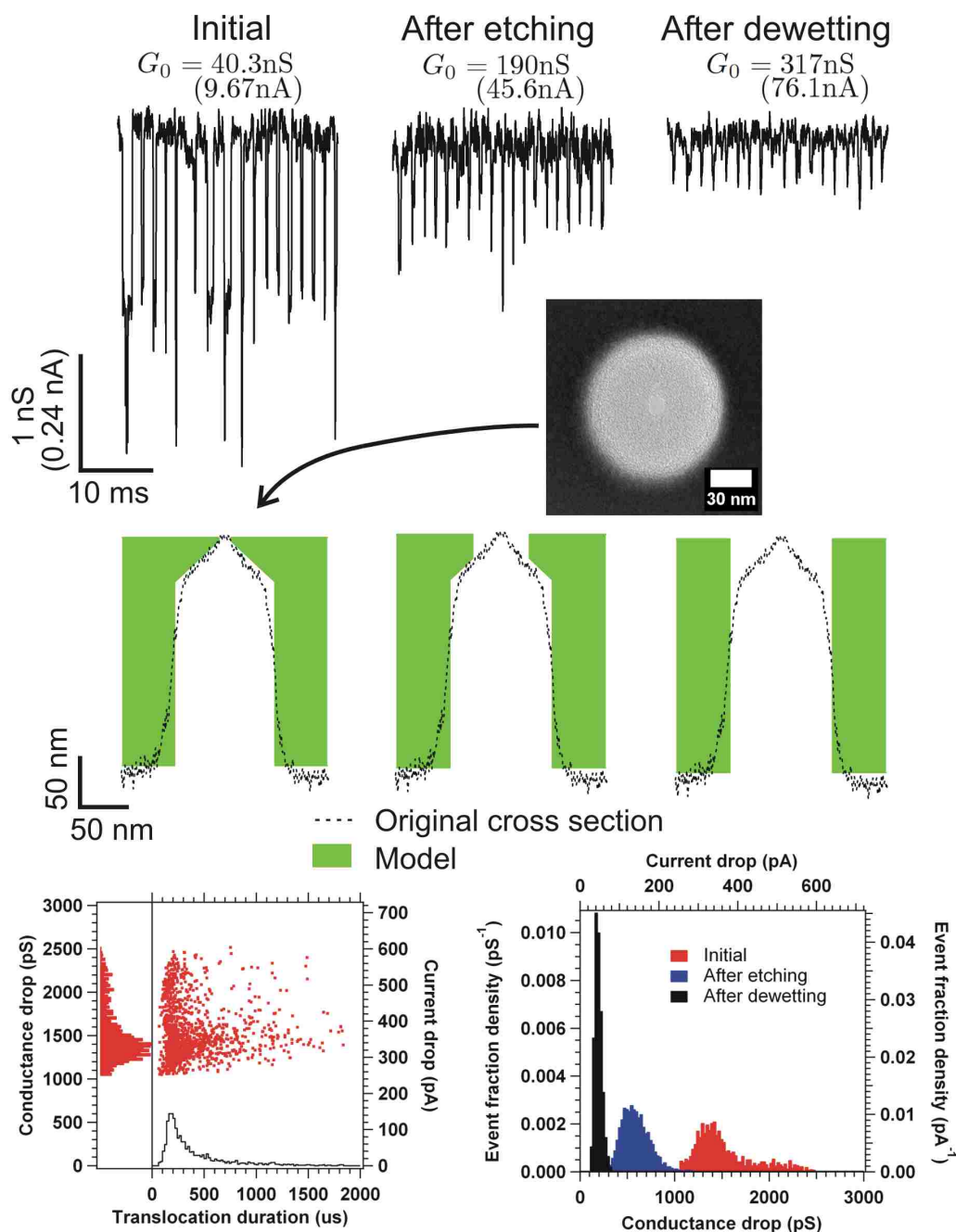


Figure 3.2: (Top) Concatenated conductance drops for (Initial) DNA events just after wetting pore after etching and after dewetting and rewetting. (Middle) Measured TEM cross section and model geometries for the initial, etching, and dewetting stages of the same pore as shown in (Top). (Bottom left) Scatterplot showing conductance drop and translocation time for all events for the same pore as above before etching. (Bottom right) Normalized conductance drop histograms for all events from the same pore for the three stages shown above. The applied voltage for all stages was 240 mV.

3.3.2 Nanopores etch laterally during experiment

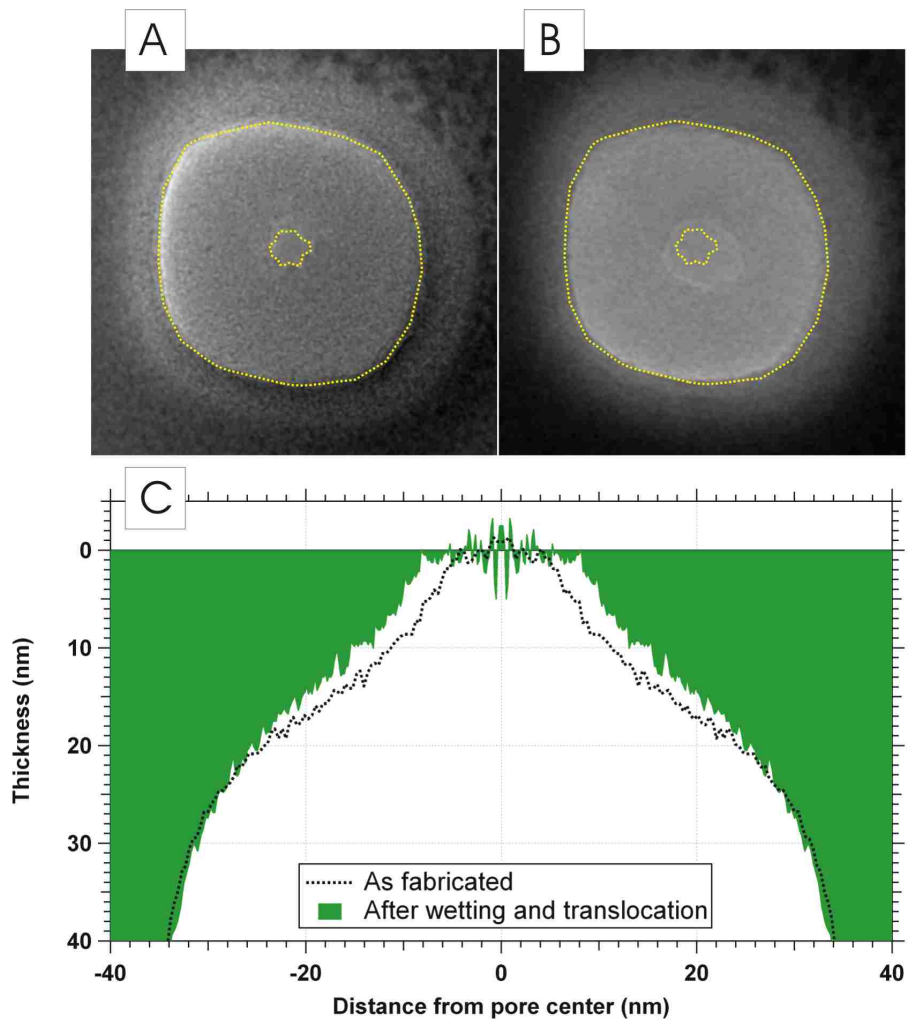


Figure 3.3: (A) Bright field TEM image of a nanopore as fabricated in vacuum and (B) after wetting and translocation. Dotted line shows outline of pore and vestibule before wetting. (C) EFTEM derived thickness profile before and after wetting. To aid in comparison, thickness profiles were radially averaged then mirrored about the center point. Noise at the center of the pore is an artifact of the averaging process.

To determine the precise changes in nanopore structure that were occurring, we used EFTEM to map the thickness of all pores used in this study. This allowed us to compare their precise geometry with the measured conductance and conductance drop. EFTEM thickness mapping takes only a few minutes and is fast enough for routine measurement, but does not provide the location of the material along the pore axis. Each position in the x-y plane in the map can be viewed as a column of material of known thickness that could be moved arbitrarily along the z-axis. In order to find the

location of the center of mass along the z-axis for each pixel, we used TEM tomography [83, 84] to find the ≈ 10 nm low resolution full 3D reconstructions for several samples fabricated by IBS as shown in Figure 3.1C.

Because of the very thick supporting membrane, the thinnest region of the nanopore was obfuscated at tilt angles greater than $\pm 35^\circ$, degrading the resolution of our reconstruction. The tomographic reconstruction of a point in space can roughly be approximated as a 3D ellipsoid with the longest axis, and hence lowest resolution, along the electron beam path [85]. Every point in the reconstructed nanopore becomes an ellipse centered at the original point but spread approximately 5 nm above and below the actual position along the z-axis. The x-y plane has a resolution much closer to that shown in the plan-view image in Figure 3.1A. We conclude that the 3D geometry as shown in Figure 3.1C is similar to the geometry inferred by the EFTEM thickness map when plotted as in Figure 3.1B, allowing us to approximate our the 3D geometry of the nanopore directly from the EFTEM thickness map. We were unable to resolve the rounded edge of the pore as shown by destructive cross sectional imaging done recently by Kuan [42]. It is likely that these structures will be important in the conductance modeling for nanopores smaller than those used in this work.

This reconstruction confirmed earlier work [12, 42] that show IBS pores have a lateral mass flow at the top surface that produced a single truncated cone at the resolution measured. We note that material in an IBS pore flows at a depth greater than the roughly 5 nm mean penetration depth of the ion [12]. The conical thickness profile creating the transition between nanopore and the larger vestibule is similar to that hypothesized by Cai [12] but is unlike the stressed overhang predicted by George [17]. These results will be of importance to future modeling of lateral mass flow caused by IBS and are under further investigation.

Because our TEM fabricated pores were fabricated from pits of dimensions similar to the holes used to fabricate our IBS pore, they had similar structures at this resolution but consistently larger cone angles. We expect that the region immediately adjacent to TEM fabricated pores has the well characterized truncated double-cone geometry as shown in earlier work [19], but because of the low resolution tomographic reconstruction were unable to resolve the structure.

As shown in Figure 3.3, after wetting, most mass loss occurred in IBS pores at the newly formed material of the pore and cone. Most mass loss occurred at the thinnest region of the pore, changing the radius of the pore while keeping the cone angle nearly the same. The vestibule and membrane far from the pore showed little to no change after wetting.

3.3.3 Modeling to determine radius change from conductance and conductance drop

For the 1 M KCl salt concentrations used in this study, the Debye length is $\approx 0.3\text{nm}$, far less than the dimensions of the features of our nanopores, making the Ohmic approximation to conductance reasonable [86, 87, 88]. To approximate the non-cylindrical geometry of the entire structure, we approximate the resistance of our system as the sum of five resistors in series. To find the resistance between the nanopore mouth and the bulk $R_{a,n}$ and the resistance between the vestibule and the bulk on the opposing side $R_{a,v}$ we use the same model as Hall [89]. To find the resistance of the nanopore cylinder R_p , cone region R_c , and vestibule cylinder R_v we approximate the conductance of each separate region using

$$G_0 = \sigma \left(\int \frac{dz}{A(z)} \right)^{-1} \quad (3.2)$$

where σ is the measured bulk solution conductivity and $A(z)$ is the cross sectional area at point z along the pore axis. This approximation is only exact for cylinders with field lines parallel to the pore walls but is within 10-20% of the numerically calculated value for a conical resistor with dimensions similar to ours [90]. Our total pore conductance can thus be written as

$$G_0(r_p) = (R_{a,p} + R_p + R_c + R_v + R_{a,v})^{-1} \quad (3.3)$$

$$= \sigma \left(\frac{1}{4r_p} + \frac{t_p}{\pi r_p^2} + \frac{t_c}{\pi r_p r_v} + \frac{t_v}{\pi r_v^2} + \frac{1}{4r_v} \right)^{-1} \quad (3.4)$$

where t_p , t_c , and t_v are the respective thicknesses of the pore, cone, and vestibule, and r_p and r_v are the respective radii of the pore and vestibule. We mathematically model our simplification that etching occurs at only the thinnest region by assuming that t_p increases at the same time r_p increases such that the cone angle is kept the same as shown in Figure 3.4A. This assumption

allows us to model the change in pore thickness Δt_p and cone thickness Δt_c as

$$\Delta t_p = -\Delta t_c = \frac{\Delta r_p}{\tan(\theta)} \quad (3.5)$$

and results in r_p as the sole free parameter to compare our measured conductance with the TEM measured geometry. Theoretically predicted conductances and conductance drops vs radius are diagrammed in Figure 3.4 B.

Single DNA molecules longer than about 1 kbp translocating through the pore produce changes in conductance nearly proportional to the cross section of the molecule [10, 25] in a manner that depends upon pore radius and the relative contribution of the pore and access resistance [91]. Using the Kowalczyk modified Hall access resistance [91] for a long molecule entering a pore and performing the integral in Equation 3.2 while taking into account the blocking DNA molecule, the conductance while the pore is blocked becomes

$$G_b(r_p) = \sigma \left[\frac{1}{4r_{pe}} + \frac{t_p}{\pi r_{pe}^2} + \frac{t_c}{2\pi(r_v - r_p)r_d} \ln \left(\frac{(r_v - r_d)(r_p + r_d)}{(r_v + r_d)(r_p - r_d)} \right) + \frac{t_v}{\pi r_{ve}^2} + \frac{1}{4r_{ve}} \right]^{-1} \quad (3.6)$$

where $r_{pe} = \sqrt{r_p^2 - r_d^2}$ and $r_{ve} = \sqrt{r_v^2 - r_d^2}$ are the effective radius of a cylinder with the same cross sectional area as the cylinder minus the DNA molecule for the nanopore and vestibule respectively. The third, longer term represents the cone region resistance during the presence of DNA calculated using Equation 3.2. Finally, the conductance blockage is calculated as

$$\Delta G = G_0 - G_b \quad (3.7)$$

We note that in the limit of r_p approaching r_v , Equations 3.4 and 3.7 simplify to equations modeling the nanopore of a single cylinder used in the literature [92, 91]. We also note that this modeling

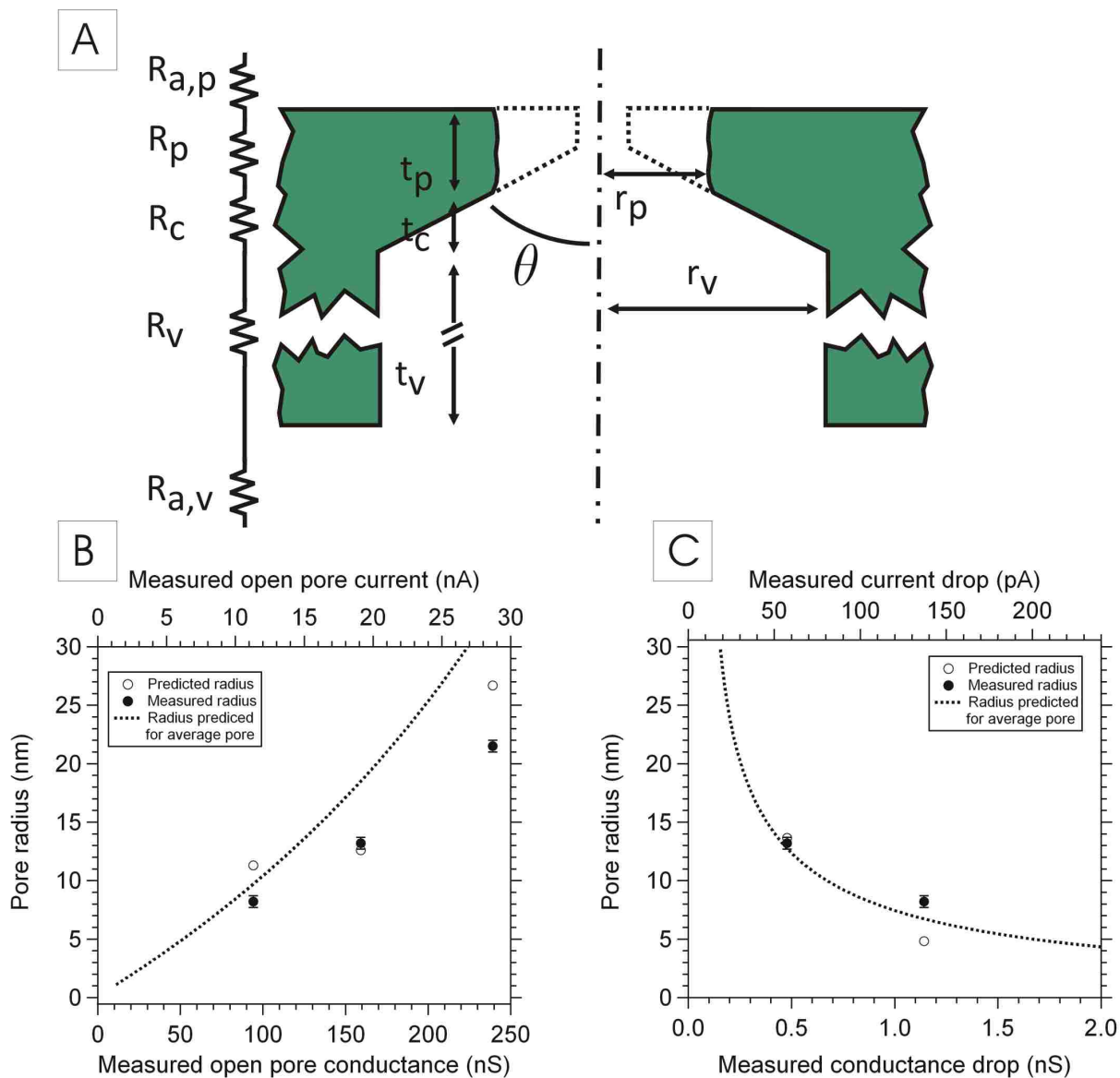


Figure 3.4: (A) Idealized cylinder-cone-cylinder geometry of nanopores showing idealized mass loss model. (B) (open circles) Pore radius fit using Equation 3.4 from the measured conductance and initial pore geometry. (closed circles) Pore radius measured by TEM after wetting. (C) (open circles) Pore radius fit using Equation 3.7 from the measured conductance drop and initial pore geometry. (closed circles) Pore radius measured by TEM after wetting. Conductances measured at 120 mV.

method can easily be modified to include variations in molecule cross section, but this variation is omitted in our model here since these variations were undetectable with the pores used in this study.

3.3.4 Radius change rate determined from conductance and conductance drop is similar

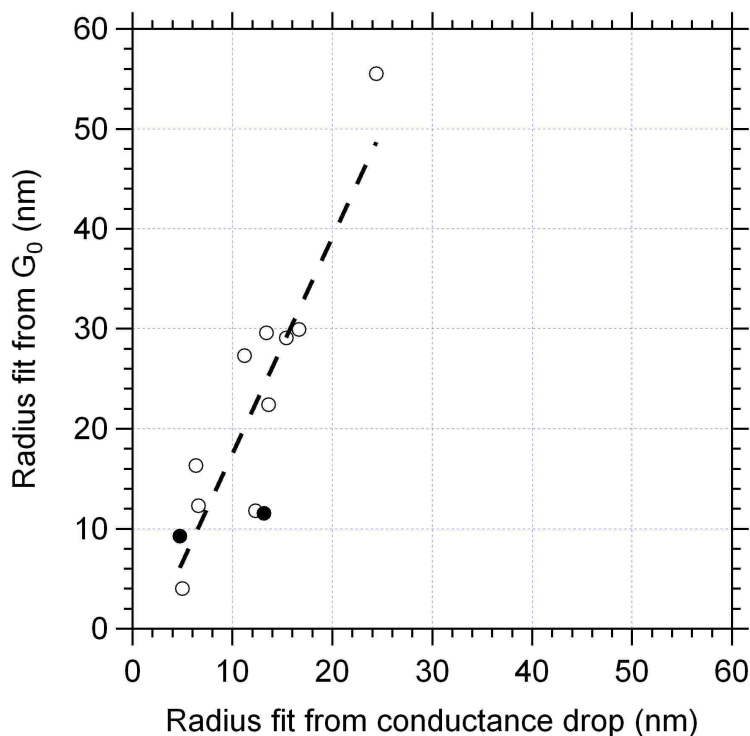


Figure 3.5: Graph showing difference in pore radius predicted by pore conductance and conductance drop. Perfect agreement between the two methods would produce a line at 45° . Dashed line is a linear fit to the data. Solid dots denote pores with post wetting TEM images in Figure 3.4B

Both Equation 3.4 and 3.7 were solved numerically to provide independent estimates of r_p at the moment that translocations were measured. Although on average our pores had conductances slightly higher than predicted from TEM images once wet, several pores had conductances lower than expected from our model. For these, we fit the radius as smaller than measured from TEM images. It is possible that this is due to errors in our measurement of pore geometry and our modeling, but we cannot rule out the possibility of a partial wetting of the pore. Exact agreement between the estimated change in radius from Equation 3.4 and Equation 3.7 would result in a fit line with a slope of 1 in Figure 3.5, but our slope is 1.9 ± 0.2 . Since the change in radius predicted by the open pore conductance and Equation (3.4) agrees well with post-wet TEM images, we interpret this result as a systematic under-prediction of the conductance drop magnitude by our model. Since the conductance drop is most sensitive to the pore geometry at the narrowest constriction, this may

be evidence that our method does not sufficiently model this region at high enough resolution, however, we cannot rule out other effects due to our ohmic simplification and the approximate method for calculating the conductance made by Equation (3.2).

3.3.5 Radius change rate

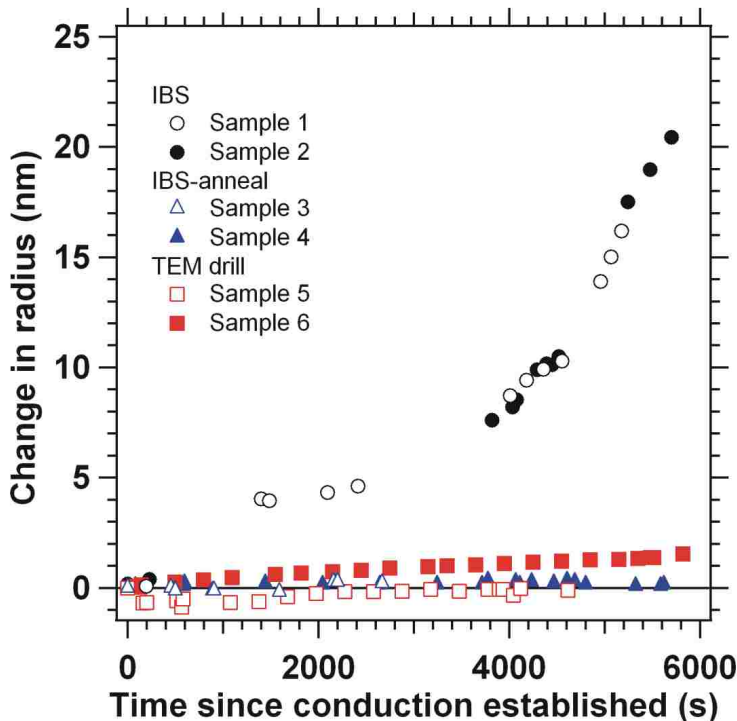


Figure 3.6: Increase in pore radius vs time calculated using Equation (3.4) for all fabrication methods tested.

Fabrication method	Etch rate
IBS	$10 \pm 6.5 \text{ nm/hr}$
IBS-annealed	$0.22 \pm 0.4 \text{ nm/hr}$
TEM drilled	$1.0 \pm 1.2 \text{ nm/hr}$

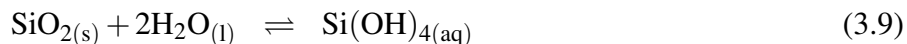
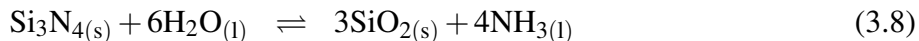
Table 3.1: Etch rate for all fabrication methods tested. Errors are standard deviations. Three samples were measured for each fabrication method.

After opening and stabilizing, we observed the rise in open pore conductance vs time and using Equation (3.4), estimated the rate at which the radius changed. Example opening traces from 6 samples are shown in Figure 3.6. The rate of conductance change decreased over the roughly

1 hr time during which conductance was measured, but due to the geometry of the pore, radius change etch rates were predominately linear during the time conductance was observed. Several pores showed initial conductances as if $r_p = r_v$ and were interpreted as the cone region of the pore failing catastrophically upon wetting and were omitted from our analysis. As shown in Table 3.1, annealing IBS nanopores significantly decreased their etch rate and made them comparable to TEM drilled pores.

3.3.6 Chemical etching mechanism and comparison of pore etching with the bulk etch rate

In the semiconductor manufacturing industry, SiN_x is typically etched with aggressive etchants such as phosphoric acid, potassium hydroxide, and hydrofluoric acid [93]. Because of the long-term stability of microelectronics in less aggressive environments such as implants or environmental sensors is of great concern for micro-electro-mechanical systems (MEMS) [94], the dissolution of SiN_x in deionized water [95, 94, 96, 97, 98] and salt solutions [99, 100] has also been studied. The chemical reaction of stoichiometric Si_3N_4 with water can be summarized as [97, 96]



In reaction 3.9 the Si-N bond is hydrolysed by water to produce SiO_2 and ammonia. The SiO_2 further hydrolyses to form silicic acid which diffuses away into the solution, exposing the next layer. Extra silicon in our silicon rich nitride hydrolyzes and to form SiO_2 , which dissolves as in reaction 3.9. In thin films, this reaction has been shown to follow an Arrhenius type relationship with temperature with rates that depend upon the fabrication method, solution pH, and salt concentration. For neutral pH, etch rates range from 0.01 to 0.1 nm/hr with the highly coordinated crystalline SiN_x [98] powders and LPCVD thin films [99, 94] having the slowest etch rates and the less coordinated PECVD thin films having the highest. Salt concentrations such as that found in living organisms [99] and 1 M NaCl [100] were shown to increase these rates by up to an order of magnitude.

To compare the etch rates of SiN_x measured using nanopores with those from bulk thin films, we must first consider any affects of the confined geometry and the contribution of surface energy at the nanoscale radii of curvature. Research in nanoporous SiN_x aggregates show that the dissolution reaction is slow enough to be reaction limited rather than diffusion limited [98], and that the products of dissolution diffuse out of the nanopores fast enough for us to assume that the pore solution is the same as the bath solution. Therefore, the dissolved species are far from equilibrium with the still bound atoms and we can neglect their influence [101]. Research on SiO_2 nanoparticles show very little change in dissolution rate with radius and suggest that radii greater than 0.6 nm have etch rates that can be predicted by bulk equations alone. Recent work with very high electric fields in nanopores [79] suggest a etching effects due to electric fields require fields at almost two orders of magnitude greater than those used in this work. We thus conclude that the rate of change in radius is directly comparable to the bulk etch rate.

It has been shown that annealing silicon oxynitride films decreases dangling bonds and increases Si-N coordination [102] and has been shown to reduce the etch rate of LPCVD nitrides in DI water [94] and aggressive wet etchants [103], the significant reduction in etch rate in annealed IBS samples is consistent with a reduction in dangling bonds and reduced sensitivity to hydrolytic attack. We thus conclude that the reason for the increase in dissolution rate for our nanopores over other nitrides in similar salt solutions is due to the presence of dangling bonds that are left over from the IBS fabrication process. This conclusion is further supported by the fact that annealing IBS pores brings their etch rate comparable to that of TEM fabricated pores, possibly making the material more like the deposited LPCVD SiN_x .

3.4 Conclusion

We used the full 3D geometry of nanopores to show that the simultaneous increase in open pore conductance and decrease in single molecule conductance drop are caused predominately by a lateral change in radius, even in complicated non-cylindrical nanopores. Using a model based on this geometry, we measure pore stability and were successful in developing more robust nanopores.

This work provides a method that can routinely determine the thickness profile of nanopores to improve predictions of pore current and conductance drop. These methods will be of use in monitoring and improving nanopore reliability as improvements are made in their sensitivity and is applicable to solid state pores fabricated of any material.

Chapter 4

Noise in ionic current through IBS nanopores

It is probably fair comment to say that to many physicists the subject of fluctuations (or ‘noise’ to put it bluntly) appears rather esoteric and perhaps even pointless; spontaneous fluctuations seem nothing but an unwanted evil which only an unwise experimenter would encounter!

Quote from the preface of MacDonald’s 1962 introductory monograph ‘Noise and Fluctuations’ [104], also beginning Dutta and Horn’s 1981 review article [105]

There is no noise, only sound.

John Cage, American composer 1912-1992

4.1 When noise *is* signal

The noise—or more appropriately, statistical fluctuations—measured in nanopore experiments without any added molecules has highly repeatable, theoretically fundamental properties that exist in any measurement of ions flowing through solution. Many of these fundamental noise sources are shared with the measurement of current through any resistive and capacitive system no matter the nature of the charge carrier, but there are also noise properties that vary between pore to pore and are ill understood.

These properties are separate from the ‘noise’ that is usually brought to mind when an experimental scientist refers to noise: interference due to the experimental setup. In this chapter we discuss the known fundamental noise processes in nanopore measurements and the experimental setup and separate them from the less understood noise sources of the nanopore in order to better understand and attempt to improve pore-to-pore repeatability with respect to noise sources. We show that the so called $1/f$ or ‘flicker’ noise dominates pore-to-pore noise variability.

Data similar to that shown in Figure 4.1 hypothesize that noble gas and annealing steps used to fabricate IBS nanopores can be used to modify the ‘ $1/f$ ’ noise in nanopores. Using X-ray photoelectron spectroscopy (XPS) and atomic force microscopy (AFM) we characterize changes in surface chemistry and topography of the material near the pore as a function of fabrication method in an attempt to correlate these changes with noise properties of the nanopore. We conclude by being unable to confirm our hypothesis and were unable to find a strong correlation between fabrication procedure and nanopore noise.

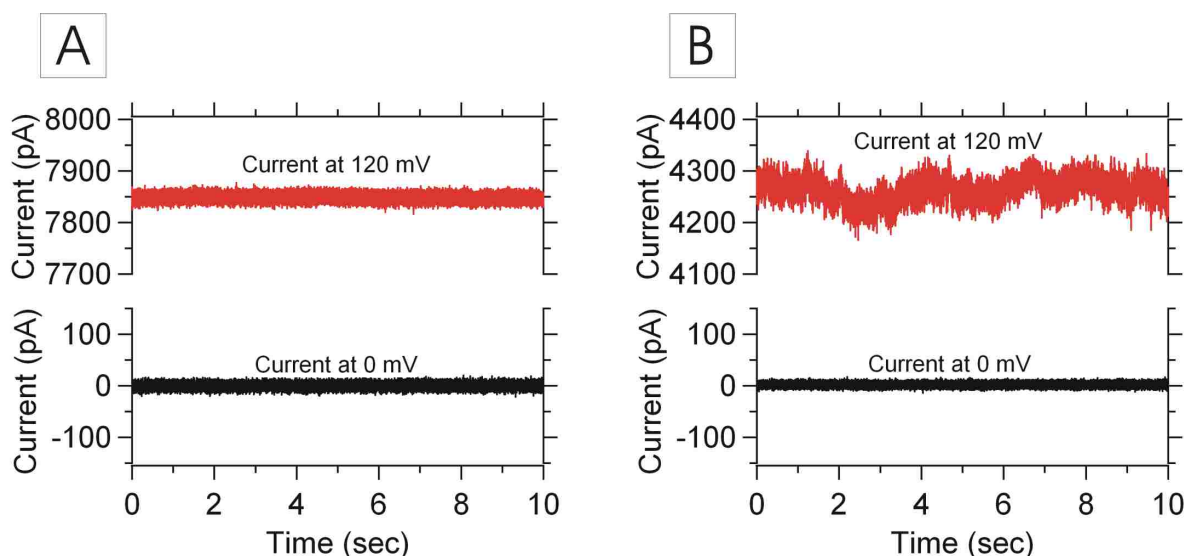


Figure 4.1: A) Current measured through a ‘quiet’ nanopore at zero applied voltage and at 120 mV. Nanopore 19 nm diameter, 1M KCl pH 7.5, Tris-EDTA buffer. Digital 10 kHz lowpass filter. B) Current measured through a ‘noisy’ nanopore at zero applied voltage and at 120 mV. Nanopore 10 nm diameter, 1M KCl pH 7.5, Tris-EDTA buffer. Digital 10 kHz lowpass filter. Both pores shown here were fabricated with neon.

4.2 Introduction to noise measurement

4.2.1 Spectral density estimation

In order to characterize the noise in our system we start with a few assumptions, namely that the noise in our nanopore is stationary and ergodic. Roughly speaking, stating that a system is stationary is equivalent to stating that properties such as mean and variance do not change in time. It is assumed, for example, that the current through a nanopore at a constant bias is not perturbed

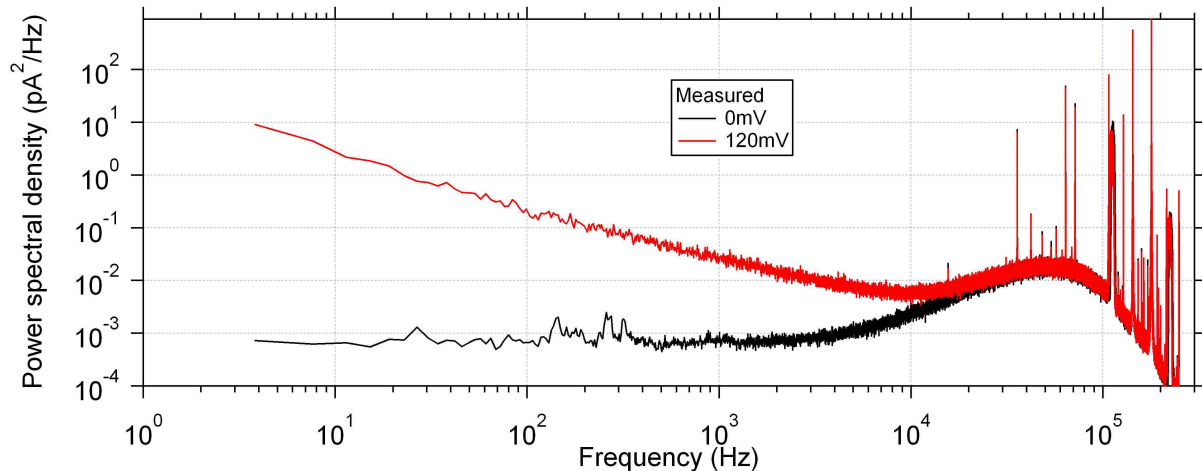


Figure 4.2: Power spectral density of current fluctuations through ‘noisy’ nanopore shown in Figure 4.1B

in a time varying way such as by a translocating DNA molecule or external electromagnetic noise and that the data is taken over a time period very short compared to slowly moving variables such as the rate at which the pore etches. The assumption that our system is ergodic, namely that conclusions made from time averaging of current are identical to ensemble averaging over many identically prepared nanopores. This allows us to conclude statistical information such as the mean and variance of current by time averaging rather than ensemble averaging over multiple experiments.

One of the most powerful methods to study noise is by examining its power spectral density (PSD), which can roughly be described as the magnitude of a signal’s Fourier spectrum. The precise definition of the PSD is often approached using a limiting procedure that assumes a signal is measured over all time, or as the Fourier transform of the related autocorrelation of the signal. Although this derivation is fascinating on its own and definitely required reading for those interested in stochastic processes, the fact that all signals are recorded over a finite time period means that the PSD can only be *estimated*. The reader seeking further understanding the theoretical foundations of the PSD is directed to the excellent introductory text by Reif Chapter 15 [106] as well as Hayes Section 3.3 [107], and Madisetti Chapter 14 [108].

We now define the estimation of the PSD, referred to as the periodogram, that we use in this

work to estimate the PSD and will refer to the periodogram and PSD interchangeably. First, we define our signal as the measurements $x(t_n)$ where t_n denotes the discrete time intervals $n = 0, 1, 2, \dots, N - 1$, each separated by time Δt over which the sample is measured. Since N is finite, we thus have data measured over the total time interval T where $T = N\Delta t$. We calculate the discrete time Fourier transform of our signal as

$$X^T(f_k) = \sum_{n=0}^{N-1} x(t_n) e^{-i2\pi f_k n \Delta t} \Delta t. \quad (4.1)$$

The superscript T is added as a reminder that this Fourier transform is over a finite time interval and the subscript $k = 0, 1, 2, \dots, N - 1$ acts similar to the subscript n as it denotes discrete samples in frequency space starting at zero frequency and separated by $\Delta f = 1/T$. Using the symbol S for our periodogram, we define it as

$$S_x(f_k) = \frac{2}{T} |X^T(f_k)|^2. \quad (4.2)$$

The subscript x is used as a reminder of what time-space function the PSD refers to. The coefficient $2/T$ is multiplied by the magnitude of our Fourier spectrum so that the total power of the signal is a constant value as $T \rightarrow \infty$. This definition has several useful qualities used in this work. In particular, the root-mean-square noise can be calculated as

$$x_{rms} = \sqrt{\int_{f_l}^{f_h} S_x df} \quad (4.3)$$

where f_l and f_h define the bandwidth over which the rms value is calculated. Estimating the PSD from the periodogram contains errors that are discussed in the references given above and improving the estimation can be done by a number of means. In this work we use the Bartlett method to improve our spectral estimation where we divide the dataset $x(t_n)$ into adjacent segments of length m , calculate the periodogram for each segment and then average them together. In this work our noise traces long enough such that approximately 10 spectral estimates are averaged

together.

4.3 Noise in all systems

4.3.1 Thermal noise

Charge carriers above absolute zero undergo thermal fluctuations usually referred to as thermal noise or Johnson-Nyquist noise after the experimentalist and theorist that simultaneously published a demonstration of the effect and theoretical explanation in 1928 [109, 110]. Within the limits of the equipment of the time, Johnson discovered that for any resistor (including tubes of KCl solution he studied in his original paper) the mean-squared voltage, and similarly current noise, was proportional to the temperature of the resistor and magnitude of its resistance given by

$$S_{I,therm} = \frac{4k_bT}{R} \quad (4.4)$$

$$I_{rms,therm} = \sqrt{\langle I^2 \rangle} = \sqrt{\frac{4k_bTB}{R}} \quad (4.5)$$

where V_{rms} and I_{rms} are the root-mean-squared voltage and current measured across the resistor respectively, k_b is Boltzmann's constant, R is the magnitude of resistance. Angle brackets denote time averaging. B is the frequency bandwidth over which the measurement is made and is defined as, $B = f_h - f_l$. In most cases simply stating the bandwidth without the frequency range can be ambiguous when the PSD is frequency dependent. By convention, noise analysis does not include the zero frequency or 'DC' component of the signal, equivalent to setting f_l to be very small but slightly above zero. Unless otherwise specified, it is typically understood that $f_h \approx B$. In data presented in this work, we assume $f_l \approx 1$ Hz range, unless otherwise specified.

These equations as written imply that a measurement system with infinite bandwidth will measure infinite RMS noise and hence infinite energy, however, at very high frequencies, the conducting charges move ballistically and are not in thermal equilibrium with their surroundings. The timescale of these interactions for ions in solution can be roughly estimated from the mean free path l predicted by the Drude model and assuming the characteristic energy is equal to k_bT from

the equation

$$\tau = \frac{l}{v} = \frac{(\pi d^2 n_d)^{-1}}{k_b T / 2 m_{ion}} \approx 1 \text{ fs.} \quad (4.6)$$

where $d = 0.3 \text{ nm}$ is the approximate size of an ion, n_d is the number density of water molecules, and m_{ion} is the mass of a chlorine ion. The corresponding frequency of interaction τ^{-1} is well above the gigahertz range accessible to modern electronics and certainly above the 500 kHz bandwidth accessible by the digitizer used in this work and hence the approximations made in Equation (4.5) are adequate for this work.

It is important to note that $S_{I,therm}$ is frequency independent and hence all spectral frequencies have the same amplitude. By analogy with optics, this type of noise can be referred to as ‘white’ noise.

4.3.2 Capacitance

An important question arises when one considers the thermal noise of systems that aren’t purely resistive. Equations (4.4) and (4.5) can be extended to the case of RC networks by using the admittance of the circuit, Y , resulting in

$$I_{rms,therm} = \sqrt{4k_b T B \text{Re}(Y)} \quad (4.7)$$

$$S_{I,therm} = 4k_b T \text{Re}(Y). \quad (4.8)$$

This formulation is important once we realize that the membrane containing the nanopore acts as a capacitor in parallel with the pore resistance as shown in Figure 4.3 [111]. It has also been shown that the non-ideal dielectric loss in membranes typically used for nanopore experiments also has a noticeable contribution to the measured noise [112, 113]. This can be modeled as an admittance in parallel with the capacitance given by [111, 112, 113]

$$Y_{loss} = \omega C \tan \delta \quad (4.9)$$

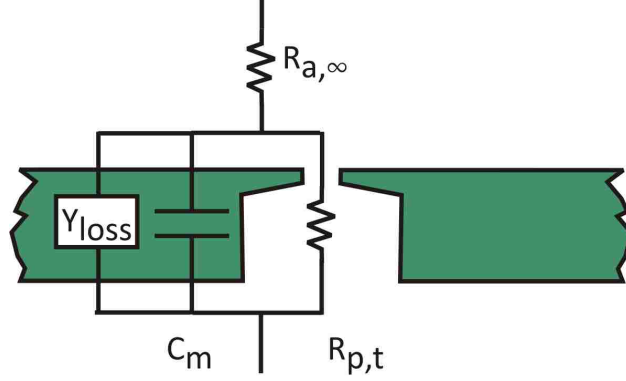


Figure 4.3: RC circuit model for noise analysis of nanopore. C_m is the membrane capacitance ≈ 10 pF, $R_{a,\infty}$ is the access resistance far from the pore, not including the spreading resistance adjacent to the pore and is typically < 100 k Ω , $R_{p,t}$ is the total resistance of the nanopore and surrounding area, on the order of 10 M Ω . Chapter 3 deals extensively with the calculation $R_{p,t}$.

where $\tan \delta$ is the loss tangent of the dissipation factor. For this circuit, the admittance becomes

$$Y = \frac{1}{R_{a,\infty} + \frac{1}{\frac{1}{R_{p,t}} + i\omega C_m + \omega C_m \tan \delta}} \quad (4.10)$$

This function produces an s-shaped monotonically increasing PSD as a function of angular frequency, $\omega = 2\pi f$, with a midpoint at roughly $(R_{a,\infty} C_m)^{-1}$. The loss tangent in similar SiN_x films was measured to be on the order of 0.01 [114] by traditional solid state AC methods, while a value of 0.27 ± 0.7 was reported by Smeets *et al.* for SiN_x/SiO₂ membranes containing nanopores [113], and by Hoogerheide for SiN_x/SiO₂ pores in solution was measured to be 0.031 [115].

For our nanopore system, square freestanding membranes of 30-50 μm on a side and 250 nm thick separate the two fluid solutions and produces a capacitance. This is complicated by the electrolytic capacitance that builds up due to the electrolyte on either side of the nanopore, as well as the input capacitance of the amplifier placed in series with the nanopore. We measure typical values of 40 pF as an estimate of the capacitance in parallel with the nanopore resistance measurement system. Estimates of the loss tangent vary by an order of magnitude for the loss tangent, and we assume a value of 0.03 since this value was determined in the conditions closest to our own. As will be shown shortly, the above mentioned effects are all present in our measured PSD, however, unexplained deviations between theory and the measured PSD cause us to treat

some aspects of our spectrum empirically, and hence overwhelm the uncertainty in our estimates of C_m and $\tan\delta$.

4.3.3 Shot noise

Shot noise is also a fundamental and unavoidable contribution to the noise of current passing through any system with randomly arriving discrete charge values [116]. If one assumes that the arrival of charges making up the current arrive independently, one can use the properties of Poisson statistics to derive

$$I_{rms,shot} = \sqrt{2qIB} \quad (4.11)$$

where q has been introduced as the charge of the charge carrier. Similar to our discussion with thermal noise, the power spectral density can be written as,

$$S_{I,shot} = 2qI. \quad (4.12)$$

This noise contribution is also frequency independent but scales linearly with current. We can already see that different noise sources are related to the mean parameters in ways that can be used to discover physics about the system under study. In the case of shot noise an experimenter can produce higher voltages across a circuit, producing higher currents. If the fluctuations in the system can be described by a combination of shot and thermal noise alone, the noise can be used to measure fundamental properties such as the charge of the electron and Boltzmann's constant. This in fact what is done in a number of undergraduate physics and electrical engineering labs [117]. The assumption that charges pass randomly depends upon their ability to occasionally 'bunch up' within the resistor on timescales that are short compared to the length of time it takes the charge carrier to pass through the resistor[116]. For an ionic system this means that the dielectric relaxation time $\tau_r = \epsilon_r \epsilon_0 \rho$ must be much less than $\tau_t = t_p / (\mu V)$, where ϵ_r is the relative dielectric constant of water, ϵ_0 is the permittivity of free space, ρ the solution conductivity, t_p is the pore thickness, μ is the electrophoretic mobility of an ion, and V is the voltage drop across the nanopore.

When the appropriate values for the parameters typical of those in this work are used $\tau_r > \tau_t$, thus we do not expect shot noise to be a significant contribution to the noise measured in this work.

4.3.4 $1/f$ noise

By far the most enigmatic—and oftentimes most troublesome—is the presence of low frequency noise far above that predicted by thermal noise. This noise often presents itself with a power law behavior as $S \propto 1/f^\beta$ where $0 < \beta < 2$ with typical values close to 1. This type of noise is present in many physical and biological systems including vacuum tubes, solid state devices [105], weather phenomena [118], astrophysical phenomena, motor vehicle traffic [119], and music [120]. Low frequency fluctuations of this form have been reported in the nanopore literature several times over the last half-decade [113, 112, 121, 122, 123, 124].

Because of its ubiquity, there have been many attempts to discover universal laws common to all systems exhibiting this noise, or at least descriptions of the physical mechanisms underlying the noise for specific systems. Research in this field is still very active, but progress has been slow. We will present here only two of these approaches and direct the reader interested in low frequency noise in solid state devices to the review by Dutta and Horn [105], and those interested in a wider set of phenomena to the article by W. H. Press [118].

The Hooge model

A widely used empirical model that sought to explain the magnitude of $1/f$ noise was proposed by Hooge in 1969, suggesting that that the PSD was proportional to the number of charge carriers in the sample N given by [125, 113]

$$S_{I, Hooge} = I^2 \frac{\alpha}{N} \frac{1}{f}. \quad (4.13)$$

In this relationship the PSD is also proportional to the square of the current through the system, however this is a result of Ohm's law rather than an insight into the source of flicker noise [126]. Hooge's experimental work suggested that the coefficient α/N was a constant for any material,

however, it was later shown that α varies over many orders of magnitude ranging from 10^{-8} to 10^{-2} for homogeneous materials [126]. Hooge's empirical theory was applied to electrons in solid state materials, but recent work by Smeets *et al.* has suggested that the Hooge relationship applies to solid state nanopores as well, with $\alpha = 10^{-4}$, comparable to values for α in many technologically relevant semiconductors [113]. Smeets also showed considerable variability in $1/f$ noise in their pores and their reported α should be considered a low estimate of the mean value for α .

4.3.5 Surface chemistry noise

Another noise source that is frequency independent within the bandwidth of our measurement system is the surface chemistry noise discovered explored by Hoogerheide [88]. He showed that nanopores fabricated with methods very similar to those in this work contain SiO_2 surface groups that undergo surface protonization reactions that influence the pore conductivity. These reactions are faster than can be directly measured with our measurement system, but manifest themselves as conductance fluctuations that depend upon the power of the surface protonization constant, pKa , solution pH , and nanopore surface potential ψ as

$$S_{I,surf} \propto I^2 \frac{10^{pKa-pH} e^{\psi/(k_b T)}}{(1 + 10^{pKa-pH} e^{\psi/(k_b T)})^3}. \quad (4.14)$$

For a neutral pH, this produced a noise

$$S_{I,surf} = I^2 10^{-10} / \text{Hz}. \quad (4.15)$$

This noise is on the order of the thermal noise measured for pores in this work. For a typical nanopore of $R_p = 10 \text{ M}\Omega$ with a current of 10 nA $S_{I,surf}/S_{I,therm} \approx 6$. In this work we assume that frequency independent contributions to the noise that scale with the square of the current are due to this model.

4.4 Combining noise sources

The separate noise sources discussed above must be combined in order to model the measured noise in nanopore systems. Each frequency bin of the PSD can be interpreted as an estimate of the mean variance of the Fourier components within that bin. Since the variances of random processes add linearly, the sum of independent PSDs add linearly. For the PSDs mentioned, the total PSD and RMS noise become

$$S_{I,total} = S_{I,therm} + S_{I,Hooge} + S_{I,surf} \quad (4.16)$$

$$I_{rms,total} = \int_{f_l}^{f_h} (S_{I,therm} + S_{I,Hooge} + S_{I,surf}) df. \quad (4.17)$$

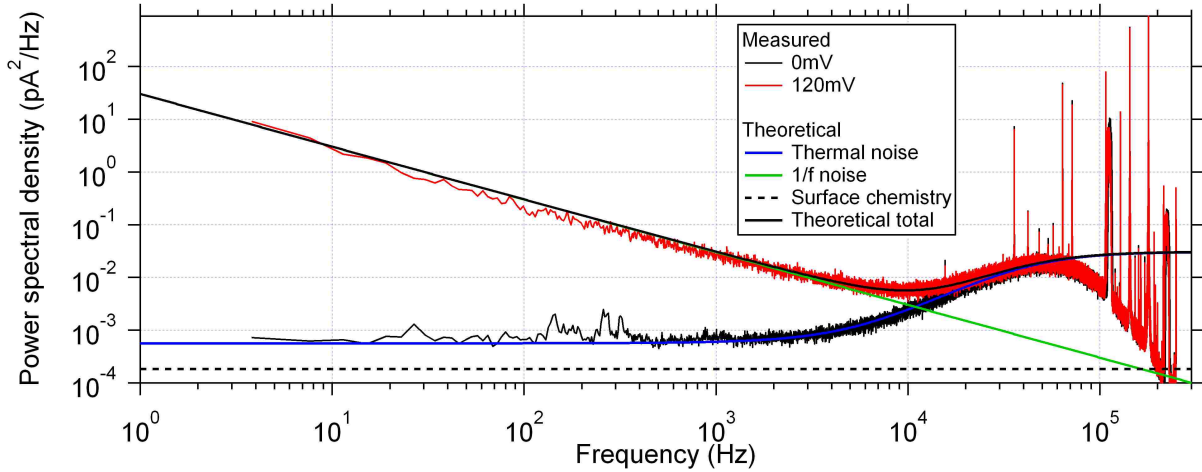


Figure 4.4: The same PSDs for no bias and 120 mV applied bias as shown in Figure 4.2, but with theoretical noise contributions depicted. Note the log-log scale and that for nearly every frequency regime, the largest noise contribution dominates the spectrum. The fit demonstrated here is qualitative and parameters used to fit the data were selected manually, nonphysically low membrane capacitance C_p and high access resistance R_a were required. Roll-off after 100 kHz is due from 8-pole analog Bessel filter used while taking the data.

In order to model the PSD, all the necessary parameters must be known or fit from the data. Values for $R_{p,t}$ are measured in a straightforward manner using Ohm's law and applying a step voltage of a known magnitude and waiting for any transient behavior to decay. Values for C_m and $R_{a,\infty}$ can be found by applying a step function voltage waveform and fitting the response curve. N , the number of charges in the pore can be estimated from the ion concentration of the solution and

pore size, assuming that at high salt concentrations the pore environment is the same as the bulk [87, 113]. The loss factor $\tan\delta$ can be determined by fitting the PSD at no applied bias, and α can be determined by fitting the PSD at an applied bias.

Figure 4.4 shows the combination of the main noise sources used to model the total noise in the nanopore. At 0 mV, no net current flows and only thermal noise remains. Varying the parameters for capacitance and resistance in Equations (4.8) and (4.10) provides a qualitative fit sufficient to explain the observed PSD at 0 mV. At 120 mV, the $1/f$, shot, and surface chemistry noise sources that increase with current are present in addition to the thermal noise, however, both the shot and surface chemistry noises are negligible and the additional noise can be modeled as an increase in $1/f$ Hooge noise.

Although seemingly straightforward, producing fits in this manner do not model the data self-consistently. Values required for R_a and C_p to fit the data are off by an order of magnitude of those measured using voltage steps, and parameters such as D and α vary by orders of magnitude from sample to sample. We emphasize here, however, that the qualitative behavior of a $1/f$ decrease into the kHz range, followed by a rise until the filter begins attenuating the signal around 100 kHz is well explained by our PSD model, and the low frequency behavior of the generalized thermal noise, the noise dominated by R_p alone, fits the data at zero applied bias very well.

All is not lost, though! Figure 4.5 shows that the ‘quiet’ pore depicted in Figure 4.1A does not have as much $1/f$ noise. In this figure we see a roughly constant region from 30 Hz to 5 kHz. This region is too low a frequency to be affected by the capacitive thermal noise and dielectric loss noises and can be modeled by the low frequency thermal noise in Equation (4.4). The only remaining contributions are the $1/f$ and surface chemistry noise sources, however, as shown in Figure 4.4, $1/f$ noise, when present, can dominate in this regime. We show below in Section 4.6.3 that measuring the integral under the PSD, namely I_{rms} , over the 30Hz to 5kHz bandwidth is sufficient to group pores into $1/f$ dominated ‘noisy’ pores and surface and thermal noise dominated ‘quiet’ pores.

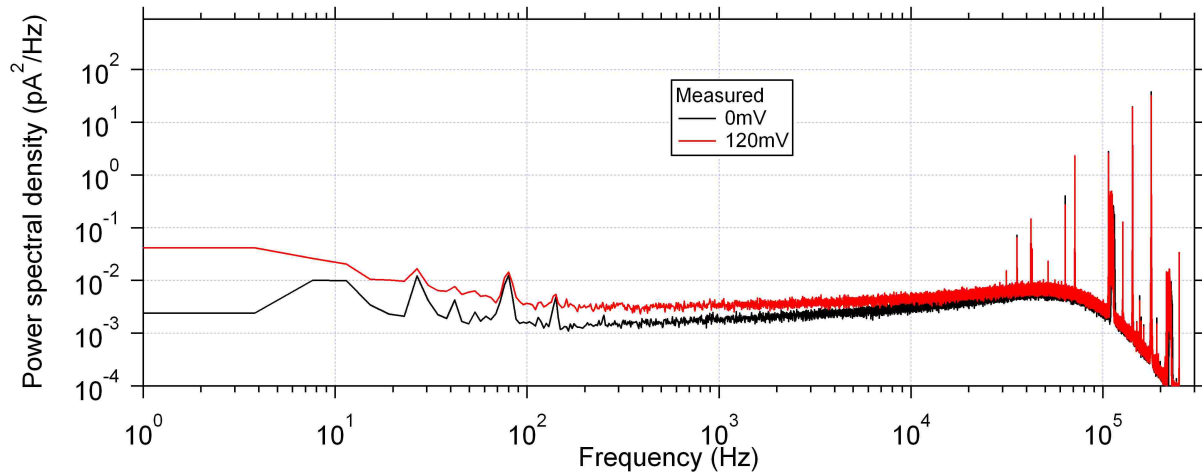


Figure 4.5: Power spectral density of current fluctuations through ‘quiet’ nanopore shown in Figure 4.1

A.

4.5 Amplifier Noise

So far we’ve assumed that we can measure our nanopore system without any influence from the measurement electronics and, as alluded in the beginning quotes in this chapter, no discussion on noise would be complete without considering the influence of the environment outside the nanopore system.

All sharp peaks in the PSD can be traced to outside influences that can usually be identified by their characteristic frequency ranges. In the sub 100 Hz range, mechanical and acoustic vibrations can appear. Peaks in the ≈ 100 Hz to 1 kHz range are usually due to the AC mains voltage and its harmonics, and peaks in the 10 kHz range and above are due to higher frequency electromagnetic interference coupling radiatively or through the power line for our measurement equipment.

More important are the sources of noise in the amplifier that result from the same physical noise sources present in the nanopore, most important of which is the thermal noise of the feedback resistor used in the transimpedance amplifier discussed in Chapter 2. There are two user selectable feedback resistors, R_f , available on the Axopatch 200B headstage, referred to on the Axopatch as the whole cell β settings, 50 M Ω ($\beta = 0.1$) and 500 M Ω ($\beta = 1$). The open circuit RMS noise measured over a 5 kHz bandwidth was 1.46 pArms and 0.48 pArms for the 50 M Ω and 500 M Ω

resistors, respectively. Because of the linear dependence of noise on temperature, the headstage is actively cooled using to 25° C using an on-board peltier device. Using Equation (4.4) at this temperature we estimate the thermal current noise contribution of 1.22 pArms for the 50 MΩ and 0.38 pArms for the 500 MΩ resistor. Most of the remaining noise comes from the field effect transistors used to construct the amplifier [111].

To compare the magnitude of this noise contribution to the noise in a nanopore experiment we first calculate the thermal noise of a typical nanopore assuming zero membrane capacitance. In this work the average nanopore resistance was on the order of 10 MΩ, resulting in a thermal RMS noise of 2.84 pA. Because this noise is uncorrelated with the thermal and amplifier noises of the headstage we can add the noise in quadrature [111], yielding a total, minimum predicted noise of

$$\begin{aligned}
 I_{rms,total} &= \sqrt{I_{rms,R_f}^2 + I_{rms,amp}^2 + I_{rms,pore}^2} & (4.18) \\
 &= \begin{cases} 2.88\text{pArms} & \text{for } R_f = 500\text{M}\Omega \\ 3.19\text{pArms} & \text{for } R_f = 50\text{M}\Omega \end{cases}
 \end{aligned}$$

where $I_{rms,amp}$ is chosen to account for the difference in thermal feedback noise and measured noise. For the 500 MΩ resistor, the measured noise is within about 1% of the theoretical value, but the 50 MΩ resistor has a noise contribution of about 10%. Clearly, the higher value resistor is the best choice, however, currents larger greater than 20 nA saturate the frequency-dependent gain circuit implemented after the transimpedance amplifier. The maximum voltages applied to study noise in this work were ±200 mV, this means the lower noise setting could only be used for pores with resistances higher than about 10 MΩ. As shown in Figure 4.6, the maximum contribution of amplifier noise was around 11% and was highest for pores with resistances just less than 10 MΩ. This was unfortunate since 10 MΩ was the typical pore resistance for this work, requiring most data to be taken at the high noise setting. Care was taken to note the amplifier setting to facilitate data analysis. Figure 4.6 shows the maximum error and is only approached for the case of zero applied bias and is insignificant for noisy pores with flicker noise. Perhaps counterintuitively, the noisier the nanopore, the more accurate the measurement of noise.

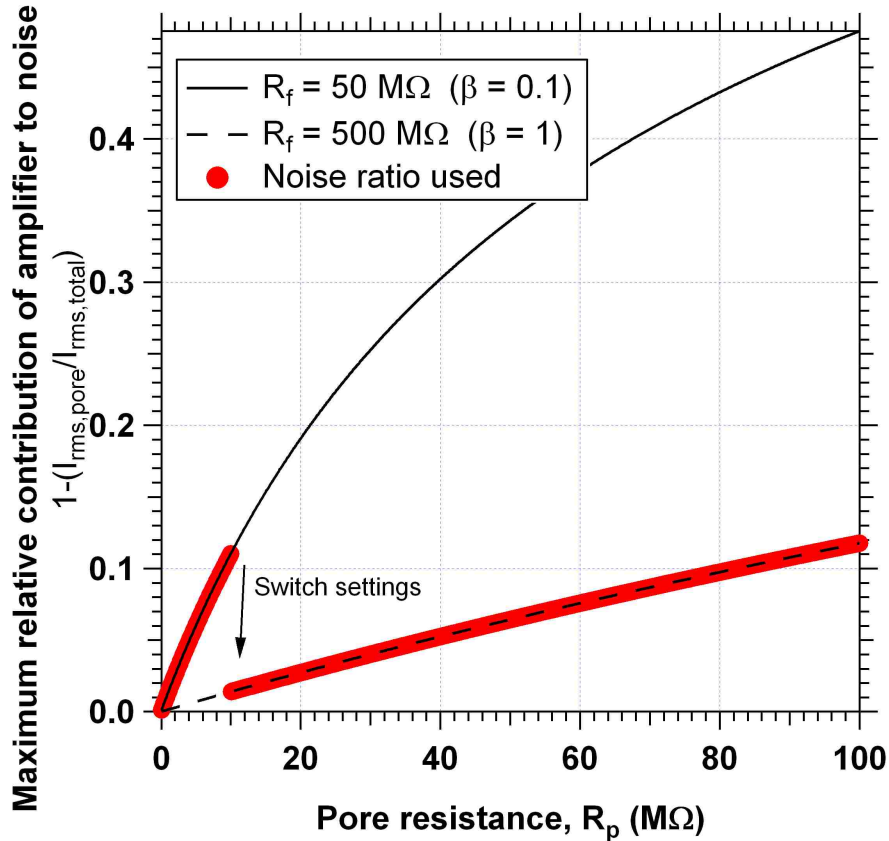


Figure 4.6: Maximum relative RMS noise contribution of amplifier noise to nanopore measurement.

4.6 Comparison of noise between Ne and Xe fabricated pores

As outlined in Chapter 2, nanopores can be fabricated using any noble gas. Preliminary work by Dr. Jiali Li suggested that there was a repeatable difference in noise between pores fabricated with neon and xenon, and preliminary work on annealing samples after fabrication at temperatures up to 1000° C showed a possible reduction in noise.

Silicon nitride has been investigated as a thermal diffusion barrier against embedded ions for decades [127, 128], and the concentration of nitrogen has been shown to be directly related to the reduction of diffusion in silicon oxynitrides [129]. Previous research also shows that embedded material such as boron leave silicon and silicon oxynitrides in a temperature dependent diffusion process [129, 130]. Although the growth of a thermal oxide on silicon nitride is much slower than silicon, the oxides have been shown to grow in oxygen containing atmospheres at both room

temperatures and elevated temperatures [61]. Our hypothesis was that noble gas used to fabricate the pore changed its PSD and that annealing was causing the diffusion of the imbedded noble gas atoms out of the material, bringing the pores fabricated by different ion beams to the same, low noise state.

Preliminary work by Dr. Jiali Li also showed that surface roughness changed as a function of noble gas used to fabricate the nanopore, with pores fabricated with xenon having smoother surfaces than those fabricated with other noble gases. It has been suggested that the surface topology within nanopores affects fluid transport [131, 132] and that the electro-osmotic flow near surfaces can vary significantly with nanoscale roughness [133]. To investigate if surface topology also affected fluctuations in ionic flow, we collaborated with Dr. Hoogerheide in the lab of Dr. Golovchenko at Harvard to measure surface roughness near nanopores using the atomic force microscope (AFM) for nanopores fabricated with Ne, Ar, and Xe, and as a function of annealing. To investigate the possibility of gas dependent noise differences, we also fabricated pores with Ne and Xe and measured the noise during ionic current flow to determine if a repeatable difference in noise was present and then annealed these samples to see if the diffusion of gas out of the pore forming material could produce pores with identical noise characteristics.

4.6.1 Methods

We fabricated approximately 30 pores using the protocols outlined in reference [52] and Chapter 2, with a typical flux of $1 \text{ ion/nm}^2 \text{ sec}$ and wet them as outlined in Chapter 2. Current noise measurements were made using a 4 pole Butterworth analog RMS meter which measured I_{rms} from 30 Hz to 5 kHz. Although not used for the comparison in noise between samples presented here, we also measured current for at least 10 seconds at 0 mV bias and 120 mV bias with a 100 kHz low pass 8-pole Bessel filter and oversampled our data at either 250 kHz or 500 kHz. This data was used to produce the PSD of the signal when necessary for troubleshooting. Annealing was done in either lab room air, nitrogen, or argon, with zero flow in the case of lab air and flow rates on the order of 2 sccm for nitrogen and argon. Gas flow was done in one of several standard tube furnaces and

was chosen low enough to ensure temperature stability, but to allow at least hundreds of exchanges of the gas in the heated tube. No dependence on gas flow rate was seen. Material composition of the surface of our SiN_x before and after baking and as a function of noble gas used to fabricate the pore was measured using X-ray photoelectron spectroscopy (XPS) using a monochromated Aluminum K_α source at an energy of 1486.6 eV. XPS is a highly surface sensitive method that probes only 10 nm into the surface of the material [134]. XPS is a fascinating method and readers interested in a practical introduction are recommended to consult the book edited by Briggs and Seah [135]. Samples measured for noble gas out diffusion were dosed with 100 ions/nm² over a 2 mm x 2 mm area by rastering a 120 μm beam. Dosing took approximately 1 hr per sample. All AFM roughness scans were measured over a 1 μm x 1 μm patch at a resolution of 512 x 512 pixels with a scan rate of 1 Hz per line in tapping mode in air. Tips used were the Mikromasch NSC-35 and Olympus AC240TS. For the roughness measurement, samples were dosed with noble gas ions as above. Roughness measurements were measured before and after dosing. The roughness of two samples dosed with argon were also annealed at 850° C in air for 1 hr and roughness measured again. Roughness was calculated as the RMS value of heights measured for all pixels in each image after flattening by subtracting a line-by-line linear fit.

4.6.2 Material characterization

Annealing

An example of a survey scan of our SiN_x material is shown in Figure 4.7. This survey shows the expected peaks from silicon, nitrogen, and xenon, as well as the presence of oxygen at the surface. Oxygen is also expected for SiN_x that has been exposed to air, with up to 1 nm of oxygen rich material growing in 1 month [61]. Baking 1 hr at 1000° C in air shows a clear increase in oxygen and nitrogen as seen from the increase in their 1s peaks, and a clear decrease in xenon as shown by its 3d peak, with a nearly constant concentration of silicon. A closer view of the xenon 3d peaks in a similar sample as shown in Figure 4.8 shows the reduction in the integrated area of the peaks as the sample is baked at higher temperatures. Also evident is a shift in peak energy due to surface

charging caused by the incident x-rays that does not effect the quantification of material [136]. By comparing the integrated area of each peak after extracting the background we can determine the relative change in each component [137].

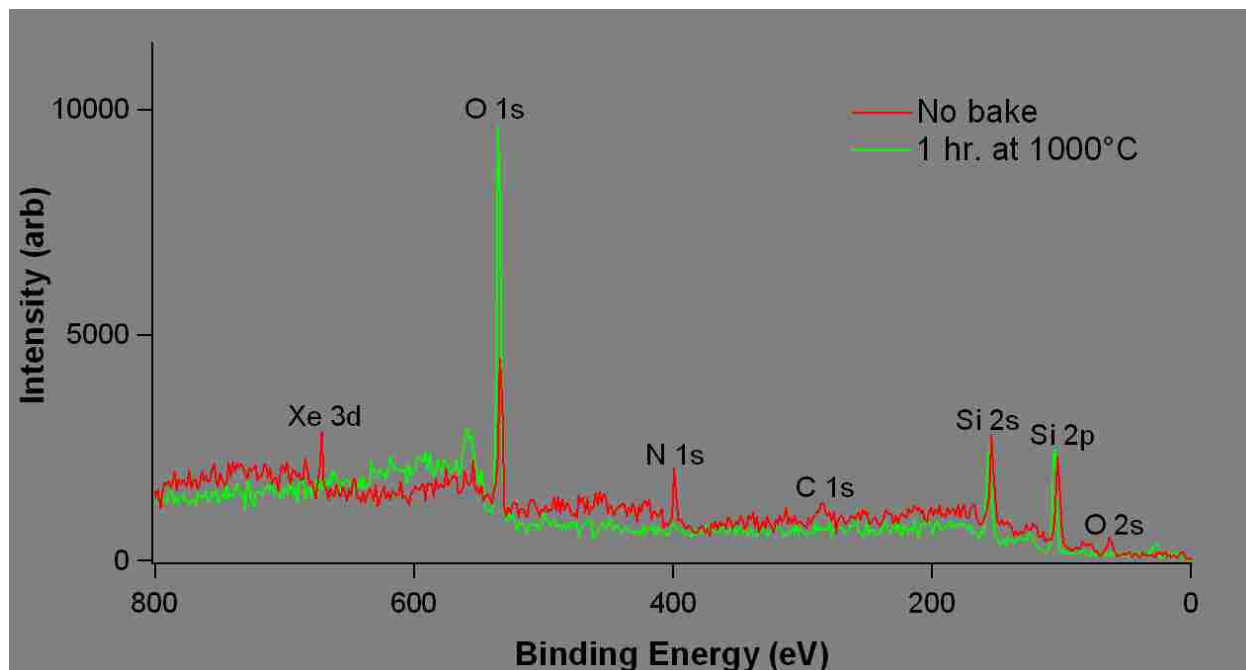


Figure 4.7: An XPS survey scan before and after annealing a SiN_x sample in air. The expected Si and N peaks are clear, along with the oxygen from a surface oxide formed before baking. This sample was also dosed with Xenon before baking.

We first established that a silicon oxynitride layer grew on our sample when annealed in air, as shown in Figure 4.9, consistent with previous work [61]. We then annealed three samples that were dosed with neon, argon, and xenon, respectively and then baked for 1 hr at 600°C and then again at 100°C in air. The resulting relative change in concentration is shown in Figure 4.10. The concentration of three noble gases clearly reduced with heating in air. To determine if out diffusion of the embedded gas was aided by the increased oxygen content, we dosed a SiO_2 membrane with argon and annealed to 600°C and measured the presence of argon using RBS in collaboration with John Chervinsky at Harvard. The results shown in Figure 4.11 show that annealing for 1 hr indicates complete removal of the argon, suggesting a much higher diffusion rate in SiO_2 than in SiN_x . We then dosed two SiN_x samples with argon and xenon separately and annealed them in an inert argon atmosphere that prevented the growth of the oxide layer as shown in Figure 4.12. Both

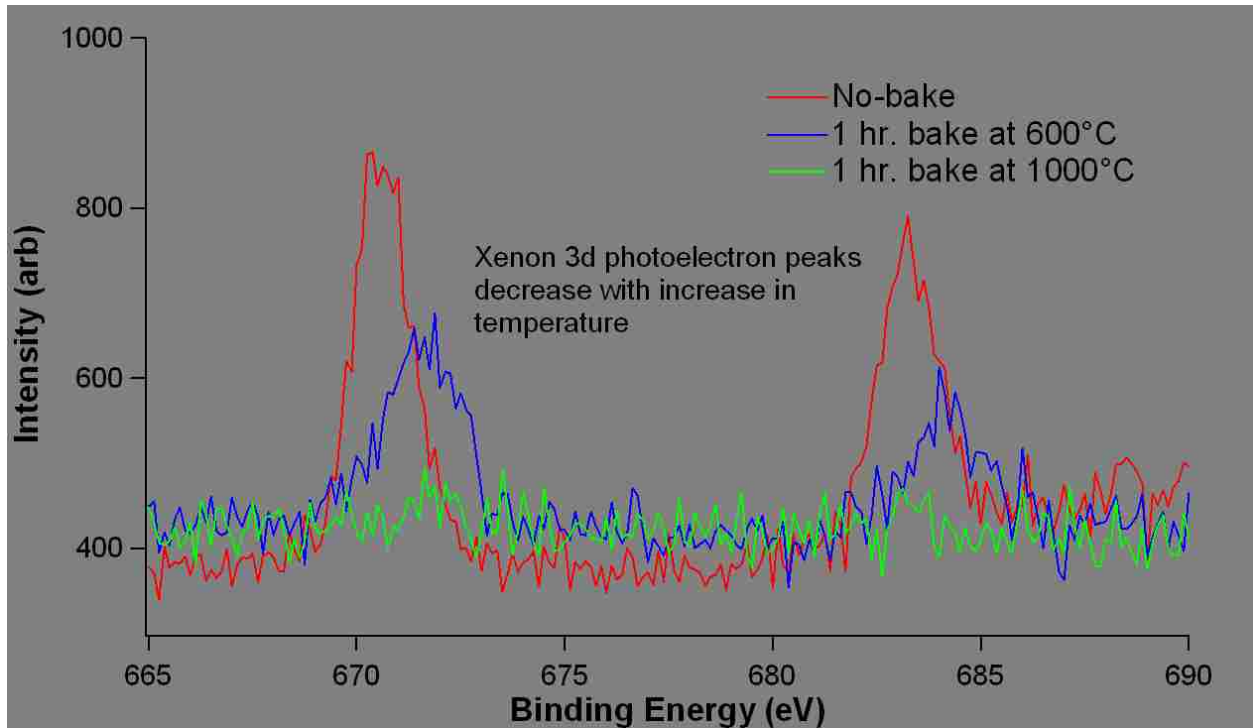


Figure 4.8: The area under the intensity peak is proportional to the concentration of the element studied. Here, xenon is shown decreasing with increase in bake temperature.

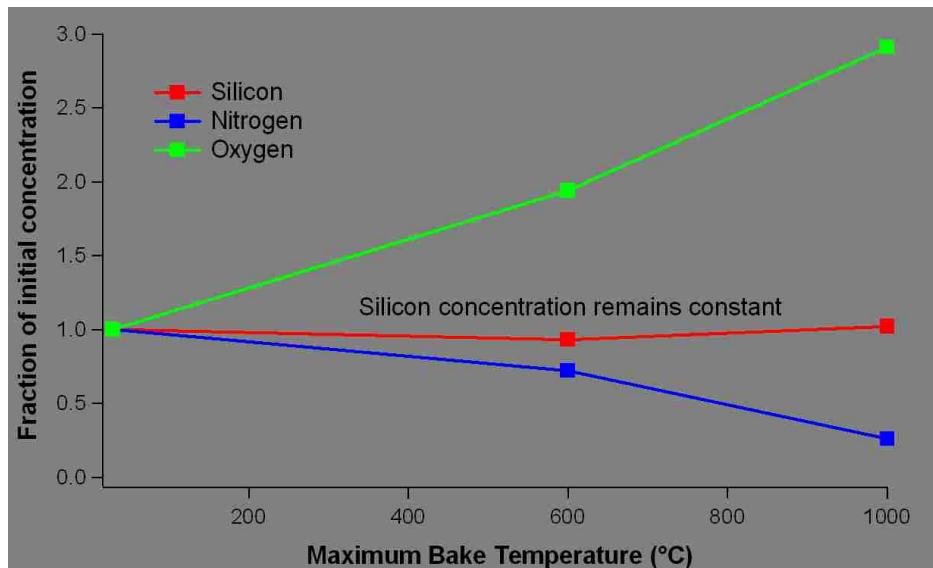


Figure 4.9: Relative change in silicon, nitrogen, and oxygen for a typical SiN_x sample. The sample was first baked for 1 hr at 600°C and then for 1hr at 1000°C

argon and xenon were retained at much higher rates than in SiN_x annealed in air.

In order for thermal oxidation of SiN_x to be a significant factor influencing the out diffusion of embedded gas, the penetration of oxygen must be near that of the embedded material. Previous

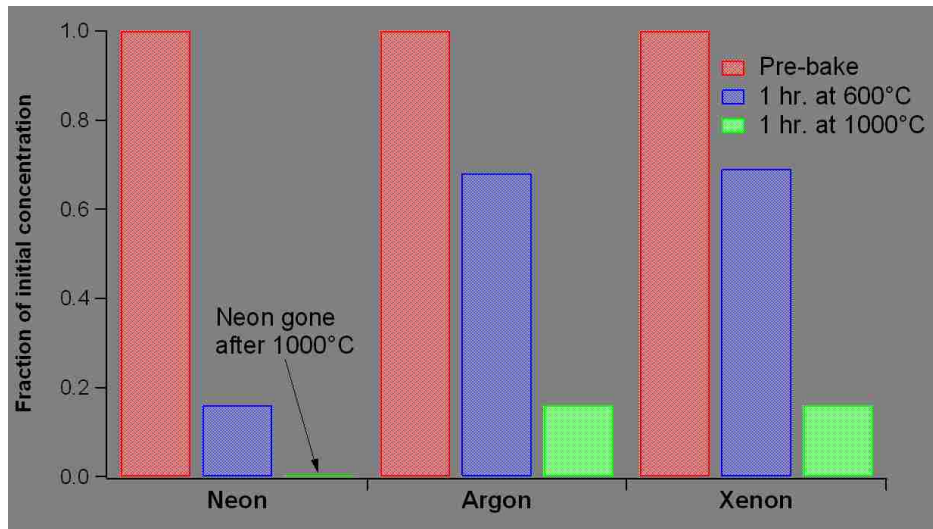


Figure 4.10: Relative change in neon, argon, and xenon imbedded in SiN_x . Each sample baked for 1 hr at 600°C and then for 1hr at 1000°C .

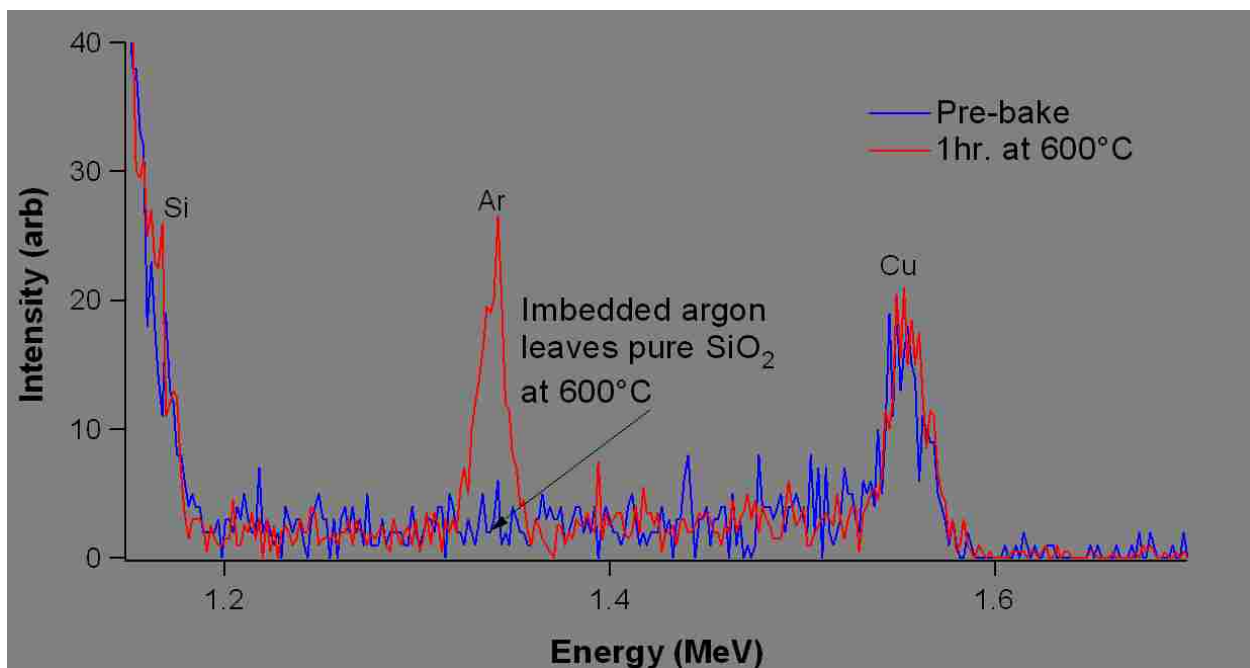


Figure 4.11: RBS spectrum demonstrating diffusion of argon out of pure SiO_2 sample after 1 hr annealing at 600°C . The silicon peak is due to silicon substrate and copper peak is due to the copper sample holder.

computational work in our lab [12], reproduced in Table 4.1, show that the mean location for the embedded gas is between 4.3 nm to 4.6 nm. To verify this calculation, a depth profile was measured using argon ion milling of a xenon embedded sample. In this procedure, XPS is used to quantify the amount of material, in this case xenon, layer by layer after repeated 4 keV argon

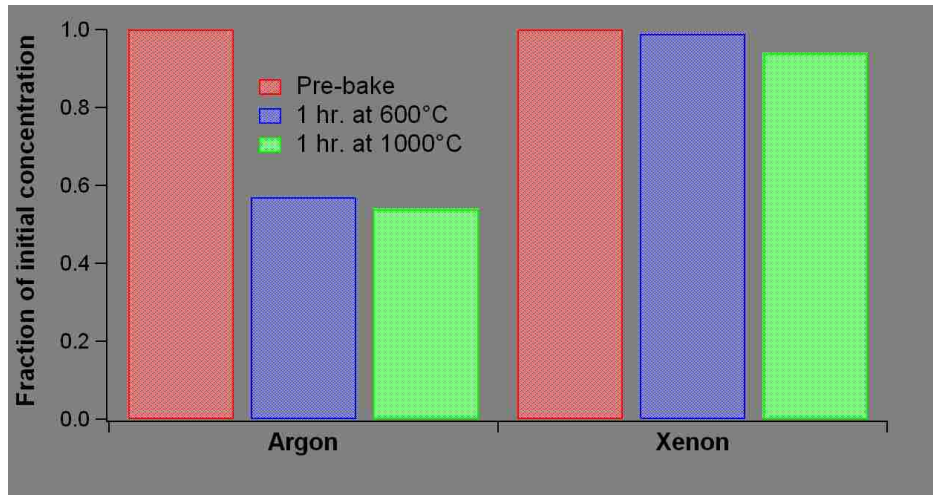


Figure 4.12: Relative change in concentration for embedded argon and xenon out of two separate SiN_x samples annealed in an inert argon atmosphere. Without an oxidizing agent, both argon and xenon are less mobile.

ion sputtering steps. To calibrate the depth sputtered as a function of argon sputtering time, a 50 nm SiN_x membrane was deposited on silicon and sputtered until completely removed. Using this calibration, the resulting depth profile is shown in Figure 4.13, consistent with the 4.6 nm mean depth estimate shown in Table 4.1. Thermal oxidation of SiN_x annealed for 1 hr in air at 1000°C is predicted to produce a graded oxynitride with oxygen concentrations greater than nitrogen at depths down to 5 to 10 nm[61], which is the same penetration range expected for each embedded gas in our sample.

	Ne	Ar	Xe
Mean depth (nm)	4.5	4.3	4.6

Table 4.1: Mean penetration depth for ions embedded in SiN_x at 3 keV. Data from SRIM calculation from work previously done in our lab. Reference in the main text.

Our annealing experiments show qualitatively that out diffusion of embedded gas occurs in both SiN_x and SiO_2 , with lighter elements diffusing faster than heavier ones and out diffusion increasing with oxygen content. The expected depth of oxidation is also the same as the depth of gas implantation, which is consistent with the hypothesis that increases in oxidation are responsible for the increased out diffusion of ions from SiN_x .

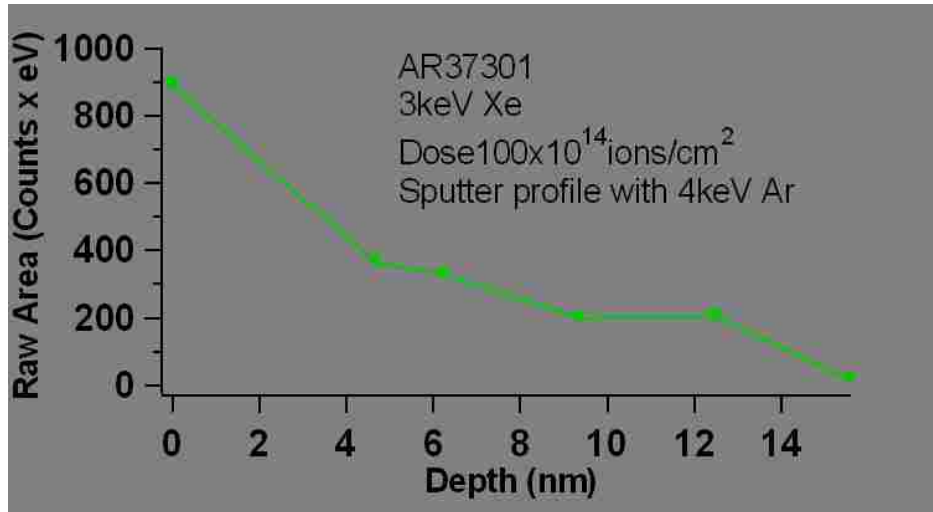


Figure 4.13: Depth profile of xenon embedded in SiN_x at 3 keV.

AFM

An example topography for an argon dosed sample is shown in Figure 4.14. The sample was dosed in the same manner as those used for XPS and RBS measurements and then annealed for 1 hr at 850°C and with a patch of surface scanned after each step. These images show that the height of our SiN_x surface varies over a range of nearly 10 nm. Embedding the noble gas reduces the surface roughness by reducing the lateral variation at the 100 nm length scale, but retains some of the variation at longer length scales. In other words, the magnitude of variation is reduced for all features, but small, spiky variations are preferentially removed. After annealing, the magnitude of surface variation is further reduced. These results are summarized for argon and xenon in Table 4.2. These preliminary AFM results suggest that high mass noble gas produce a significantly smoother surface, and that annealing in air produces a slightly smoother surface.

	Ar	Xe
R_{post}/R_{pre}	0.69	0.06
R_{bake}/R_{pre}	0.63	-

Table 4.2: Relative change in RMS roughness for samples dosed with argon and xenon. R_{pre} and R_{post} are the RMS roughnesses before and after noble gas dosing, respectively. R_{bake} is the RMS roughness after first dosing then annealing for 1 hour at 850°C . Typical values for R_{pre} are 0.80 nm.

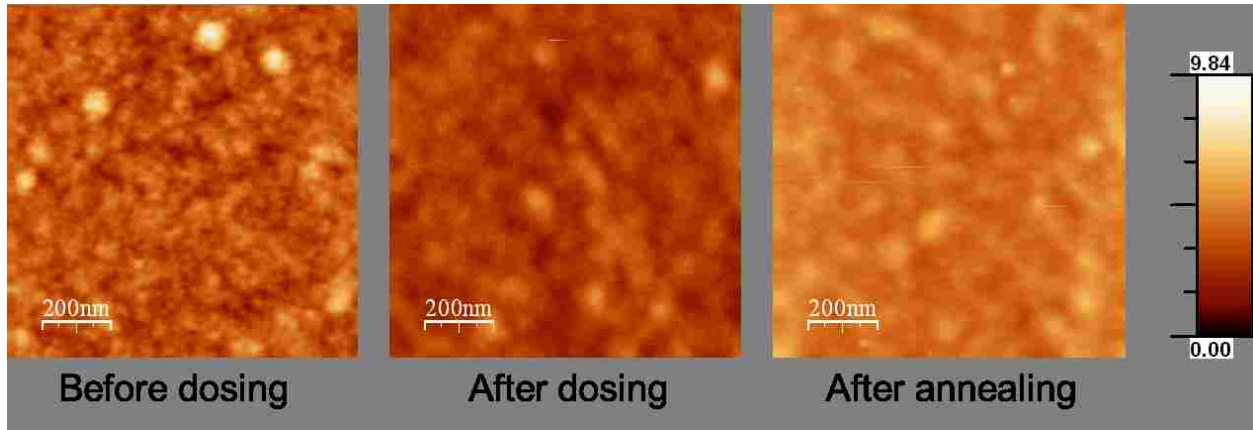


Figure 4.14: Example AFM topographies of sample before dosing with argon, after dosing, and after annealing. Scale bar for height shown on the right.

4.6.3 Noise results and discussion

Trends for all pores observed

The RMS noise for all pores was measured at zero applied bias and 120 mV bias for pores fabricated with both xenon and neon and that were both annealed and not annealed as shown in Figure 4.15. Each pore has two markers on the graph, a filled marker, representing the noise at zero applied bias, and an unfilled marker, directly above it representing the noise at 120 mV applied bias. The location along the abscissa for all points is determined by the current measured at 120 mV for that pore. The red markers represent pores fabricated with xenon, and the blue markers represent pores fabricated with neon. Lozenges (\diamond) represent baked samples while circles (\circ) represent unbaked samples. The first clear pattern is that no pores exhibit a noise below the wedge shape region forbidden by the thermal noise baseline of Equation (4.5). All pores at zero applied bias (filled markers) lie very close to this line, and deviations can be explained by the small amount of noise added by the amplifier itself. At an applied bias (unfilled markers), the situation is different. At 120 mV, 22 of the 29 pores shown in Figure 4.15 have approximately 2 pA noise in excess of the RMS noise measured at zero bias, while the remaining 7 pores have much higher noise levels.

Looking more closely at the difference between the noise at 120 mV and zero bias as shown in

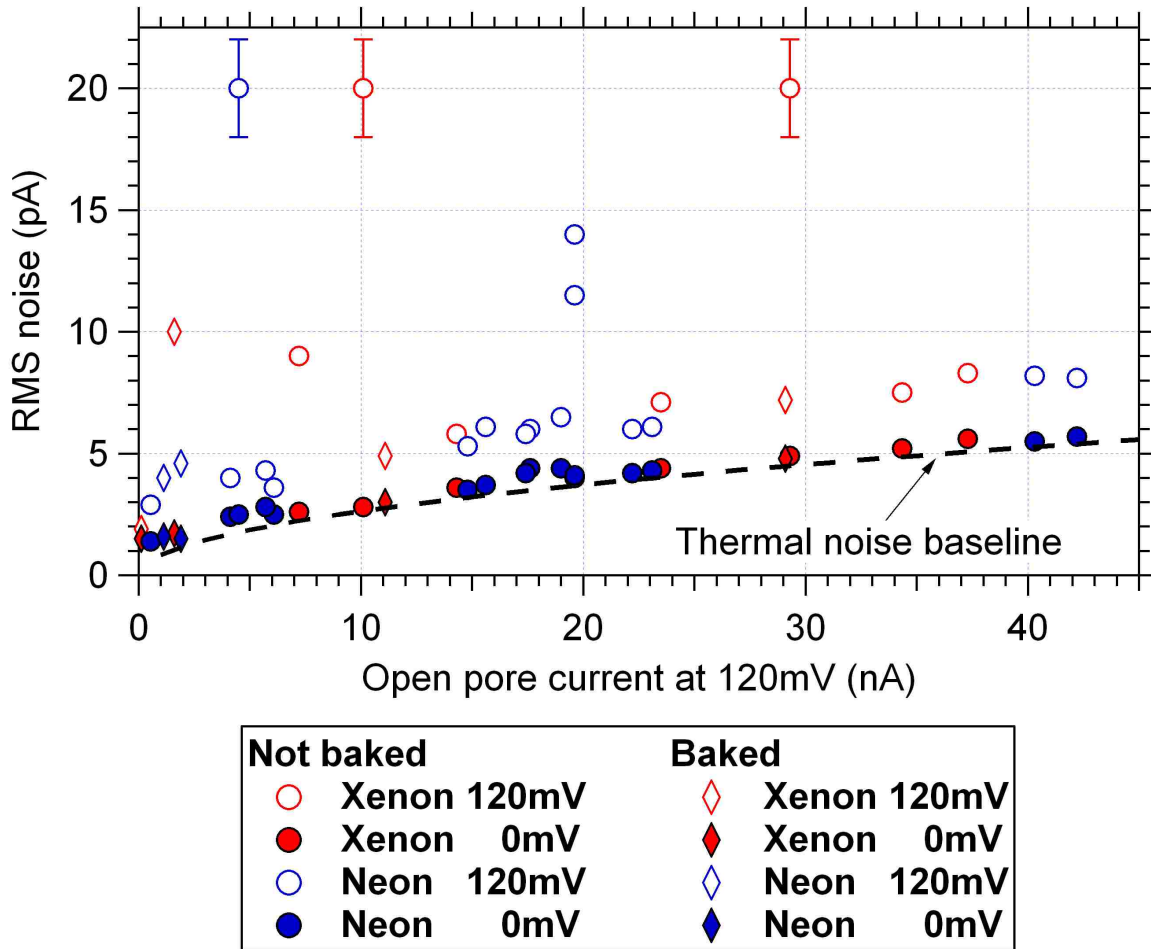


Figure 4.15: RMS noise over the 30 Hz to 5 kHz bandwidth for each pore measured at zero applied bias and 120 mV bias. Error bars unless shown are approximately the width of the marker and omitted for clarity.

Figure 4.16, the approximately 2 pA difference in RMS noise can more clearly be seen. Subtracting the zero bias noise removes the thermal noise, leaving only the $1/f$ and surface chemistry noise sources. If we assume that only surface noise is present at the levels measured by Hoogerheide, the noise is correct to the right order of magnitude. By inspection of the PSDs of these pores, the $1/f$ noise was small in magnitude in many of them, with a larger $1/f$ noise more common in pores < 10 nm in diameter.

If we look closer at the trend in the noise as current increases, we see that there is a gradual rise in the RMS noise as current increases. To suggest an explanation for this trend we rearrange

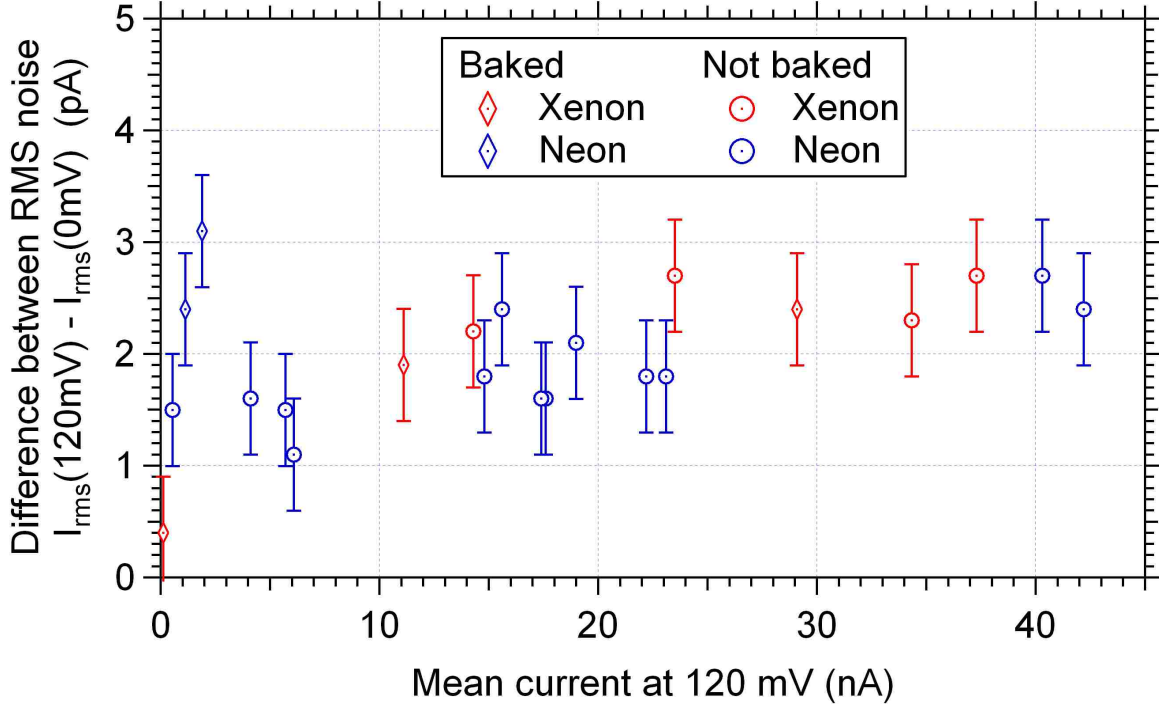


Figure 4.16: Difference in noise measured at 120 mV and zero bias, each pore is represented by a single marker. Dashed line is a fit to data points with RMS noise less than 5pA.

4.13 and integrate to write the flicker noise in terms of its RMS value, yielding

$$I_{rms,Hooge} \propto \frac{I_0}{\sqrt{N}} \quad (4.19)$$

If we assume the pore thickness is on the order of the pore radius, we have $N \propto V_p \approx r_p^3$, where V_p is the pore volume and $I_0 \propto r_p$, thus

$$I_{rms,Hooge} \propto \frac{I_0}{\sqrt{I_0^3}} = I_0^{-1/2}. \quad (4.20)$$

Thus we'd expect the $1/f$ noise to decrease as the mean open pore current at a fixed voltage increases and therefore cannot explain this trend. It is likely that that a combination of these noise sources are present and that future experiments measuring the full PSD at many voltages for each pore would illuminate the underlying mechanism.

No difference between pore fabrication method observed

The hypothesis that pores fabricated by neon and xenon produce repeatable differences in noise is not supported by this data. No clear trend emerges that differentiates the noise for neon and xenon pores. The preliminary observation that pores fabricated with different noble gases had different noise levels could be attributed to the fairly high probability of outlier ‘noisy’ events with noise levels > 3 pA above the thermal baseline. These pores have much higher $1/f$ noise which has been reported in the literature to be highly variable and possibly due to contamination, not the pore itself [113]. Another possibility is the fact that the mean pore current was typically much larger than the open pore current predicted using the methods discussed in Chapter 3. Although this data was taken before the TEM based methods used to measure pore thickness were developed, Figure 4.17 shows an estimate of the mean current using the conductance prediction methods of Chapter 3 and indicates that nearly all pores have currents several times larger than those predicted. We conclude that most of the pores have opened significantly and that if differences in noise between fabrication methods exist, they are likely to be found only in pores that are more stable.

4.7 Conclusion

We cannot conclude that there is any difference in noise characteristics based on the noble gas used or annealing of solid state nanopores made from SiN_x using the ion beam sculpting method. We conclude that the thermal, Hooge, and surface chemistry noises can explain the qualitative frequency dependence of the noise measured in all nanopores. We show clear trends in the out diffusion of noble gas being faster for lower mass embedded atoms, and that annealing in air forms an oxide layer that increases the out diffusion more than annealing in an inert atmosphere. We also show that bombarding the surface of SiN_x reduces its surface roughness and suggest that higher mass ions smooth the surface more. The lack of an observed correlation between noise and fabrication gas or annealing history means that surface roughness and annealing history do not likely have a significant effect on the noise in solid state nanopores.

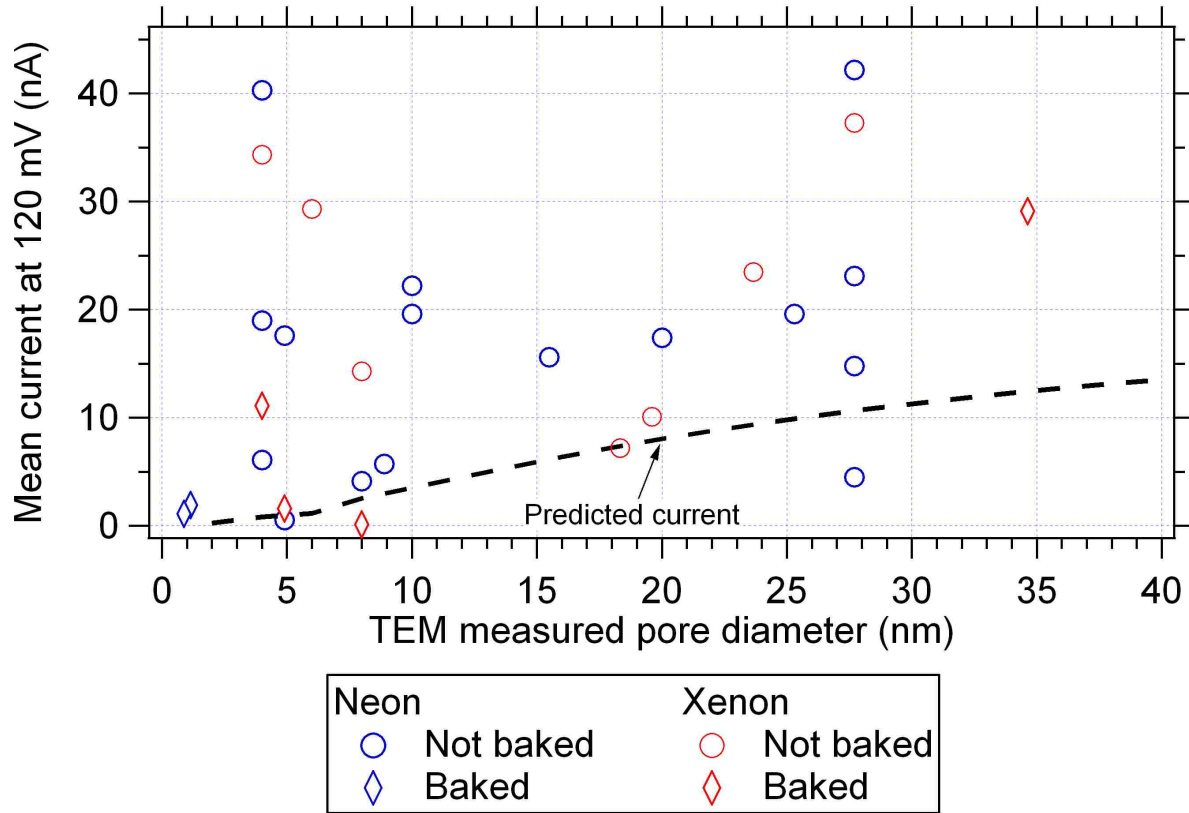


Figure 4.17: Mean current through nanopores used in the noise study vs diameter as measured by TEM.

4.8 Future work

Future work on noise would be to measure the noise for nanopores that are stable and do not open quickly when exposed to liquid. This would guarantee that any surface specific effects in the as-fabricated sample would remain and could possibly present differences in the noise between fabrication methods. A more thorough characterization of the circuit model to determine the PSD that models the entire system including the macroscopic electrodes could possibly correct for the high frequency thermal noise. An investigation of the PSD measured as a function of applied voltage and hence current for a given pore should show the linear behavior uncomplicated by the discussion surrounding Equation (4.20). Combining this data with better control of the nanopore size, a better estimate of N could be made and the coefficient α could be explicitly investigated, along with values for the magnitude of the surface concentration noise. To change N , salt concen-

tration can be varied in the pores as well, similar to the work done by Smeets [113] giving an even stronger determination of α . Other parameters such as salt concentration and pH could be varied to modify the surface chemistry and probe the pH dependent characteristics of the noise.

There is a tantalizing but speculative explanation of the $1/f$ noise outlined in the review on noise by Dutta and Horn [105] (see section B: Diffusion) that uses the diffusion equation to model the variation of any parameter coupled to conductance. The work by Weissman [138] showed that any homogeneous conductor split in half by a thin insulating plane with a single, circular pore allowing conduction can show $1/f$ noise given that the diffusion of this parameter satisfied the relationship $f \gg D/r_p^2$ for a pore of radius r_p and a diffusion coefficient D . Weissman's 'diffusing parameter' could be any physical quantity coupled to the conductance of the nanopore. The angle of the contact should vary β between 1 for perfectly flat graphene-like pores to $4/3$ for a 90° wedge shaped pore. A quick calculation shows that for $r_p = 10$ nm and assuming that $1/f$ noise was clearly exhibited to 10^{-6} Hz (a Herculean month long experiment, but on par with measurements made on some electronic systems), the diffusion coefficient D must be much greater than 10^{22} m²/s. For an hour long experiment, $\Delta t \approx 3 \times 10^6$ sec, and assuming $D = 10^{22}$ m²/s the mean squared displacement of this parameter would be $\sqrt{2Dt} = 1.4$ nm. Clear parameters that are coupled to the pore conductance are the pore dimensions themselves and could be the very slowly diffusing parameter in question. Although we show at length in Chapter 3 that pore diameters increase with time, this is the change in the slowly varying mean of the pore size as it travels towards a chemical energy minimum and does not exclude the possibility of a random diffusion of pore dimensions. In fact, there is some evidence that for very stable pores, pore size occasionally shrinks on the nanometer scale [50]. Although this theory is not tested in this dissertation, we speculate that variation of pore angles and pore radii available with current fabrication methods could be used to test this theory.

Chapter 5

Proof of DNA translocation through ion-beam sculpted nanopores

5.1 Motivation

Proving that DNA translocates through the pore and interacts with it in the manner implied throughout this dissertation is another matter. It is entirely possible that the DNA simply ‘bumps’ into the pore, perhaps pinning at the pore opening before returning to the bulk in the *cis* chamber from whence it came. Such interactions would be interesting, but would require a completely different interpretation than what has been presented in this dissertation.

Determining that DNA translocates through the alpha-hemolysin nanopore was done in the first paper demonstrating the time resolved detection of DNA translocation by Kasianowicz *et al.* [6]. They accomplished this method by performing a PCR amplification of the possibly translocated DNA of the fluid in the *trans* chamber. PCR is capable of amplifying even a single DNA molecule to easily detectable amounts and primers (short DNA sequences) can be designed with very high specificity to target the DNA sequence to be amplified. This extreme sensitivity is a double edged sword since very small amounts of fluid from the *cis* chamber can accidentally contaminate the fluid in the *trans* chamber. To avoid this problem Kasianowicz performed a series of controls to ensure that the fluid in the *trans* chamber only came into contact with the *cis* fluid through the nanopore.

Proof of translocation through TEM fabricated pores was shown using a very different method by Gershow and Golovchenko [48]. In their work, triggering electronics were designed to reverse the polarity of the field applied to the nanopore a short time after detecting a translocation event. They saw a second current drop upon reversal of the polarity, and furthermore showed that an increase time between the first event and polarity reversal increased the time it took for the second event to occur. Their statistical mechanical treatment showed that this was entirely consistent with a sort of molecular ‘ping pong’ in which a DNA molecule would pass through the pore and undergo

a biased diffusion away from the pore before being pulled back through the opposite side.

Although established in biological pores and TEM fabricated pores, absent in the literature was proof that DNA passed through IBS nanopores. The geometry of IBS nanopores shown in Chapter 3 is very different from the geometry of TEM fabricated nanopores demonstrated by Kim *et al.* [19] and the ill characterized material that flows close to the pore may have a different surface charge from the SiN_x when in solution. These factors could repel the DNA from the nanopore and encourage ‘bumping’ events. To prove that DNA translocates through IBS nanopores we performed PCR similar to the method of Kasianowicz *et al.*.

5.2 Methods

To prove that dsDNA traversed from the *cis* to the *trans* chamber, a test was performed in which 1079 bp dsDNA with a known sequence was translocated through a 6 nm diameter nanopore fabricated with 3 keV Ne ions (codename Methusala) at 120 mV applied bias. The DNA used was the same 1079 bp DNA section of the ΦX174 phage described in Section 2.7.3 of Chapter 2. During the 4 hr recording time, \approx 40,000 current blockage events occurred.

We collected 3 samples (as controls) (50 μ L each) via pipette from the *trans* chamber before voltage was applied and 3 samples of the same volume after translocation. Between each sample, 50 μ L of fluid was injected through the fluid inlet to bring any DNA that had aggregated on or near the surface of the pore within reach of the pipette. Because the negatively charged DNA in the chamber could have aggregated on the positively charged electrode in the *trans* chamber, a reverse bias of -180 mV was applied for 2 min before each sample was taken. The control and *trans* samples were then amplified by PCR, separated using agarose gel electrophoresis, and photographed after staining with ethidium bromide to determine final DNA size. Positive and negative controls were also run using the same PCR reagents and thermal cycler to reduce the chance of false negatives or positives. Figure 5.1B shows the gel electrophoresis results that demonstrated the 1 kb dsDNA had traversed the solid state nanopore during the translocation experiment. We estimated that the number of DNA molecules translocating through the pore is consistent with the number of

blockage events observed.

A major complication of the PCR protocol was the fact that the fluid in the *trans* chamber was 1 M KCl, approximately 100 X the typical concentration of salt for a standard PCR run. It was feared that the pipetted samples would need to be diluted to bring the salt concentration to normal levels, however, this was not the case. A test PCR using the standard reagents and 1079 bp stock DNA showed that higher salt concentrations than those provided by Promega, the supplier of most of the reagents, actually improved the PCR yield. Because many PCR protocols were tried over several weeks, only small portions of each 50 μ L sample were used each time, leading to a minimum dilution of 20 X. Reagent concentrations and thermocycler protocols are listed in Table 5.2 and Table 5.1.

Step number	Duration	Temperature	Notes
1.	30 sec	95° C	Initial denaturation
2.	1 min	95° C	Denaturation
3.	1 min	50° C	Annealing
4.	1.5 min	72° C	Extension
5.			GOTO STEP 2. 34 TIMES
6.	5 min	72° C	Final extension
7.	Inf.	5° C	Hold until retrieved

Table 5.1: PCR thermocycler protocol for *trans* dsDNA sample.

Reagents	dsDNA
oligo1c	1 pM
oligo3	1 pM
dNTPs	200 μ M
MgCl ₂	2.5 mM
Promega GoTaq buffer (No dye)	1 X
GoTaq Polymerase	0.05 'units'/ μ L
dsDNA or control solution	Varies

Table 5.2: PCR reagents concentration. See 2.7.3 of Chapter 2 for descriptions of the reagents used. Add enough water to fill each PCR tube to 50 μ L. For controls and the *trans* sample extracted after translocation 1 μ L of solution was added. The *trans* sample extracted after translocation was not pre-diluted before addition.

Several key steps made this PCR successful.

- Use 50 μL total volume
- Put all PCR and intermediate mixing tubes on ice.
- Use the ‘master mix’ method. Premix all reagents that will be common for most or all lanes, this reduces the number of pipettings required, reduces pipette error since volumes are larger, and homogenizes the solutions used, making troubleshooting failed PCR runs easier.
- Use wide lanes as they tend to improve visibility of weak bands.
- Vortex when everything is mixed for a few seconds then spin samples briefly before pipetting in a low velocity centrifuge, taking care to not let the sample heat very long before running the PCR.

5.3 Results and Discussion

Lanes 2 and 3 of the gel in Figure 5.1 show that our PCR parameters were sufficient to amplify the DNA of interest and that we were free of contamination. Lane 4 (*trans* sample before the 1 kbp DNA was added to the *cis* side) has no 1 kbp dsDNA while lane 5 shows a clear 1 kbp band. This shows that the 1 kbp DNA was present in the *trans* chamber only after DNA was added to the *cis* chamber, demonstrating that the 1 kbp DNA translocated through the nanopore from the *cis* to the *trans* chamber and further supporting the interpretation of transient current blockages as being caused by single DNA molecules translocating through the pore.

5.4 Conclusion

In this chapter we showed novel results using PCR that DNA does translocate through IBS nanopores. The transient drops in current can be interpreted as DNA passing through the pore, as has been supposed throughout this dissertation.

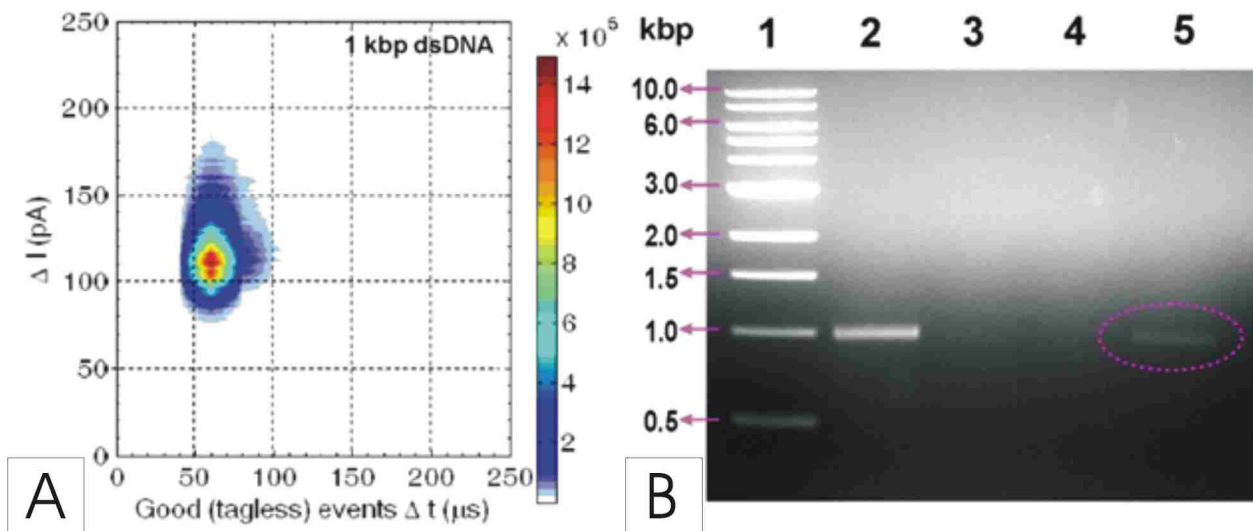


Figure 5.1: A) Density plot of current blockage events measured from the 1 kb dsDNA molecules. The average open pore current was $I_0 = 11 \pm 1.5$ nA during the time of the recording. We estimate the nanopore diameter is about 10 nm based on this open pore current. The most probable Current drop values are at 112 pA and 60 μ s. (B) Agarose gel electrophoresis to demonstrate that the 1 kb dsDNA traversed the solid state nanopore. Lane 1. Promega Corp. 1 kbp DNA ladder, Lane 2, Positive control for the *cis* chamber sample (10^8 X dilution), Lane 3, negative control with no template DNA, Lane 4, *trans* chamber solution before the DNA was added, Lane 5, *trans* sample collected after $\approx 40,000$ events were recorded. Photograph of the ethidium bromide-stained gel was taken using UV transillumination in a FluoroChem 8900 imaging system.

Chapter 6

Conclusion

In this dissertation I have provided novel insights into the relationship between the geometry of IBS nanopores and the signals they produce when used in single molecule experiments. This was accomplished by measuring the 3D size and shape of the nanopore to improve the models used to predict these signals. This improvement in the understanding of the nanopore has also provided a means to quantitatively monitor and improve the stability of the nanopore over time, making it a more robust experimental method.

In addition to the signal, the noise sources within the nanopore and experimental apparatus have been investigated. Sources fundamental to current measurement such as thermal noise, shot noise, and capacitive losses are discussed, as well as the nanopore specific surface chemistry noise. The low frequency $1/f$ noise was found to vary from pore-to-pore and it was shown that the source of this noise is not likely to be due to the noble gas used nor the annealing procedure used to fabricate the pore.

As a final contribution to the field, I use PCR to show that IBS pores indeed do translocate DNA as has been supposed for a decade.

Research into the application of nanopores to single molecule analysis is now over 20 years old and it has been over 12 years since the first solid state nanopore paper was published. Still, the nanopore field continues to attract interest by researchers across the globe and across scientific disciplines. It is my hope that the research presented here will make robust single molecule DNA sequencing and protein analysis one step closer.

But — as always — there is much more to learn.

References

- [1] Wallace H. Coulter. Means for counting particles suspended in a fluid, October 1953. U.S. Classification: 324/71.1.
- [2] Marshall Don Graham. The coulter principle: Foundation of an industry. *Journal of the Association for Laboratory Automation*, 8(6):72–81, December 2003.
- [3] Daniel Branton, David W. Deamer, Andre Marziali, Hagan Bayley, Steven A. Benner, Thomas Butler, Massimiliano Di Ventra, Slaven Garaj, Andrew Hibbs, Xiaohua Huang, Stevan B. Jovanovich, Predrag S. Krstic, Stuart Lindsay, Xinsheng Sean Ling, Carlos H. Mastrangelo, Amit Meller, John S. Oliver, Yuriy V. Pershin, J. Michael Ramsey, Robert Riehn, Gautam V. Soni, Vincent Tabard-Cossa, Meni Wanunu, Matthew Wiggin, and Jeffrey A. Schloss. The potential and challenges of nanopore sequencing. *Nature Biotechnology*, 26(10):1146–1153, 2008.
- [4] Elizabeth Pennisi. Search for pore-fection. *Science*, 336(6081):534–537, May 2012.
- [5] Sergey M. Bezrukov, Igor Vodyanoy, and V. Adrian Parsegian. Counting polymers moving through a single ion channel. *Nature*, 370(6487):279–281, July 1994.
- [6] John J. Kasianowicz, Eric Brandin, Daniel Branton, and David W. Deamer. Characterization of individual polynucleotide molecules using a membrane channel. *Proceedings of the National Academy of Sciences*, 93(24):13770–13773, November 1996.
- [7] Amit Meller, Lucas Nivon, Eric Brandin, Jene Golovchenko, and Daniel Branton. Rapid nanopore discrimination between single polynucleotide molecules. *Proceedings of the National Academy of Sciences of the United States of America*, 97(3):1079–1084, February 2000.
- [8] Ken Healy. Nanopore-based single-molecule DNA analysis. *Nanomedicine*, 2(4):459–481, August 2007.
- [9] Michael Zwolak and Massimiliano Di Ventra. Colloquium: Physical approaches to DNA sequencing and detection. *Reviews of Modern Physics*, 80(1):141–165, January 2008.
- [10] Jiali Li, Marc Gershow, Derek Stein, Eric Brandin, and J. A. Golovchenko. DNA molecules and configurations in a solid-state nanopore microscope. *Nature Materials*, 2(9):611–615, 2003.
- [11] Jiali Li, Derek Stein, Ciaran McMullan, Daniel Branton, Michael J. Aziz, and Jene A. Golovchenko. Ion-beam sculpting at nanometre length scales. *Nature*, 412(6843):166–169, July 2001.
- [12] Qun Cai, Brad Ledden, Eric Krueger, Jene A. Golovchenko, and Jiali Li. Nanopore sculpting with noble gas ions. *Journal of Applied Physics*, 100(2):024914–024914–6, 2006.
- [13] Derek Stein, Jiali Li, and Jene A Golovchenko. Ion-beam sculpting time scales. *Physical review letters*, 89(27):276106, December 2002.

- [14] Derek M. Stein, Ciaran J. McMullan, Jiali Li, and Jene A. Golovchenko. Feedback-controlled ion beam sculpting apparatus. *Review of Scientific Instruments*, 75(4):900–905, April 2004.
- [15] Toshiyuki Mitsui, Derek Stein, Young-Rok Kim, David Hoogerheide, and J. A. Golovchenko. Nanoscale volcanoes: Accretion of matter at ion-sculpted nanopores. *Physical Review Letters*, 96(3):036102, January 2006.
- [16] David P. Hoogerheide, H. Bola George, Jene A. Golovchenko, and Michael J. Aziz. Thermal activation and saturation of ion beam sculpting. *Journal of Applied Physics*, 109(7):074312–074312–4, April 2011.
- [17] H. Bola George, Yuye Tang, Xi Chen, Jiali Li, John W. Hutchinson, Jene A. Golovchenko, and Michael J. Aziz. Nanopore fabrication in amorphous si: Viscous flow model and comparison to experiment. *Journal of Applied Physics*, 108(1):014310–8, July 2010.
- [18] A. J. Storm, J. H. Chen, X. S. Ling, H. W. Zandbergen, and C. Dekker. Fabrication of solid-state nanopores with single-nanometre precision. *Nature Materials*, 2(8):537–540, 2003.
- [19] Min Jun Kim, Ben McNally, Kazuyoshi Murata, and Amit Meller. Characteristics of solid-state nanometre pores fabricated using a transmission electron microscope. *Nanotechnology*, 18(20):205302, May 2007.
- [20] Chuen Ho, Rui Qiao, Jiunn B. Heng, Aveek Chatterjee, Rolf J. Timp, Narayana R. Aluru, and Gregory Timp. Electrolytic transport through a synthetic nanometer-diameter pore. *Proceedings of the National Academy of Sciences of the United States of America*, 102(30):10445–10450, July 2005.
- [21] Daniel Fologea, James Uplinger, Brian Thomas, David S. McNabb, and Jiali Li. Slowing DNA translocation in a solid-state nanopore. *Nano Letters*, 5(9):1734–1737, September 2005.
- [22] Gerald S. Manning. The molecular theory of polyelectrolyte solutions with applications to the electrostatic properties of polynucleotides. *Quarterly Reviews of Biophysics*, 11(02):179–246, 1978.
- [23] A J Storm, J H Chen, H W Zandbergen, and C Dekker. Translocation of double-strand DNA through a silicon oxide nanopore. *Physical Review E*, 71(5 Pt 1):051903, May 2005.
- [24] Daniel Fologea, Eric Brandin, James Uplinger, Daniel Branton, and Jiali Li. DNA conformation and base number simultaneously determined in a nanopore. *Electrophoresis*, 28(18):3186–3192, September 2007.
- [25] Meni Wanunu, Jason Sutin, Ben McNally, Andrew Chow, and Amit Meller. DNA translocation governed by interactions with solid-state nanopores. *Biophysical Journal*, 95(10):4716–4725, November 2008.
- [26] Arnold J. Storm, Cornelis Storm, Jianghua Chen, Henny Zandbergen, Jean-Francois Joanny, and Cees Dekker. Fast dna translocation through a solid-state nanopore. *Nano Letters*, 5(7):1193–1197, 2005.

- [27] William Ralph Smythe. *Static and dynamic electricity*. International series in physics ; F.K. Richtmyer, consulting editor. London, McGraw-Hill Book Company, New York, 1st edition, 1939.
- [28] Ragnar Holm and Else Holm. *Electric Contacts: Theory and Application*. Springer, 4th edition, August 1999.
- [29] Bertil Hille. *Ion Channels of Excitable Membranes*. Sinauer Associates, 3rd edition, 2001.
- [30] Aleksii Aksimentiev, Jiunn B. Heng, Gregory Timp, and Klaus Schulten. Microscopic kinetics of DNA translocation through synthetic nanopores. *Biophysical Journal*, 87(3):2086–2097, September 2004.
- [31] G. M. King and J. A. Golovchenko. Probing nanotube-nanopore interactions. *Physical Review Letters*, 95(21):216103, November 2005.
- [32] Stefan Howorka, Stephen Cheley, and Hagan Bayley. Sequence-specific detection of individual DNA strands using engineered nanopores. *Nature Biotechnology*, 19(7):636–639, 2001.
- [33] Yann Astier, Orit Braha, and Hagan Bayley. Toward single molecule DNA sequencing: direct identification of ribonucleoside and deoxyribonucleoside 5'-monophosphates by using an engineered protein nanopore equipped with a molecular adapter. *Journal of the American Chemical Society*, 128(5):1705–1710, February 2006.
- [34] Hai-Chen Wu, Yann Astier, Giovanni Maglia, Ellina Mikhailova, and Hagan Bayley. Protein nanopores with covalently attached molecular adapters. *Journal of the American Chemical Society*, 129(51):16142–16148, December 2007.
- [35] Tom Z. Butler, Mikhail Pavlenok, Ian M. Derrington, Michael Niederweis, and Jens H. Gundlach. Single-molecule DNA detection with an engineered MspA protein nanopore. *Proceedings of the National Academy of Sciences*, 105(52):20647–20652, December 2008.
- [36] Ian M. Derrington, Tom Z. Butler, Marcus D. Collins, Elizabeth Manrao, Mikhail Pavlenok, Michael Niederweis, and Jens H. Gundlach. Nanopore DNA sequencing with MspA. *Proceedings of the National Academy of Sciences*, 107(37):16060–16065, September 2010.
- [37] Elizabeth A. Manrao, Ian M. Derrington, Andrew H. Laszlo, Kyle W. Langford, Matthew K. Hopper, Nathaniel Gillgren, Mikhail Pavlenok, Michael Niederweis, and Jens H. Gundlach. Reading DNA at single-nucleotide resolution with a mutant MspA nanopore and phi29 DNA polymerase. *Nature Biotechnology*, 30(4):349–353, 2012.
- [38] Christopher A. Merchant, Ken Healy, Meni Wanunu, Vishva Ray, Neil Peterman, John Bartel, Michael D. Fischbein, Kimberly Venta, Zhengtang Luo, A. T. Charlie Johnson, and Marija Drndic. DNA translocation through graphene nanopores. *Nano Letters*, 10(8):2915–2921, August 2010.
- [39] Gregory F. Schneider, Stefan W. Kowalczyk, Victor E. Calado, Gregory Pandraud, Henny W. Zandbergen, Lieven M. K. Vandersypen, and Cees Dekker. DNA translocation through graphene nanopores. *Nano Letters*, 10(8):3163–3167, August 2010.

- [40] S. Garaj, W. Hubbard, A. Reina, J. Kong, D. Branton, and J.A. Golovchenko. Graphene as a sub-nanometer trans-electrode membrane. *Nature*, 467(7312):190–193, September 2010.
- [41] Meng-Yue Wu, Diego Krapf, Mathijs Zandbergen, Henny Zandbergen, and Philip E. Batson. Formation of nanopores in a SiN/SiO₂ membrane with an electron beam. *Applied Physics Letters*, 87(11):113106–3, September 2005.
- [42] Aaron T. Kuan and Jene A. Golovchenko. Nanometer-thin solid-state nanopores by cold ion beam sculpting. *Applied Physics Letters*, 100(21):213104–4, May 2012.
- [43] Eliane H. Trepagnier, Aleksandra Radenovic, David Sivak, Phillip Geissler, and Jan Liphardt. Controlling DNA capture and propagation through artificial nanopores. *Nano Letters*, 7(9):2824–2830, September 2007.
- [44] Ulrich F. Keyser, Bernard N. Koeleman, Stijn van Dorp, Diego Krapf, Ralph M. M. Smeets, Serge G. Lemay, Nynke H. Dekker, and Cees Dekker. Direct force measurements on DNA in a solid-state nanopore. *Nature Physics*, 2(7):473–477, 2006.
- [45] Jrme Math, Hasina Visram, Virgile Viasnoff, Yitzhak Rabin, and Amit Meller. Nanopore unzipping of individual DNA hairpin molecules. *Biophysical Journal*, 87(5):3205–3212, November 2004.
- [46] Mark Bates, Michael Burns, and Amit Meller. Dynamics of DNA molecules in a membrane channel probed by active control techniques. *Biophysical Journal*, 84(4):2366–2372, April 2003.
- [47] Olga K Dudko, Jrme Math, Attila Szabo, Amit Meller, and Gerhard Hummer. Extracting kinetics from single-molecule force spectroscopy: nanopore unzipping of DNA hairpins. *Biophysical Journal*, 92(12):4188–4195, June 2007.
- [48] Marc Gershow and J. A. Golovchenko. Recapturing and trapping single molecules with a solid-state nanopore. *Nature Nanotechnology*, 2(12):775, 2007.
- [49] Nanopore sequencing: Towards the 15-minute genome. *The Economist*, March 2011.
- [50] Michiel van den Hout, Adam R Hall, Meng Yue Wu, Henny W Zandbergen, Cees Dekker, and Nynke H Dekker. Controlling nanopore size, shape and stability. *Nanotechnology*, 21(11):115304, March 2010.
- [51] Ryan Rollings and Jiali Li. Emerging technologies: Nanopore sequencing for mutation detection. In Khalid Meksem and Gnter Kahl, editors, *The Handbook of Plant Mutation Screening*, pages 339 – 354. Wiley-VCH Verlag GmbH & Co. KGaA, 2010.
- [52] Ryan C. Rollings, David S. McNabb, and Jiali Li. DNA characterization with ion beam-sculpted silicon nitride nanopores. In Maria E. Gracheva, editor, *Nanopore-Based Technology*, volume 870, pages 79–97. Humana Press, Totowa, NJ, 2012.
- [53] James Uplinger, Brian Thomas, Ryan Rollings, Daniel Fologea, David McNabb, and Jiali Li. K⁺, Na⁺, and Mg²⁺ on DNA translocation in silicon nitride nanopores. *Electrophoresis*, 33(23):3448–3457, December 2012.

- [54] W. van Gelder and V. E. Hauser. The etching of silicon nitride in phosphoric acid with silicon dioxide as a mask. *Journal of The Electrochemical Society*, 114(8):869–872, August 1967.
- [55] Bradley Thomas Ledden. Fabrication of solid states nanopores using feedback controlled ion beam sculpting techniques. Master’s thesis, University of Arkansas, 2004.
- [56] M. J. Kim, M. Wanunu, D. C. Bell, and A. Meller. Rapid fabrication of uniformly sized nanopores and nanopore arrays for parallel DNA analysis. *Advanced Materials*, 18(23):31493153, 2006.
- [57] David B. Williams and C. Barry Carter. *Transmission Electron Microscopy: A Textbook for Materials Science*. Springer, 2nd edition, August 2009.
- [58] Jessamine Ng Lee, Cheolmin Park, and George M. Whitesides. Solvent compatibility of poly(dimethylsiloxane)-based microfluidic devices. *Analytical Chemistry*, 75(23):6544–6554, December 2003.
- [59] Mirna Mihovilovic, Nicholas Hagerty, and Derek Stein. Statistics of DNA capture by a solid-state nanopore. *Physical Review Letters*, 110(2):028102, January 2013.
- [60] Bo Lu, Fernando Albertorio, David P. Hoogerheide, and Jene A. Golovchenko. Origins and consequences of velocity fluctuations during DNA passage through a nanopore. *Biophysical Journal*, 101(1):70–79, July 2011.
- [61] S. I. Raider, R. Flitsch, J. A. Aboaf, and W. A. Pliskin. Surface oxidation of silicon nitride films. *Journal of The Electrochemical Society*, 123(4):560–565, April 1976.
- [62] R. M. M. Smeets, U. F. Keyser, M. Y. Wu, N. H. Dekker, and C. Dekker. Nanobubbles in solid-state nanopores. *Physical Review Letters*, 97(8):088101, August 2006.
- [63] Matthew R. Powell, Leah Cleary, Matthew Davenport, Kenneth J. Shea, and Zuzanna S. Siwy. Electric-field-induced wetting and dewetting in single hydrophobic nanopores. *Nature Nanotechnology*, 6(12):798–802, 2011.
- [64] Frederick M. Ausubel, Roger Brent, Robert E. Kingston, David D. Moore, J. G. Seidman, John A. Smith, and Kevin Struhl, editors. *Current Protocols in Molecular Biology*, volume 1. John Wiley and Sons, 2012.
- [65] Maria Szekely. PhiX174 sequenced. *Nature*, 265(5596):685, February 1977.
- [66] F. Sanger, A.R. Coulson, T. Friedmann, G.M. Air, B.G. Barrell, N.L. Brown, J.C. Fiddes, C.A. Hutchison III, P.M. Slocombe, and M. Smith. The nucleotide sequence of bacteriophage PhiX174. *Journal of Molecular Biology*, 125(2):225–246, October 1978.
- [67] Warren A. Kibbe. OligoCalc: an online oligonucleotide properties calculator. *Nucleic Acids Research*, 35(suppl 2):W43–W46, July 2007.
- [68] Daniel Fologea, Marc Gershow, Bradley Ledden, David S. McNabb, Jene A. Golovchenko, and Jiali Li. Detecting single stranded DNA with a solid state nanopore. *Nano Letters*, 5(10):1905–1909, October 2005.

- [69] Gary M. Skinner, Michiel van den Hout, Onno Broekmans, Cees Dekker, and Nynke H. Dekker. Distinguishing single- and double-stranded nucleic acid molecules using solid-state nanopores. *Nano Letters*, 9(8):2953–2960, August 2009.
- [70] Anpan Han, Gregor Schrmann, Giampietro Mondin, Roland Andreas Bitterli, Nicole G. Hegelbach, Nico F. de Rooij, and Urs Staufer. Sensing protein molecules using nanofabricated pores. *Applied Physics Letters*, 88(9):093901–3, February 2006.
- [71] Gerald M. Cherf, Kate R. Lieberman, Hytham Rashid, Christopher E. Lam, Kevin Karplus, and Mark Akeson. Automated forward and reverse ratcheting of DNA in a nanopore at 5- α precision. *Nature Biotechnology*, 30(4):344–348, 2012.
- [72] Alon Singer, Meni Wanunu, Will Morrison, Heiko Kuhn, Maxim Frank-Kamenetskii, and Amit Meller. Nanopore based sequence specific detection of duplex DNA for genomic profiling. *Nano Letters*, 10(2):738–742, February 2010.
- [73] Peng Chen, Toshiyuki Mitsui, Damon B. Farmer, Jene Golovchenko, Roy G. Gordon, and Daniel Branton. Atomic layer deposition to fine-tune the surface properties and diameters of fabricated nanopores. *Nano Letters*, 4(7):1333–1337, June 2004.
- [74] Bala Murali Venkatesan, Brian Dorvel, Sukru Yemenicioglu, Nicholas Watkins, Ivan Petrov, and Rashid Bashir. Highly sensitive, mechanically stable nanopore sensors for DNA analysis. *Advanced Materials*, 21(27):2771, July 2009.
- [75] Waseem Asghar, Azhar Ilyas, Joseph Billo, and Samir Iqbal. Shrinking of solid-state nanopores by direct thermal heating. *Nanoscale Research Letters*, 6(1):372, May 2011.
- [76] Adam R. Hall, Andrew Scott, Dvir Rotem, Kunal K. Mehta, Hagan Bayley, and Cees Dekker. Hybrid pore formation by directed insertion of alpha-haemolysin into solid-state nanopores. *Nature Nanotechnology*, 5(12):874–877, 2010.
- [77] Nicholas A. W. Bell, Christian. R. Engst, Marc Ablay, Giorgio Divitini, Caterina Ducati, Tim Liedl, and Ulrich F. Keyser. DNA origami nanopores. *Nano Letters*, 12(1):512–517, January 2012.
- [78] Erik C. Yusko, Jay M. Johnson, Sheereen Majd, Panchika Prangko, Ryan C. Rollings, Jiali Li, Jerry Yang, and Michael Mayer. Controlling protein translocation through nanopores with bio-inspired fluid walls. *Nature Nanotechnology*, 6(4):253–260, 2011.
- [79] Eric Beamish, Harold Kwok, Vincent Tabard-Cossa, and Michel Godin. Precise control of the size and noise of solid-state nanopores using high electric fields. *Nanotechnology*, 23(40):405301–7, 2012.
- [80] Jiali Li and Jene A. Golovchenko. Solid-state nanopore for detecting individual biopolymers. In Robert S. Foote and James Weifu Lee, editors, *Micro and Nano Technologies in Bioanalysis*, volume 544, pages 81–93. Humana Press, Totowa, NJ, 2009.
- [81] R. F. Egerton. *Electron Energy-Loss Spectroscopy in the Electron Microscope*. Springer, 3rd edition, July 2011.

- [82] Caroline A. Schneider, Wayne S. Rasband, and Kevin W. Eliceiri. NIH image to ImageJ: 25 years of image analysis. *Nature Methods*, 9(7):671–675, 2012.
- [83] Meng-Yue Wu, Ralph M. M. Smeets, Mathijs Zandbergen, Ulrike Ziese, Diego Krapf, Philip E. Batson, Nynke H. Dekker, Cees Dekker, and Henny W. Zandbergen. Control of shape and material composition of solid-state nanopores. *Nano Letters*, 9(1):479–484, January 2009.
- [84] Ruoshan Wei, Daniel Pedone, Andreas Zrner, Markus Dblinger, and Ulrich Rant. Fabrication of metallized nanopores in silicon nitride membranes for single-molecule sensing. *Small*, 6(13):1406–1414, July 2010.
- [85] M. Radermacher. 3-dimensional reconstruction of single particles from random and non-random tilt series. *Journal of Electron Microscopy Technique*, 9(4):359–394, August 1988.
- [86] Changbae Hyun, Ryan Rollings, and Jiali Li. Scanning-probe microscopy: Probing access resistance of solid-state nanopores with a scanning-probe microscope tip. *Small*, 8(3):384–384, February 2012.
- [87] Ralph M. M. Smeets, Ulrich F. Keyser, Diego Krapf, Meng-Yue Wu, Nynke H. Dekker, and Cees Dekker. Salt dependence of ion transport and DNA translocation through solid-state nanopores. *Nano Letters*, 6(1):89–95, January 2006.
- [88] David P. Hoogerheide, Slaven Garaj, and Jene A. Golovchenko. Probing surface charge fluctuations with solid-state nanopores. *Physical Review Letters*, 102(25):256804, June 2009.
- [89] J. E. Hall. Access resistance of a small circular pore. *The Journal of General Physiology*, 66(4):531–532, October 1975.
- [90] Joseph D. Romano. The conical resistor conundrum: A potential solution. *American Journal of Physics*, 64(9):1150, 1996.
- [91] Stefan W Kowalczyk, Alexander Y Grosberg, Yitzhak Rabin, and Cees Dekker. Modeling the conductance and DNA blockade of solid-state nanopores. *Nanotechnology*, 22(31):315101, August 2011.
- [92] Meni Wanunu, Tali Dadosh, Vishva Ray, Jingmin Jin, Larry McReynolds, and Marija Drndi. Rapid electronic detection of probe-specific microRNAs using thin nanopore sensors. *Nature Nanotechnology*, 5(11):807–814, 2010.
- [93] Kirt R. Williams, Kishan Gupta, and Mathew Wasilik. Etch rates for micromachining processing part-II. *Journal of Microelectromechanical Systems*, 12(6):761–778, December 2003.
- [94] Gert F Eriksen and Karsten Dyrbye. Protective coatings in harsh environments. *Journal of Micromechanics and Microengineering*, 6(1):55–57, March 1996.
- [95] J. W. Osenbach and W. R. Knolle. Behavior of a-SiN:H and a-SiON:H films in condensed water. *Journal of the Electrochemical Society*, 139(11):3346–3351, November 1992.

- [96] M. Vogt and R. Hauptmann. Plasma-deposited passivation layers for moisture and water protection. *Surface and Coatings Technology*, 7475, Part 2(0):676–681, October 1995.
- [97] Eric Laarz, Boris V. Zhmud, and Lennart Bergstrm. Dissolution and deagglomeration of silicon nitride in aqueous medium. *Journal of the American Ceramic Society*, 83(10):2394400, 2000.
- [98] B.V. Zhmud and L. Bergstrm. Dissolution kinetics of silicon nitride in aqueous suspension. *Journal of Colloid and Interface Science*, 218(2):582–584, August 1999.
- [99] John M. Maloney, Sara A. Lipka, and Samuel P. Baldwin. In vivo biostability of CVD silicon oxide and silicon nitride films. *MRS Proceedings*, 872, 2005.
- [100] G. Schmitt, F. Fabender, H. Lth, M. J. Schning, J.-W. Schultze, and G. Bu. Passivation and corrosion of microelectrode arrays. *Materials and Corrosion*, 51(1):2025, 2000.
- [101] Tamara Diedrich, Agnieszka Dybowska, Jacques Schott, Eugenia Valsami-Jones, and Eric H. Oelkers. The dissolution rates of SiO₂ nanoparticles as a function of particle size. *Environmental Science & Technology*, 46(9):4909–4915, May 2012.
- [102] W. L. Scopel, M. C. A. Fantini, M. I. Alayo, and I. Pereyra. Structural investigation of si-rich amorphous silicon oxynitride films. *Thin Solid Films*, 425(1-2):275–281, February 2003.
- [103] P.J French, P.M Sarro, R Malle, E.J.M Fakkeldij, and R.F Wolffenbuttel. Optimization of a low-stress silicon nitride process for surface-micromachining applications. *Sensors and Actuators A: Physical*, 58(2):149–157, February 1997.
- [104] D. K. C. MacDonald. *Noise and Fluctuations: An Introduction*. John Wiley and Sons, 1962.
- [105] P. Dutta and P. M. Horn. Low-frequency fluctuations in solids: 1/f noise. *Reviews of Modern Physics*, 53(3):497–516, July 1981.
- [106] Frederick Reif. *Fundamentals of Statistical and Thermal Physics*. Waveland Pr Inc, December 2008.
- [107] Monson H. Hayes. *Statistical Digital Signal Processing and Modeling*. Wiley, April 1996.
- [108] Petar M. Djuric and Stephen M. Kay. Spectrum estimation and modeling. In Vijay Madisetti and Douglas B. Williams, editors, *The Digital Signal Processing Handbook*, pages 14:1–19. CRC Press, December 1997.
- [109] J. B. Johnson. Thermal agitation of electricity in conductors. *Physical Review*, 32(1):97–109, July 1928.
- [110] H. Nyquist. Thermal agitation of electric charge in conductors. *Physical Review*, 32(1):110–113, July 1928.
- [111] Rivka Sherman-Gold, editor. *The Axon Guide*. Molecular Devices, 3rd edition, 2007.

- [112] Jeffrey D. Uram, Kevin Ke, and Michael Mayer. Noise and bandwidth of current recordings from submicrometer pores and nanopores. *ACS nano*, 2(5):857–872, May 2008.
- [113] R. M. M. Smeets, U. F. Keyser, N. H. Dekker, and C. Dekker. Noise in solid-state nanopores. *Proceedings of the National Academy of Sciences*, 105(2):417–421, January 2008.
- [114] S.A Awan and R.D Gould. Conductivity and dielectric properties of silicon nitride thin films prepared by RF magnetron sputtering using nitrogen gas. *Thin Solid Films*, 423(2):267–272, January 2003.
- [115] David P. Hoogerheide. *Stochastic Processes in Solid State Nanopores*. PhD, Harvard University, Cambridge, Massachusetts, February 2010.
- [116] G. Gomila, C. Pennetta, L. Reggiani, M. Sampietro, G. Ferrari, and G. Bertuccio. Shot noise in linear macroscopic resistors. *Physical Review Letters*, 92(22):226601, June 2004.
- [117] D. R. Spiegel and R. J. Helmer. Shot-noise measurements of the electron charge: An undergraduate experiment. *American Journal of Physics*, 63(6):554–560, 1995.
- [118] W. H. Press. Flicker noises in astronomy and elsewhere. *Comments on Astrophysics*, 7:103–119, 1978.
- [119] Laszlo B. Kish and Sergey M. Bezrukov. Flows of cars and neural spikes enhanced by colored noise. *Physics Letters A*, 266(46):271–275, February 2000.
- [120] Richard F. Voss and John Clarke. $1/f$ noise in music and speech. *Nature*, 258(5533):317–318, November 1975.
- [121] Vincent Tabard-Cossa, Dhruvi Trivedi, Matthew Wiggin, Nahid N Jetha, and Andre Marziali. Noise analysis and reduction in solid-state nanopores. *Nanotechnology*, 18(30):305505, August 2007.
- [122] Matthew R. Powell, Ivan Vlassiouk, Craig Martens, and Zuzanna S. Siwy. Nonequilibrium $1/f$ noise in rectifying nanopores. *Physical Review Letters*, 103(24):248104, December 2009.
- [123] Matthew R. Powell, Craig Martens, and Zuzanna S. Siwy. Asymmetric properties of ion current $1/f$ noise in conically shaped nanopores. *Chemical Physics*, 375(23):529–535, October 2010.
- [124] M. R. Powell, N. Sa, M. Davenport, K. Healy, I. Vlassiouk, S. E. Letant, L. A. Baker, and Z. S. Siwy. Noise properties of rectifying nanopores. *The Journal of Physical Chemistry C*, 115(17):8775–8783, May 2011.
- [125] F.N. Hooge. $1/f$ noise is no surface effect. *Physics Letters A*, 29(3):139–140, April 1969.
- [126] Sh. Kogan. *Electronic Noise and Fluctuations in Solids*. Cambridge University Press, August 1996.

- [127] T. E. Burgess, J. C. Baum, F. M. Fowkes, R. Holmstrom, and G. A. Shirn. Thermal diffusion of sodium in silicon nitride shielded silicon oxide films. *Journal of The Electrochemical Society*, 116(7):1005–1008, July 1969.
- [128] R. Hezel and N. Lieske. Characterization of plasma-deposited silicon nitride films by auger electron spectroscopy and electron energy loss spectroscopy. *Journal of Applied Physics*, 53(3):1671–1674, March 1982.
- [129] K. A. Ellis and R. A. Buhrman. Boron diffusion in silicon oxides and oxynitrides. *Journal of The Electrochemical Society*, 145(6):2068–2074, June 1998.
- [130] Kunihiro Suzuki, Hideki Yamawaki, and Yoko Tada. Boron out diffusion from si substrates in various ambients. *Solid-State Electronics*, 41(8):1095–1097, August 1997.
- [131] Baoxing Xu, Yibing Li, Taehyo Park, and Xi Chen. Effect of wall roughness on fluid transport resistance in nanopores. *The Journal of Chemical Physics*, 135(14):144703, October 2011.
- [132] Mikhail R. Stukan, Patrice Ligneul, John P. Crawshaw, and Edo S. Boek. Spontaneous imbibition in nanopores of different roughness and wettability. *Langmuir*, 26(16):13342–13352, August 2010.
- [133] R J Messinger and T M Squires. Suppression of electro-osmotic flow by surface roughness. *Physical Review Letters*, 105(14):144503, October 2010.
- [134] S. Hofmann. Depth profiling in AES and XPS. In David Briggs and M. P. Seah, editors, *Practical Surface Analysis: Auger and X-ray photoelectron spectroscopy*, volume 1, pages 143–199. Wiley, 2nd edition, 1990.
- [135] David Briggs and M. P. Seah. *Practical Surface Analysis: Auger and X-ray Photoelectron Spectroscopy*, volume 1. Wiley, 2nd edition, 1990.
- [136] M. P. Seah. Charge referencing techniques for insulators. In David Briggs and M. P. Seah, editors, *Practical Surface Analysis: Auger and X-ray photoelectron spectroscopy*, volume 1, pages 143–199. Wiley, 2nd edition, 1990.
- [137] M. P. Seah. Quantification of AES and XPS. In David Briggs and M. P. Seah, editors, *Practical Surface Analysis: Auger and X-ray photoelectron spectroscopy*, volume 1, pages 143–199. Wiley, 2nd edition, 1990.
- [138] Michael B. Weissman. Simple model for 1/f noise. *Physical Review Letters*, 35(11):689–692, September 1975.

Appendix A

On the resolution limits of the nanopore method

A.1 Introduction

This section uses simplified models of current drop ΔI and translocation time τ_d as well as RMS noise I_{rms} to model the ultimate resolution of the nanopore based measurements as presented in this thesis. The model is based on the Student's t-test as an abstract classifier to determine when the magnitude and duration of an event, or region within an event, are large enough to extract useful information.

A.2 Model and Results

A.2.1 Simplified model the nanopore

We model the nanopore as a cylinder with diameter d_p piercing a flat, semi-infinite plane of thickness L_p . Furthermore, the solution immediately above and below the pore is a perfect conductor, with all voltage drop along the pore length.

A.2.2 Simplified model of DNA

We assume that the DNA is a perfectly insulating rigid rod with diameter equal to the crystallographically measured diameter $d_m = 2.2$ nm with length L_m where the length is dependent upon the number of basepairs, n_{bp} in the molecule using the crystallographic pitch between basepairs of $p = 0.34$ nm resulting in $L_m = n_{bp} \times p$ [9]. Furthermore, the DNA has a linear charge density of $\lambda = -0.3$ e/bp due to the deprotonation of the phosphate groups at the pH levels used in this study [22].

A.2.3 Single molecule measurements

We treat the case when a molecule, or region of a molecule, of cross section A_m extends fully across the pore, creating a constant cross section through the pore. Neglecting the effect of access resistance and the voltage drop outside the pore, current drop can be defined as

$$I_0 - I_b = \Delta I = V\sigma \frac{A_m}{L_p}. \quad (\text{A.1})$$

The translocation time can be derived by assuming a very simple Stokes' drag on a particle model, producing the translocation time

$$\tau_d = \frac{L_p k a \eta}{V \lambda}. \quad (\text{A.2})$$

where η is the solution viscosity, λ is the screened linear charge density of the molecule, and a is a parameter with units of length accounting for the dimensions of the pore. For a spherical particle this would be the radius of the sphere. In combination with the constant k , the product ka is treated as a fitting parameter to compare theory to measured data and is of limited importance to the results presented here. Intuitively, the information contained in the event would increase with both the duration of the event and the magnitude of the change in current. More fundamentally, counting the number of ions excluded during the event provides a clear, abstract means to define the information contained in the event and we thus use the event charge deficit (ECD) as the most important parameter when considering information content. To simplify it's calculation we assume

$$ECD = \Delta I \tau_d. \quad (\text{A.3})$$

A.2.4 Signal to noise ratio

To proceed further in defining resolution, we define the signal to noise ratio (SNR) of an event. Intuitively, a larger current drop and smaller RMS noise will lead to better signals. As a first approximation of the SNR, we define

$$SNR_I = \frac{\Delta I}{I_{rms}} \quad (\text{A.4})$$

This definition has been used by others [113, 121] as an approximate definition of SNR. A key question of any experimenter should be what controllable parameters are there that will provide better results, and of those, which are the most important? To help answer this question, we can rewrite SNR_I in terms of our model geometry and thermal RMS noise as

$$\begin{aligned} SNR_I &= \frac{V\sigma A_m/L_p}{\sqrt{4k_bTB/R}} \\ &= \frac{VA_m\sqrt{\sigma}}{\sqrt{4k_bTBL_pA_p}}. \end{aligned} \quad (\text{A.5})$$

We can already see that for a larger SNR_I the most important experimentally controllable parameter for a given molecule and pore is V , with weaker dependence on solution conductivity, σ . We can also see that decreasing every size related to the nanopore, namely L_p and A_p will also produce larger signals. In fact, because A_p varies with the square of pore diameter, decreasing pore diameter has a stronger effect than decreasing pore length. A non-intuitive conclusion is that $SNR_I \propto B^{-1/2}$, suggesting that low bandwidth measurements produce better results. However, a major drawback of this definition for SNR is that it does not include any temporal information. A very slowly moving molecule will provide more information than a quickly moving one and hence should increase the amount of information extracted, similarly a high bandwidth measurement will provide more data points with which to define the event. We need a better model to include these effects.

A.2.5 Statistical resolution limit

To improve upon this definition of SNR, we use a purely statistical approach. We have implicitly implied that a signal is the change in current drop, which is essentially a measurement of the difference between two mean current levels. If we treat each current level as a collection of data points, we can define a statistically significant current transition using the Student's t-test. This test is ideal for determining if the difference between the means of two small datasets are statistically

significantly different.

$$\begin{aligned}
\text{Null hypothesis } H_0 & : \langle I_0 \rangle = \langle I_b \rangle \\
\text{Alternative hypothesis } H_a & : \langle I_0 \rangle \neq \langle I_b \rangle \\
\frac{\langle I_0 \rangle - \langle I_{b,n} \rangle}{I_{rms}/\sqrt{n}} & > t_{\alpha/2}(n)
\end{aligned} \tag{A.6}$$

The term $\langle I_0 \rangle$ is the time averaged mean open pore current, assumed to be known with negligible error because of the many data points available before the event. $\langle I_{b,n} \rangle$ is the estimate of the blocked pore current over the n data points in the blocked event and I_{rms} is the standard deviation of the open pore current and assumed to be identical to the standard deviation of the blocked current. Strictly speaking we should use the experimentally estimated standard deviation over the n points in the blockage level instead of I_{rms} , however, observation of many events shows that the RMS current during an event nearly the same as the RMS value.

The term $t_{\alpha/2}(n)$ is the cumulative density function of the Student t-distribution and exact calculation requires use of the incomplete beta function. The subscript α denotes the acceptable probability of falsely rejecting the null hypothesis, with smaller values being more strict. It is divided by two because this is a two-tailed test, that is, we don't care if the next current level is above or below the previous one. We assume that being 95% certain a transition occurred ($\alpha = 0.05$) would be the minimum required for high quality sequencing. Because of the complicated functional of $t_{\alpha/2}$, we approximate the case of $\alpha = 0.05$ with a power law that fits well for $n > 2$, defined by

$$t_{0.025} \approx 2 + 6.6n^{-\frac{3}{2}} \tag{A.7}$$

Rewriting equation A.6 in terms of SNR_I and $t_{0.025}$ yields

$$\begin{aligned}
SNR_I \sqrt{n} & > 2 + 6.6n^{-\frac{3}{2}} \\
SNR_I n^2 - 2n^{-\frac{3}{2}} & > 6.6
\end{aligned} \tag{A.8}$$

Before we continue, we need to relate n to parameters related to translocation. If we assume there is negligible information beyond our filter bandwidth, for a molecule (or feature within a molecule) with translocation duration τ_d , we can treat our sample rate as the inverse of the filter bandwidth, meaning the total number of measurements becomes

$$n = B\tau_d. \quad (\text{A.9})$$

Thus we can rewrite equation A.9 as

$$SNR_I(B\tau_d)^2 - 2(B\tau_d)^{\frac{3}{2}} > 6.6. \quad (\text{A.10})$$

For all values of SNR_I , B , and τ_d where this equation is true, we can statistically accept a current transition as valid. Solving this equation numerically to create a measurement-space ‘phase diagram’ as shown in Figure A.1. In this figure, each region defines the criteria for statistically significant definition of an event. For example, at 10 kHz bandwidth, an event with SNR_I of 3 and a translocation duration of 200 μs is measurable, but a 100 μs event is not. The inequalities for each region represent the fact that an event at a given SNR_I that is measurable at low bandwidth will also be measurable at a higher bandwidth. The SNR_I region numerically predicted by equation A.5, is actually far higher and would not be shown on this graph, but in practice, current drops are lower than predicted by the toy model and noises are higher. The values for the impractical SNR region shown are empirically defined and include estimates of other sources of noise in the amplifier and nanopore system. A detailed analysis of current drops magnitude is presented in Chapter 3 and noise is further discussed in Chapter 4.

A.3 Discussion

Although the assumption that $n = B\tau_d$ is reasonable, it presents some problems. For example, at the 10 kHz measurement bandwidth typical of nanopore experiments, a 100 μs translocation event has only one data point and is invalid for our statistical definition. This effect will make

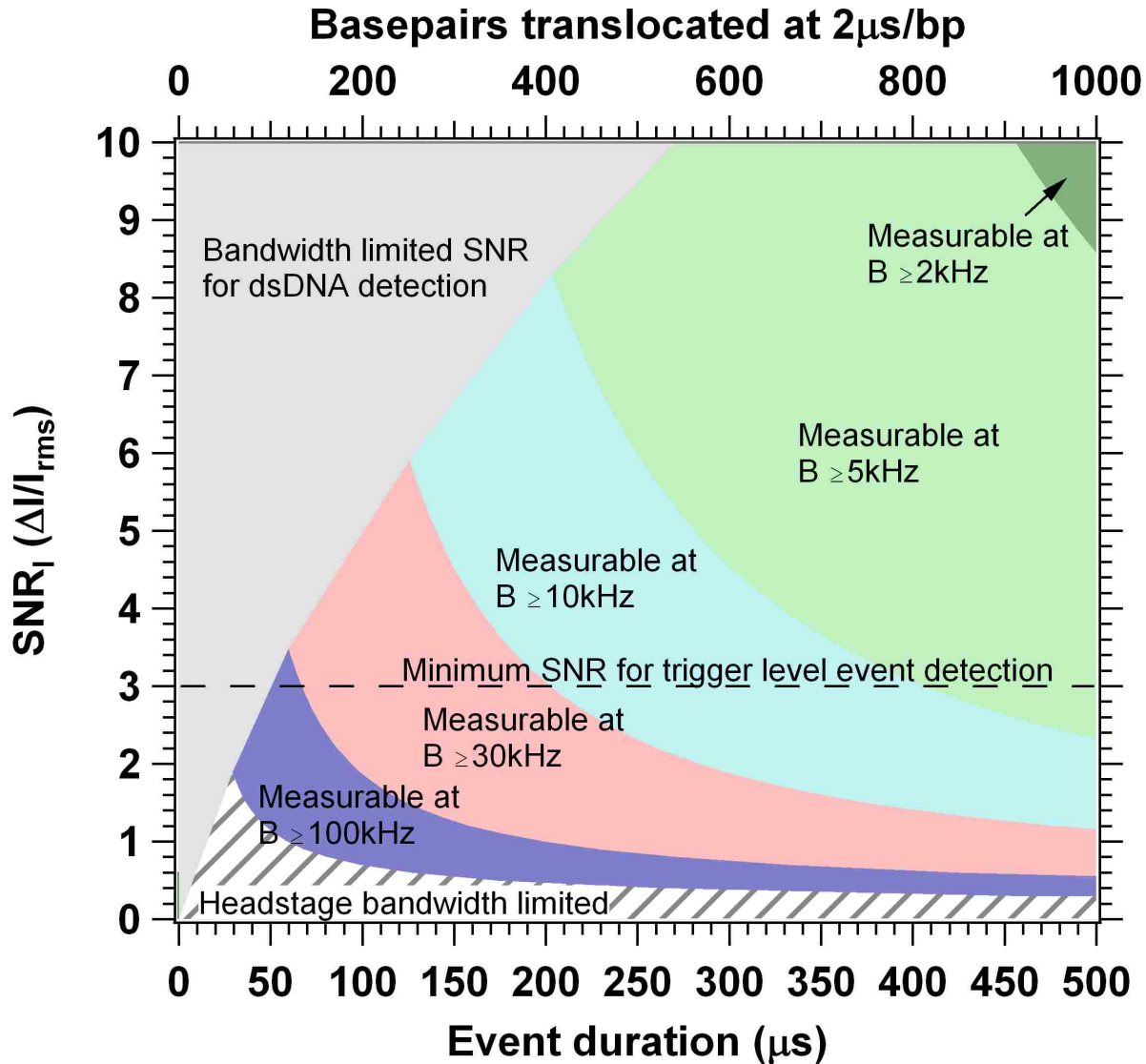


Figure A.1: Theoretical ‘phase diagram’ depiction showing the measurement bandwidth required to measure translocation events as a function of SNR and event duration. Detection of shorter event durations require higher bandwidth and higher signal to noise ratio.

the boundaries separating each measurable region more vertical as lower event durations. This problem is softened somewhat since there is information beyond the -3 dB signal attenuation of the filter we are using to define the bandwidth, with rough estimates of usable information up to 3B [111]. Further improvements to this model could add more data points to the statistical test corresponding to the higher frequency data but reduce the weight of the added points depending upon the filter roll-off. Another omission of this model is that it assumes that we know *a priori* which data belongs to which current level. In practice, this requirement forces a minimum SNR_I

of about 3 using the double trigger level detection method outlined in Chapter 2.

So far in our discussion we have kept our discussion in terms of translocation time and have not taken advantage of the voltage and molecule length dependence of our translocation time in equation A.2. We note that τ_d is approximate and depends upon the factor k which in experiment has been shown to be over a magnitude different from simple hydrodynamic equations [21] and can increase as pore diameter decreases [10, 25]. Empirically, however, translocation times for pores with ≈ 10 nm diameter used in this work have translocation times on the order of 2 bp/s, providing the information for the top axis in Figure A.1.

This graph matches very well with our experience in detecting short events, as it has always been difficult to measure translocations less than 100 μ s in duration at the typically used 10 kHz bandwidth, it also shows by the length of DNA translocated for this work was thousands of bases in order to avoid detection problems from small molecules.

This analysis on resolution was prompted by unfruitful work on 1000 nt ssDNA with 60 bp dsDNA regions. Detecting the difference between double and single stranded DNA effectively halves the signal and hence SNR_I . If we take that to mean the minimum SNR_I for detecting a single featureless double strand molecule must be 6, the minimum duration is about 150 μ s. For free translocation at 2 μ s/bp that means a minimum number of basepairs of about 300 bp, 5 times longer than the molecules studied.

A.4 Conclusion

In this appendix I define an abstract statistical test to determine the information content of a translocation event and determine at what bandwidth what event durations are detectable. It is clear from this discussion that faster events with smaller current drop magnitudes can benefit from higher bandwidth measurements.

